

---

# Climate variability modes and their impact on the hydrological cycle

- A model evaluation study -

Dominik Kunert

---



Webbing 2015



Ludwig Maximilians University Munich  
Faculty of Physics  
Meteorological Institute Munich

---

**Climate variability modes and their impact on the  
hydrological cycle  
- A model evaluation study -**

**Dominik Kunert**

---

**Master Thesis**

Supervisor: Priv.-Doz. Dr. habil. Veronika Eyring (DLR)

Scientific Advisor: Dr. Axel Lauer (DLR)

German Aerospace Center  
Institute of Atmospheric Physics

October 2015



Ludwig Maximilians Universität München

Fakultät für Physik

Meteorologisches Institut München

---

**Mehrjährige Klimavariabilitäten und ihre  
Auswirkungen auf den hydrologischen Kreislauf  
Eine Modellevaluierungsstudie**

**Dominik Kunert**

---

**Masterarbeit**

Gutachterin: Priv.-Doz. Dr. habil. Veronika Eyring (DLR)

Fachlicher Betreuer: Dr. Axel Lauer (DLR)

Deutsches Zentrum für Luft- und Raumfahrt

Institut für Physik der Atmosphäre

Oktober 2015



## **Abstract**

Climate models are essential tools for studying and projecting climate change and climate variability. A thorough assessment of a model's ability to reproduce the observed present-day climate is therefore a crucial prerequisite for building up confidence in the model's ability to project the future climate. This includes modes of natural climate variability such as the El Niño-Southern Oscillation (ENSO) and the Pacific Decadal Oscillation (PDO) that are spontaneously generated and that need not exhibit the same chronological sequence in models as in nature.

The main focus of this thesis is an assessment of representation of ENSO and PDO as well as the impact of these climate modes on cloud parameters and precipitation. For this, different simulations from the Max Planck Institute Earth System Model (MPI-ESM) and the ECHAM/MESSy Atmospheric Chemistry Model (EMAC) are evaluated. These include a coupled fully coupled ocean atmosphere simulation from the MPI-ESM, a simulation with prescribed SSTs from both MPI-ESM and EMAC, and an EMAC simulation which is nudged towards realistic meteorology. To evaluate the model simulations, a variety of different observational data sets are used. To evaluate the climate modes, the National Center for Atmospheric Research (NCAR) Climate Variability Diagnostics Package (CVDP) has been implemented into the Earth System Model Evaluation Tool (ESMValTool) as part of this thesis. The CVDP computes statistical key metrics of internal climate variability for model simulations and observational data sets. The ESMValTool is a software tool developed by multiple institutions that aims at improving routine Earth System Models (ESM) evaluation. Additionally, new diagnostics have been integrated into the ESMValTool to evaluate the response of clouds and precipitation to the selected modes of climate variability ENSO and PDO.

The results show that the spatial structure of the PDO simulated by the MPI-ESM coupled is quite realistic and in terms of temporal variability, the MPI-ESM coupled produces a periodic response of approximately the same frequency as observed – that is, periods of 3 – 7 years for ENSO, and ~20 years for the PDO. However, the MPI-ESM coupled model only weakly resembles the observed asymmetry between the El Niño and La Niña events, but simulates a quite realistic SST evolution to ENSO. Teleconnections of the atmospheric circulation with ENSO including corresponding changes in temperature, precipitation, and cloud properties are reasonably well captured by the MPI-ESM and EMAC model simulations. Systematic differences in the performance of the coupled and the atmosphere-only model runs with MPI-ESM and between the free-running and the nudged EMAC model simulations in reproducing the observed relationships between PDO, ENSO, and local SST changes and cloud parameters and precipitation are rather small. This points to the necessity to improve model parameterizations of the relevant physical processes such as convection or boundary layer processes.



# Content

<b>1</b>	<b>Introduction</b>	<b>1</b>
1.1	Background and Motivation	1
1.2	Structure of the Thesis	3
<b>2</b>	<b>Scientific Background</b>	<b>4</b>
2.1	Internal Modes of Climate Variability	4
2.1.1	El Niño and Southern Oscillation (ENSO)	4
2.1.1.1	Current Understanding of the ENSO Mechanism	6
2.1.1.2	Climate Impacts related to ENSO	6
2.1.2	Pacific Decadal Oscillation (PDO)	8
2.2	Statistical Methods	9
2.2.1	Empirical Orthogonal Functions (EOFs)	10
2.2.2	Spectral Analysis	11
2.2.3	Root-Mean-Square Difference (RMSD) and Overall Mean Bias (OMB)	11
<b>3</b>	<b>Tools for Model Evaluation and Implementation</b>	<b>12</b>
3.1	The Earth System Model Evaluation Tool (ESMValTool)	12
3.2	NCAR Climate Variability Diagnostics Package (CVDP)	12
3.2.1	Brief Description of CVDP	12
3.2.2	Implementation of CVDP into the ESMValTool	13
3.3	Additional Routines for Cloud Properties and Precipitation	15
<b>4</b>	<b>Models, Model Simulations and Observations for Evaluation</b>	<b>17</b>
4.1	Models	17
4.1.1	Max Planck Institute Earth System Model (MPI-ESM)	17
4.1.2	ECHAM/MESSy Atmospheric Chemistry Model (EMAC)	17
4.2	Model Simulations	18
4.2.1	Max Planck Institute Earth System Model (MPI-ESM)	18
4.2.2	ECHAM/MESSy Atmospheric Chemistry Model (EMAC)	19
4.3	Observational Data for Model Evaluation	19

<b>5</b>	<b>Results .....</b>	<b>23</b>
<b>5.1</b>	<b>Evaluation of the Mean State .....</b>	<b>23</b>
5.1.1	Evaluation of Annual Mean Near-Surface Air Temperature.....	26
5.1.2	Evaluation of Annual Mean Precipitation .....	28
5.1.3	Evaluation of Annual Mean Total Cloud Amount .....	30
5.1.4	Evaluation of Annual Mean Liquid Water Path .....	31
5.1.5	Summary of the Evaluation of the Mean State.....	34
<b>5.2</b>	<b>Natural Modes of Climate Variability .....</b>	<b>35</b>
5.2.1	Geographical Pattern of Non-Seasonal Sea Surface Temperature Variability .....	35
5.2.2	Pacific Decadal Oscillation (PDO).....	37
5.2.3	El Niño-Southern Oscillation (ENSO) .....	41
5.2.3.1	Niño-3.4 SST Variability.....	41
5.2.3.2	Composite El Niño and La Niña Events.....	43
5.2.3.3	Global Teleconnections .....	48
<b>5.3</b>	<b>Regional Impacts of ENSO and PDO on Clouds and Precipitation .....</b>	<b>53</b>
5.3.1	Tropics.....	54
5.3.2	NEP mid-latitudes .....	57
5.3.3	SEP Stratocumulus Region.....	59
<b>5.4</b>	<b>The Role of the Model Setup .....</b>	<b>61</b>
5.4.1	MPI-ESM coupled vs. MPI-ESM AMIP.....	61
5.4.2	EMAC RC1-base-07 vs. EMAC RC1SD-base-10 .....	63
<b>6</b>	<b>Summary and Outlook .....</b>	<b>65</b>
<b>7</b>	<b>Acknowledgements.....</b>	<b>68</b>
<b>8</b>	<b>References .....</b>	<b>69</b>

# 1 Introduction

## 1.1 Background and Motivation

Sea surface temperature (SST) anomalies, particularly in the equatorial and northern Pacific Ocean associated with the natural climate variability modes El Niño-Southern Oscillation (ENSO) (Trenberth et al., 2002; Wang et al., 2012) and Pacific Decadal Oscillation (PDO) (Mantua et al., 1997; Alexander et al., 2010) are closely connected with global climate on seasonal and longer time scales (IPCC, 2013). Driven primarily by coupled ocean-atmosphere processes within the Pacific basin, ENSO and PDO affect temperature, cloud properties and precipitation through atmospheric teleconnections worldwide including many socio-economically vulnerable areas (Trenberth et al., 1998; Alexander et al., 2002). Such effects include large impacts on agriculture, water resources (droughts), flooding as well as on air quality and wildfires.

Although the basic physical mechanisms of thermal and dynamical air-sea coupling leading to ENSO events are well studied (Deser et al., 2012) other aspects remain less well understood. These include processes responsible for the spatial and temporal asymmetries between El Niño and La Niña, the degree of regularity of the ENSO cycle and the triggering mechanisms of warm and cold events.

The mechanisms generating the PDO and its effects on weather and climate are very complex. Many studies therefore apply statistical methods to study the PDO and its dynamics (e.g., Newman et al., 2003; Vimont, 2005; Qiu et al., 2007; Newman, 2007). Unlike ENSO, the PDO is likely not a single physical mode but rather the sum of several phenomena (Deser et al., 2010).

Climate models are essential tools for studying and projecting climate change and climate variability. A thorough assessment of a model's ability to reproduce the observed present day climate is therefore a crucial prerequisite for building up confidence in the model's ability to project the future climate.

Problems still persist in the ability of coupled atmosphere-ocean climate models to accurately represent the tropical Pacific mean state, and ENSO's natural variability. The precipitation response to interannual climate variations like ENSO also continues to be a challenge for coupled climate models (Dai et al., 2006) with the same applying to the modelling of the response of cloud properties to these climate modes. A principal difficulty when assessing hydrological teleconnections is that errors in the simulated ENSO dynamics (e.g., amplitude or spatial distribution of the main SST anomaly in the equatorial Pacific) degrade the quality of the simulation at the source region before the teleconnection mechanisms even begin (Joseph and Nigam 2006).

In order to evaluate the performance in reproducing natural modes of climate variability and resulting teleconnections, the NCAR Climate Variability Diagnostics Package (CVDP) (Phillips et al., 2014) has been implemented into the Earth System Model Evaluation Tool (ESMValTool, Eyring et al., 2015) as part of this thesis. The CVDP computes key metrics of internal climate variability for a set of

user-specified model simulations and observational data sets. The ESMValTool is an open source package that allows for the evaluation and routine benchmarking of Earth system models (ESMs) and is available upon request at <http://www.pa.op.dlr.de/ESMValTool/>. In addition to the CVDP, new diagnostics to evaluate global and regional teleconnections between the natural modes of climate variability ENSO and PDO and the hydrological cycle are developed and implemented into the ESMValTool. ESMValTool-CVDP is then used to assess the performance of simulations with the ECHAM/MESSy Atmospheric Chemistry Model (EMAC) (Jöckel et al., 2006; 2010; 2015) and selected Coupled Model Intercomparison Project 5 (CMIP5) (Taylor et al., 2012) simulations with the Max Planck Institute Earth System Model (MPI-ESM) (Giorgetta et al., 2013).

Specifically, the CMIP5 long-term (~150 years) coupled atmosphere-ocean historical simulation and the Atmospheric Model Intercomparison Project (AMIP) (Gates et al. 1999) simulation with the MPI-ESM as well as an AMIP and a nudged simulation with the EMAC are analysed. In the nudged configuration of EMAC, atmospheric variables like temperature, vorticity, and divergence are continuously forced towards reanalysis data. The hydrological cycle itself is not directly forced and responds to the atmospheric state in the model simulations.

The focus of this study is to first assess the annual mean state of near-surface air temperature (TAS), precipitation (PR), total cloud amount (TCA), and liquid water path (LWP) in the coupled atmosphere-ocean experiment (“coupled”) and the AMIP simulations with the MPI-ESM and two model simulations with the EMAC model in the configuration with prescribed SSTs. This is followed by an evaluation of the representation of the tropical Pacific mean state focusing on SST, the PDO, and ENSO’s seasonal evolution in the MPI-ESM coupled simulation. In order to study the atmospheric part of potential teleconnections, simulations with prescribed SSTs are analysed, i.e., MPI-ESM AMIP and the two EMAC model runs. The MPI-ESM coupled is also compared with the MPI-ESM AMIP simulation, and the nudged EMAC run with the free-running EMAC simulation.

This study addresses particularly four questions regarding the effects of natural climate variabilities on the hydrological cycle:

1. How well are the models representing the annual mean state for near-surface air temperature, precipitation, total cloud amount, and liquid water path compared with observations?
2. Can the coupled ocean-atmosphere version of MPI-ESM reproduce the observed tropical Pacific mean state in SST, the PDO, and the seasonal evolution of ENSO?
3. Are the models capable of correctly simulating the response of cloud parameters to the modes of natural climate variability ENSO and PDO? What is the role of changes in the local SST for the variability in the cloud properties compared to possible teleconnections with PDO and ENSO?

4. Are there systematic differences between the coupled ocean-atmosphere version and the atmosphere-only configuration (AMIP) of MPI-ESM using prescribed SSTs? Does the nudged simulation of EMAC perform better than the free-running version?

## **1.2 Structure of the Thesis**

This thesis is structured in the following way. Chapter 2 provides the basic theoretical framework summarizing the current understanding of the natural climate variabilities PDO and ENSO in the Pacific Ocean. In addition, theoretical mechanisms, occurrence, and global impacts are discussed and a short overview on the statistical techniques used in this thesis is given. In chapter 3, a brief description of the ESMValTool and the CVDP and its implementation into the ESMValTool are given. Additionally, the newly implemented diagnostics are presented. A description of the MPI-ESM and EMAC models, the model setups, and the observations used for evaluation are given in chapter 4. Chapter 5 presents and discusses the most important results. Chapter 6 summarizes the most important findings and gives an outlook for possible further studies.

## **2 Scientific Background**

### **2.1 Internal Modes of Climate Variability**

The climate varies naturally because in a system of components with very different response times and non-linear interactions, the involved climate components are never fully in equilibrium and are constantly varying. Examples of such internal climate variations are the PDO in the northern Pacific and ENSO resulting from the interaction between atmosphere and ocean in the tropical Pacific. The focus of this thesis lies on the two internal modes PDO and ENSO that are introduced in the following.

#### **2.1.1 El Niño and Southern Oscillation (ENSO)**

The El Niño and the Southern Oscillation (ENSO) is a periodic fluctuation in sea surface temperature (El Niño) and the air pressure of the overlying atmosphere (Southern Oscillation) across the equatorial Pacific Ocean. An overview of the three ENSO phases (El Niño, neutral phase and La Niña) is given in figure 2.1.

In the neutral phase (neither El Niño nor La Niña) trade winds blow westward over the ocean surface of the tropical Pacific. The circulation brings near-surface warm moist air and warmer surface waters towards the western Pacific and the central Pacific keeps relatively cool. The warm and humid air over the western Pacific results in strong atmospheric convection and with high cumulonimbus clouds and precipitation. The circulation pattern of air rising in the west and descending in the east with the westward moving winds at the ground is referred to as the Walker Circulation. In the western tropical Pacific, the thermocline is deeper than in the east. The thermocline is the depth at which the temperature decreases rapidly with increase of depth. During a La Niña event, the Walker Circulation intensifies with stronger westward trade winds and enhanced convection over the western Pacific. During an El Niño event, the trade winds weaken and warmer than normal water streams into the central and eastern tropical Pacific. Sea surface temperatures near the Maritime Continent are therefore cooler than normal and the centre of the convection moves eastwards away from the Maritime Continent and Australia towards the central tropical Pacific. This results in increased rainfall over the central equatorial Pacific and South America, but less rainfall over Australia and the Maritime Continent (Trenberth, 1997; Trenberth et al., 1998) (<http://www.bom.gov.au/climate/enso/history/In-2010-12/three-phases-of-ENSO.shtml>).

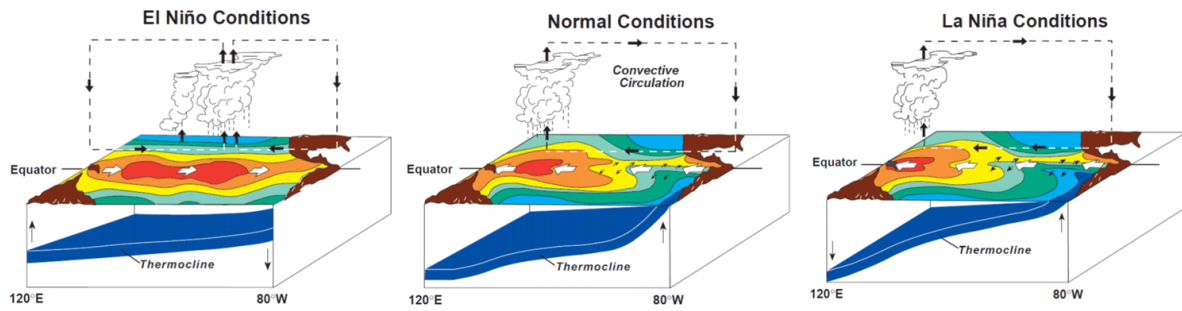


**Figure 2.1:** Conditions during El Niño, neutral phase, and La Niña  
 (Source: [http://www.pmel.noaa.gov/tao/proj\\_over/diagrams/gif/nina\\_normal\\_nino.gif](http://www.pmel.noaa.gov/tao/proj_over/diagrams/gif/nina_normal_nino.gif))

Changes in the amount of heat in the upper water layer typically induce and sustain ENSO events in the equatorial Pacific. The deeper ocean plays an essential role in determining strength and longevity of an ENSO event. The storage of large amounts of heat (El Niño) or miss of heat (La Niña) are causing an event do not dissipate rapidly.

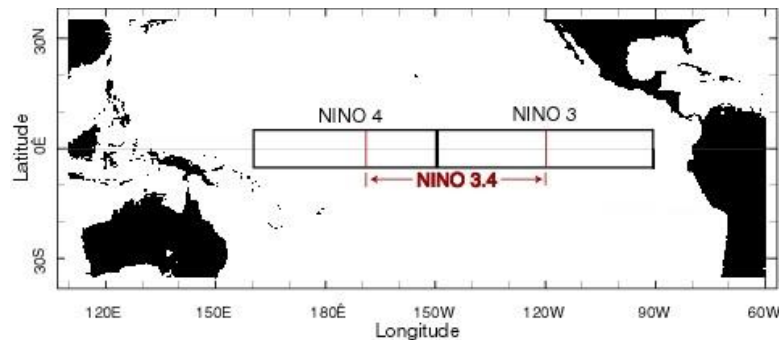


**Figure 2.2:** Niño-3.4 region (5°S - 5°N, 120° -170°W) (Source: <https://www.ncdc.noaa.gov/sotc/images/nino-regions.jpg>)

To characterize the intensity of an ENSO event, the Niño-3.4 index is used in this thesis (figure 2.2). The Niño-3.4 index is the average sea surface temperature anomaly in the region by 5°S to 5°N, from 170°W to 120°W. An anomaly in tropical SST in the Pacific is called an El Niño or La Niña event if the 5-month running mean of the Niño-3.4 index exceeds +0.5 °C for El Niño or -0.5 °C for La Niña for at least 6 consecutive months (Trenberth, 1997).

Another ENSO index is the so-called Southern Oscillation Index, or SOI, that displays the intensity of El Niño or La Niña events in the Pacific Ocean. The SOI is computed using the sea level pressure differences between Tahiti and Darwin. Negative values of the SOI below -8 hPa often indicate El Niño episodes and positive values of the SOI above +8 hPa are typical of a La Niña episode (Deser and Wallace, 1999; Harrison and Larkin, 1996).

Usually El Niño and La Niña events last about 12-18 months and occur approximately every 3-7 years (Deser et al., 2010).

### **2.1.1.1 Current Understanding of the ENSO Mechanism**

ENSO has been explained either as a self-sustained and natural oscillatory mode of the coupled ocean-atmosphere system or as a stable mode triggered by stochastic forcing (Wang et al., 2012). In both cases, ENSO involves the positive ocean-atmosphere feedback pointed out by Bjerknes (1969): an initial positive SST anomaly in the equatorial eastern Pacific reduces the zonal SST gradient and weakens the Walker circulation and hence the trade winds around the equator. The weakened trade winds further drive the ocean circulation changes that reinforce the SST anomaly leading to persistent warm conditions. After an El Niño event reaches its peak phase, negative feedbacks are necessary to terminate the maintaining of the El Niño conditions in the central and eastern Pacific. Four conceptual ENSO oscillator models have been established leading to a negative feedback ending an El Niño: the delayed oscillator (Suarez and Schopf, 1988; Battisti and Hirst, 1989), the recharge oscillator (Jin, 1997), the western Pacific oscillator (Weisberg and Wang, 1997; Wang et al., 1999), and the advective-reflective oscillator (Picaut et al., 1997). These negative feedbacks can act together and can terminate El Niño conditions as suggested by the unified oscillator (Wang, 2001).

El Niño can also be explained as a stable (or damped) mode triggered by or interacting with stochastic forcing (Philander and Fedorov, 2003). This hypothesis suggests that external disturbances to the coupled atmosphere-ocean system are the origin of random forcing that drives ENSO. A strength of this hypothesis is that it can explain the irregular behaviour of the ENSO variability in terms of noise. This “noise” also explains why every El Niño event is different and why El Niño is so difficult to predict (Philander and Fedorov, 2003). External atmospheric forcing can produce noise like westerly wind bursts, Madden-Julian Oscillation events (Gebbie et al., 2007) and the tropical instability waves in the eastern Pacific Ocean (An, 2008). A more detailed description of the individual feedbacks can be found in Wang et al. (2012) or in the above mentioned papers.

### **2.1.1.2 Climate Impacts related to ENSO**

Most of the climate impacts of ENSO are most pronounced in the equatorial Pacific and surrounding regions (Ropelewski and Halpert, 1989). Examples for the climate impact of El Niño include heavy precipitation and flooding in northwestern South America, especially Peru, Ecuador, and Columbia during December to February (see Figure 2.3), and the loss of fish and clam populations (Barriga and Quiroy, 2002), which are important to the economy and food supply of the region. Although the rainfall rates increase or decrease as response to the increasing intensity of El Niño and La Niña,

events of similar intensity (as defined by the Niño-3.4 SST anomalies) do not produce effects of the same magnitude. At the same time, droughts in Australia and the Maritime Continent (Ropolewski and Halpert, 1996) can lead to wildfires and widespread smoke in that region. The impacts of El Niño and La Niña are typically strongest and most widespread during boreal winter (Trenberth et al., 1998). During austral winter, El Niño impacts are weaker and mostly restricted to the southern hemisphere.

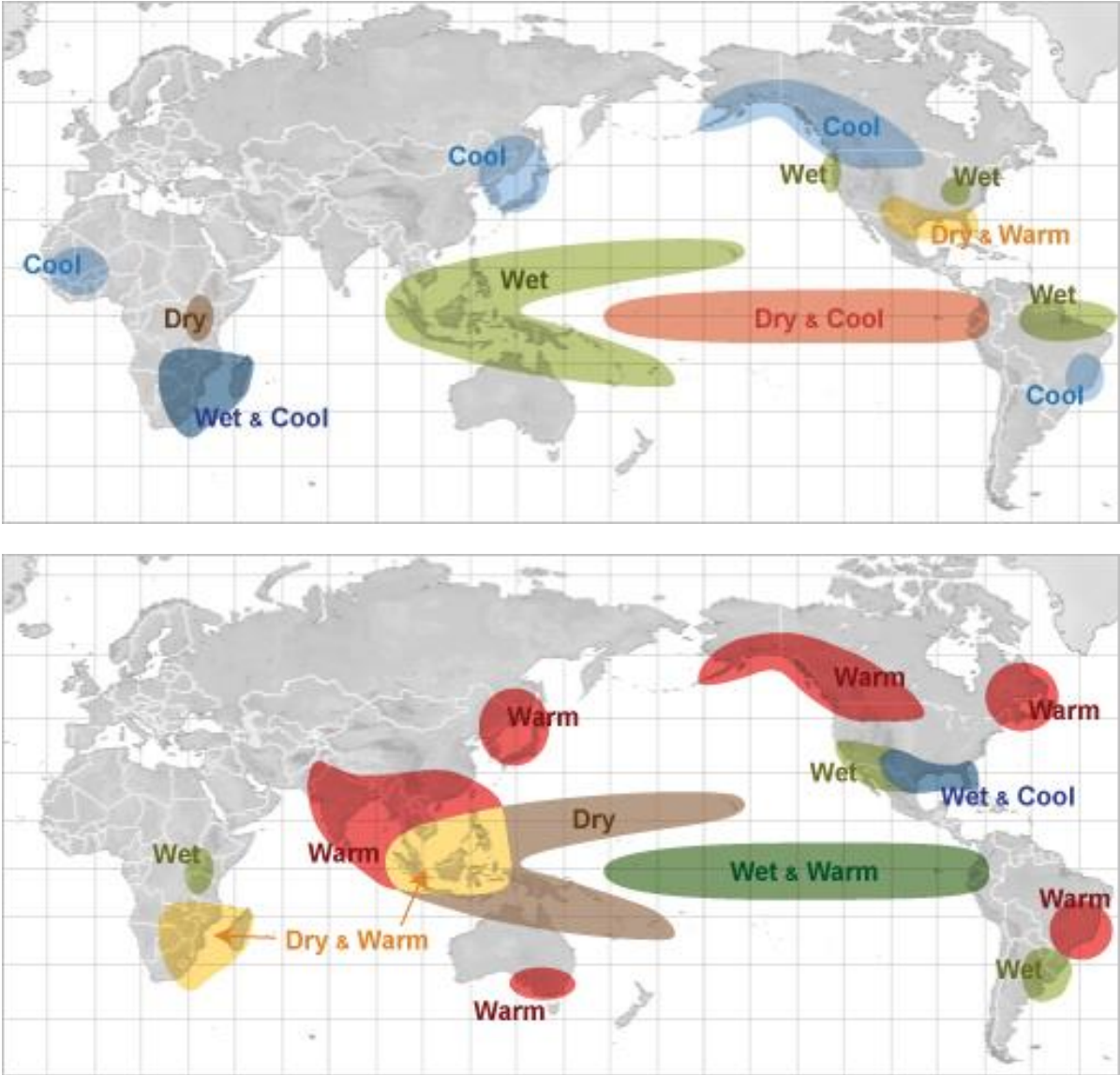


**Figure 2.3:** Global impacts of ENSO on weather and climate: the schematic shows the effects of El Niño in boreal winter. (Source: [http://www.srh.noaa.gov/jetstream/tropics/ens0\\_impacts.htm](http://www.srh.noaa.gov/jetstream/tropics/ens0_impacts.htm))

The ENSO conditions in the equatorial Pacific also have an impact on the global circulation patterns with associated climate impacts in remote regions. Atmospheric interactions between remote regions are defined as teleconnections (Alexander et al. 2002). Tropical influences on the atmospheric circulation are particularly evident in exit regions of the mid-latitude jet (Trenberth et al., 1998).

ENSO is known to influence temperature and precipitation distributions (Ropelewski and Halpert, 1986; Trenberth et al. 2002), frequency of generation of tropical cyclones in the Gulf of Mexico (Kunkel and Angel, 1999), cloud cover (Eastman et al. 2011), and a wide range of meteorological hazards including tornadoes (Schaefer and Tatom, 1998), hurricanes (Pielke and Landsea, 1999), lightning (LaJoie and Laing, 2008), snow pack (Cayan, 1996), and wildfires (Laing and Paxton, 2002). The impacts of ENSO vary spatially and temporally but it should be noted that of course not all weather/climate anomalies are related to ENSO.

**2.1.2 Pacific Decadal Oscillation (PDO)**

The Pacific Decadal Oscillation (PDO) has been described by some as a long-lived El Niño-like pattern of Pacific climate variability (Mantua et al., 1997; Alexander et al., 2010), and a formation of two sometimes independent modes having distinct spatial and temporal characteristics of North Pacific sea surface temperature (SST) variability (Mantua and Hare, 2002) (see Fig. 2.4). A number of studies found only two full PDO cycles within the last century. The “cool” phase is characterized by a cool sector of lower than normal sea surface height and sea surface temperatures in the northeastern and tropical Pacific and a warm horseshoe pattern of higher than normal sea surface heights and sea surface temperatures connecting the north, west and southern Pacific.

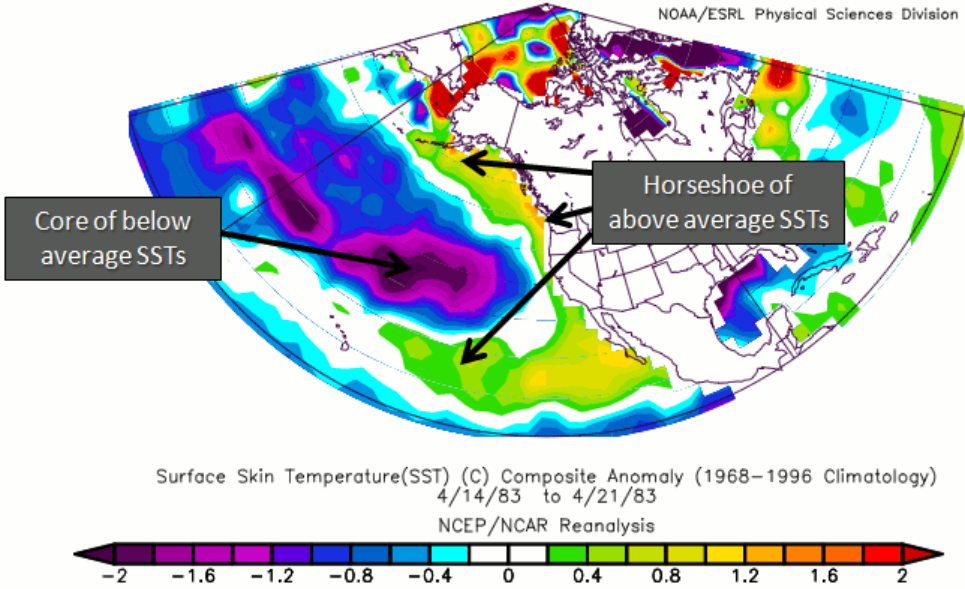


**Figure 2.4:** Typical pattern of the PDO during a warm phase: monthly mean SST anomalies (relative to the climatology 1968-1996) averaged over the period 03/14/1983 and 04/21/1983 (source: <http://climate.ncsu.edu/climate/patterns/PDO.html>).

A “cool” PDO phase was observed from 1890 – 1924 and again from 1947 – 1976, while a “warm” phase appeared from 1925 – 1946 and from 1977 through the mid-1990s (Mantua et al., 1997). The

warm and cold phase can persist for decades. Due to the relatively short time period of instrumental records, it is difficult to assess whether there is a robust frequency peak in the PDO time series. Some studies suggest nominal time scales of ~20 years to nearly ~50 years (Minobe, 1999; Deser et al., 2004). The PDO index after Mantua et al. (1997) is the leading un-rotated empirical orthogonal function (EOF) of monthly North Pacific (20° - 70°N) SST anomalies. The index indicates the prevailing phase and is positive for warm phase conditions, i.e. warm SSTs in the northeastern Pacific.

The climatic and environmental impacts of positive and negative PDO phases are of great importance to fisheries and water resources (MacDonald et al., 2005; Mantua and Hare, 2002). The timing of changes of the PDO phase closely corresponds to that of salmon catch along the west coast of North America (Mantua et al., 1997). The atmosphere also co-varies with the PDO index and the change in location of the cold and warm water masses shifts the path of the jet stream in the northern hemisphere. For that reason, shifts in the PDO phase can have significant implications for global climate, affecting Pacific and Atlantic hurricane activity, droughts and flooding around the Pacific basin, the productivity of marine ecosystems, and global land temperature patterns. In the western North America, positive phases of the PDO are associated with climatic conditions similar to El Niño – although weaker in amplitude. These conditions include decreased winter precipitation, snowpack and streamflow in the northwest and higher precipitation and lower winter temperatures in the southwest. Conditions reverse during negative PDO phases (Mantua and Hare, 2002). The Aleutian low pressure system also fluctuates with the PDO SST variations (Deser et al., 2004). A warm PDO phase features an anomalously deep Aleutian low pressure system. Many studies have tried to determine the physical mechanisms causing the PDO (see review by Alexander, 2010). A recent study by Liu (2012) indicates that the PDO results from changes in wind-driven upper-ocean circulation which is partly forced by atmospheric stochastic forcing and its time scale determined by oceanic Rossby wave propagation in the extratropics. Changes in the Aleutian Low possibly play a key role because the Aleutian Low is a dominant attribute of the atmospheric circulation in the Northern Hemisphere during winter and the variability in its strength and position has a large effect on the atmosphere and ocean in the North Pacific (Latif and Barnett, 1996; Minobe, 1999).

## **2.2 Statistical Methods**

As the modes investigated here (ENSO, PDO) are spontaneously generated by the models, they do not necessarily exhibit the same chronological sequence in the models as in nature. However, their statistical properties (i.e., time scale, empirical orthogonal functions, spectral characteristics, and spatial patterns) should be captured by coupled climate models. Statistical techniques applied in this study are presented, which are necessary to analyse and evaluate simulated natural modes against observations. Additionally, root-mean squared difference (RMSD) and overall mean bias are used, in order to verify the models' skill in realistically representing relevant basic climate variables.

### **2.2.1 Empirical Orthogonal Functions (EOFs)**

The Empirical Orthogonal Functions (EOFs) or Principal Component Analysis (PCA) is a multivariate statistical well-known technique for analysing the variability of a single variable, i.e. a field of only one scalar variable (SST, etc.). The aim of the EOF analysis is to find the linear combination of orthogonal basis functions (“modes”) explaining the variance of a variable. This is accomplished by computing the eigenvectors of the covariance matrix of a data set, which are then sorted in decreasing order. The derived eigenvalues provide a measure of the percent of variance explained by each mode. The first eigenvectors are usually capturing the dynamical behaviour of a system while the other eigenvectors (corresponding to the smallest eigenvalues) are often considered as random noise (Zwiers and Storch, 1999). The EOF analysis gives the spatial patterns of variability, their time variation, and a measure of the “importance” of each pattern.

Gridded climate data is often non-uniformly distributed (e.g., regular longitude-latitude grid), the distribution of data is then denser in high latitudes. This kind of non-uniform distribution can influence the structure of the computed EOFs. In order to avoid this geometrical artefact, the original input data used in this thesis are weighted by the cosine of their latitude after removing the annual cycle. The covariance matrix containing the covariance between the individual grid points is calculated from the weighted data.

Each of the eigenvectors from the EOF analysis can be displayed as a map. These eigenvectors - or EOFs - represent a standing oscillation and do not evolve in time. The EOF patterns only change amplitude (including sign) identifying grid points that vary similarly or oppositely from one another. The time evolution of the amplitude of an EOF shows how this pattern oscillates with time. The weighted anomaly fields are projected onto the spatial EOF pattern to obtain the time series, or principal components (PC). The PCs describe the amplitude of the corresponding EOF at each time. A more detailed explanation can be found in the statistics book by von Storch and Zwiers (1999).

#### **Cautionary Annotation on EOF Interpretation**

Although an EOF analysis gives patterns (sequentially) that can explain most of the observed variance (variability), their interpretation is not always straight forward. Physical interpretability can be controversial, see e.g., Dommenges and Latif (2002), because physical systems are not inevitably orthogonal (Simmons et al. 1983). Additionally, EOFs tend to be domain dependent (Richman 1986) leading to difficulties in their physical interpretability. The constraints enjoined on EOFs are absolutely geometric and thus can be non-physical. Thus, care has to be taken when analysing and interpreting results from any EOF analysis.

### 2.2.2 Spectral Analysis

A commonly used approach to identify dominant periods (or frequencies) in a time series is the spectral analysis. In this study, spectral analysis is applied to PC time series of the EOF modes of interest and to the detrended Nino-3.4 SST time series using the (smoothed) periodogram method (Bloomfield 2000). The periodogram provides a measure of the relative importance of frequency values that can explain an oscillation pattern in a data set. The first step is the subtraction of the sample mean from the time series. The data tapering is a smoothing technique to correct bias established from the finiteness of the data. Finally, a raw periodogram is computed via Fast Fourier Transformation (FFT). A way to improve the estimates by decreasing variance is to use a weighted moving average smoothing technique (Daniell filter, Bloomfield, 2000). To determine the statistical significance of the obtained peaks in the power spectrum, Gilman et al. (1963) have provided a formula for calculating a red noise spectrum that can be used as a reference (null hypothesis) when testing for significance. Using the lag correlation function for a theoretical first-order linear Markov process the lower and upper confidence curves are calculated. Similarly to the EOF analysis, a more detailed description of this spectral analysis method can be found in Zwiers and von Storch (1999).

### 2.2.3 Root-Mean-Square Difference (RMSD) and Overall Mean Bias (OMB)

RMSD and OMB are often used as statistical metrics to assess model performance in climate research studies by comparing a model field (M) with a corresponding reference data set (O) (equation 1). Such metrics have already been implemented in the ESMValTool and used in a study by Righi et al. (2014).

Time averaging and regridding to a common reference grid are necessary pre-processing steps. RMSD then accounts for errors in the spatial pattern and it is calculated as follows:

$$RMSD = \sqrt{\frac{1}{W} \sum_{ij} w_{ij} (M_{ij} - O_{ij})^2} \quad (1)$$

The indices  $i$  and  $j$  correspond to the longitude and latitude dimensions, and  $W$  is the sum of the weights ( $w_{ij}$ ), which for the spatial dimensions are proportional to the grid-cell areas. The weights are therefore approximately proportional to the cosine of latitude (Gleckler et al., 2008).

The OMB is defined as the mean of the weighted differences between the model (M) and the reference field (O) (equation 2).

$$OMB = \frac{1}{W} \sum_{ij} w_{ij} (M_{ij} - O_{ij}) \quad (2)$$

### **3 Tools for Model Evaluation and Implementation**

In this section, a brief description of the Earth System Model Evaluation Tool (ESMValTool) (Section 3.1) and the NCAR Climate Variability Dynamics Package (CVDP) (Section 3.2.1) and its implementation into the ESMValTool are given (Section 3.2.2). Additionally, the newly implemented routines for cloud properties and precipitation are presented. The CVDP has been implemented in the ESMValTool in order to be able to use the ESMValTool capabilities to run on EMAC and CMIP output and to use already existing functions of the tool.

#### **3.1 The Earth System Model Evaluation Tool (ESMValTool)**

The Earth System Model Evaluation Tool (ESMValTool) is a flexible and extensible software package that facilitates the complex evaluation of ESMs. It already includes many diagnostic and performance metrics (Eyring et al., 2015; <http://www.pa.op.dlr.de/ESMValTool/>). The tool can be used to evaluate single models (or different versions of a model), as well as multiple models from the Chemistry-Climate Model Initiative (CCMI, (Eyring et al., 2013)), the Coupled Model Intercomparison Project (CMIP), and other Model Intercomparison Projects that use CMOR-compliant (Climate Model Output Rewriter) output. A reformatting routine is already implemented in the ESMValTool that converts the native EMAC output to the CMOR standard required by the ESMValTool. The ESMValTool is designed in such a way that the code allows for further extensions to be made by different developers for different applications and types of ESMs. Embedded in a subversion-controlled repository, the implementation of extensions and additional analysis is straightforward. Its core routines are currently based on Python, however diagnostics and plot routines can be implemented in the open source languages NCL (National Center for Atmospheric Research (NCAR) Command Language), R, and Python.

#### **3.2 NCAR Climate Variability Diagnostics Package (CVDP)**

##### **3.2.1 Brief Description of CVDP**

The Climate Variability Diagnostics Package (CVDP) developed by the National Center for Atmospheric Research (NCAR) Climate Analysis Section (Phillips et al., 2014) version 3.7.0 has been implemented into the ESMValTool in order to be able to run CVDP alongside the Earth System Grid Federation (ESGF) on output from the Coupled Model Intercomparison Project (CMIP). The implementation of the CVDP into the ESMValTool accomplished in the context of this thesis also allows for using the ESMValTool's reformatting routines, i.e., output from the atmospheric chemistry model EMAC can be analyzed easily together with results from CMIP models.

CVDP can be used to evaluate the major internal modes of climate variability including coupled ocean-atmosphere phenomena such as El Niño and the Southern Oscillation, Pacific Decadal Oscillation, Atlantic Multi-decadal Oscillation (AMO), as well as prominent modes of regional and hemispheric atmospheric circulation variability namely Northern and Southern Annular Modes, North Atlantic Oscillation (NAO), Pacific North and South American teleconnection patterns, as well as global trend maps and index time series. Furthermore, time series and running decadal trends of global mean temperature and precipitation are also calculated to assess rates of global warming and changes in the hydrological cycle strength over time. Finally, interannual standard deviation maps give a more general view of the spatial characteristics and amplitudes of variability. CVDP is developed as a standalone tool outside the ESMValTool (see <https://www2.cesm.ucar.edu/working-groups/cvcwg/cvdp> for details on the CVDP). In order to be able to update CVDP in the ESMValTool once a new release is available the structure of the CVDP was kept as is and a wrapper has been written to be able to run CVDP directly within the ESMValTool. The CVDP produces plots that can be in postscript (ps) or portable network graphics (png) format. The CVDP output can also be compiled into a website including a table summarizing the model performance for 11 key metrics of internal climate variability on the basis of pattern correlations and calculation of root-mean square errors with the respect to the chosen observational reference data.

### **3.2.2 Implementation of CVDP into the ESMValTool**

The ESMValTool is configured and run via providing a set of text files, so called “namelists”, that specify the input data to be used (models and observations), the diagnostics and metrics to be calculated and the output to be generated. In order to implement CVDP into the ESMValTool, a new namelist (*namelist\_CVDP*) has been written that runs the CVDP within the ESMValTool environment. The CVDP has been implemented in a way that allows easy upgrading to newer versions of CVDP once available. Figure 3.1 shows a schematic overview of the ESMValTool - CVDP coupling.

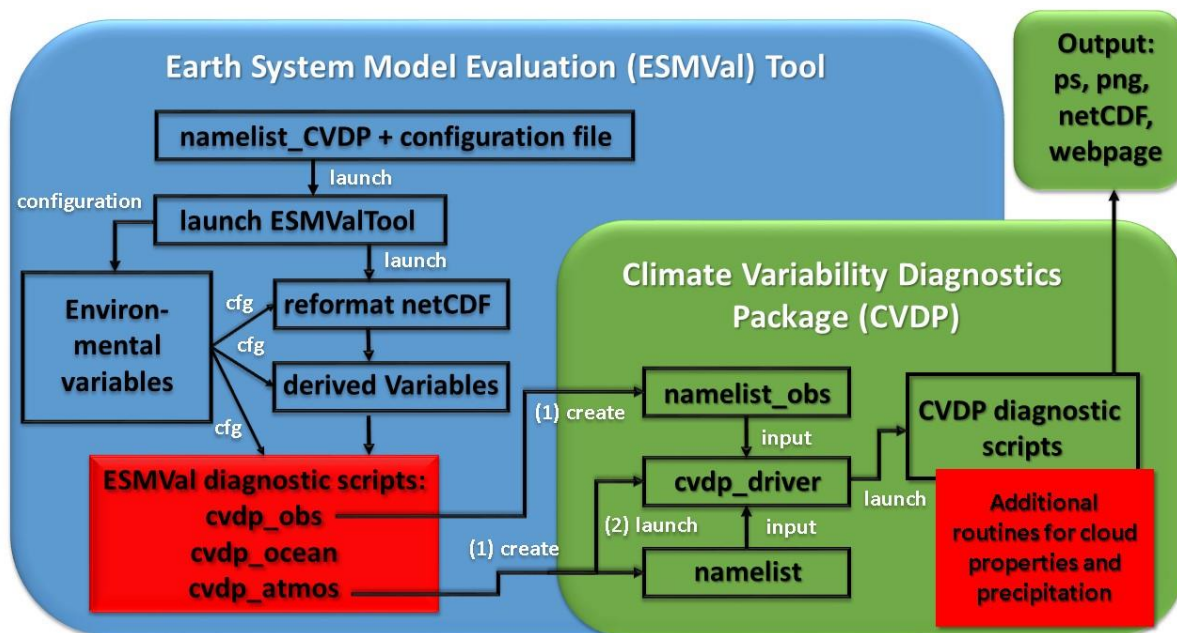


**Figure 3.1:** Schematic of the coupling of the CVDP to the ESMValTool. New routines for cloud properties and precipitation are part of the CVDP diagnostics scripts and are executed within the CVDP.

The ESMValTool-CVDP combination is launched by calling the ESMValTool’s main Python routine (workflow manager) with the *namelist\_CVDP*, which contains global settings and defines the models, observational data sets and diagnostics to be analyzed. First, the input netCDF data are reformatted to be compliant with the CMOR standard and, if required derived variables are calculated. Then, a climatology for the data sets specified in the namelist (models and observations) is calculated. The workflow manager passes these climatologies to the newly implemented ESMValTool diagnostic scripts (*cvdp\_obs*, *cvdp\_atmos*, *cvdp\_ocean*) (red box in Fig. 3.1) that effectively rename the reformatted input data to be used as input with CVDP. It is necessary to have the file names of the model and the observational data in the correct format before launching the CVDP (*cvdp\_driver*). The ESMValTool diagnostic *cvdp\_atmos* writes the information about which set of model data is passed to the CVDP into the CVDP *namelist* textfile. The information includes names of the models, the start and end year, as well as the pathnames of the model data. To compare the models with observations a separate CVDP *namelist\_obs* is necessary. This textfile is generated by the ESMValTool diagnostic *cvdp\_obs* and contains the same information as the textfile for *cvdp\_atmos*, but for observations. User-adjustable options are located in *cvdp\_driver* (includes CVDP configuration file) and *cfg\_cvd* (ESMValTool configuration file). For example, the user can decide if the selected calculated data is written in a netCDF file or if monthly atmospheric modes of variability are computed. Finally, the CVDP is launched within the ESMValTool by *cvdp\_atmos* and generates the output files.

### 3.3 Additional Routines for Cloud Properties and Precipitation

Additional diagnostics have been developed and implemented into the ESMValTool-CVDP in order to investigate the response of the atmospheric hydrological cycle to the modes of climate variability (particularly sea surface temperature) and to assess the performance of EMAC and selected CMIP5 models in reproducing the observed response. The new diagnostic files are part of the original CVDP diagnostic scripts, and are executed within the *cvdp\_driver* (Fig. 3.1).

Two different diagnostics are implemented into the ESMValTool-CVDP and used in this master thesis:

In the first diagnostic, Nino-3.4 composite plots for precipitation, total cloud amount, and liquid water path are generated. This includes the following steps:

The first step is the removal of the annual cycle from the monthly mean raw input data to obtain the temporal anomalies at each grid point. In order to avoid potential problems with the analysis caused by the effects of global warming, the linear trend (if present) is estimated via the least square method and is subsequently removed from the time series of monthly anomalies. A 3-month seasonal running mean of the variables precipitation, total cloud amount, and liquid water path is then calculated.

The standardized Nino-3.4 index averaged over the months November, December, and January is used as an indicator, when an ENSO event reaches its peak. El Niño years are selected and saved, if the Nino-3.4 SST index exceeds the value +1. This is similarly done for La Niña events (Nino-3.4 index less than -1).

The El Niño and La Niña events are separately averaged over a 24-month period to capture the full temporal and spatial evolution of the ENSO events, beginning with the onset and followed by the peak and the decay. In order to analyze the differences between El Niño and La Niña, the differences between the two are calculated. These differences are visualized as a seasonal latitude-longitude contour plot showing anomalies in the hydrological atmospheric components during ENSO. This diagnostic is applied in section 5.2.3.2 *Composite El Niño and La Niña Events* (see for example Figure 5.14) and 5.2.3.3 *Global Teleconnections* (see for example Figure 5.15).

The second diagnostic combines time series of local SST anomalies, the PDO index, and the Nino-3.4 index with time series of anomalies in precipitation, total cloud amount, and liquid water path in certain regions to investigate possible correlations. The following steps were applied:

The annual cycle is removed from the monthly mean raw input data to obtain the temporal anomalies at each grid point. To avoid global warming effects in the data, the linear trend is estimated via the least square method and removed.

The monthly PDO time series is defined as the leading principal component (PC) of the North Pacific (20°-70°N, 110°E-100°W) area-weighted SST anomalies. The Nino-3.4 index (5°S-5°N, 120°-170°W)

time series, the local sea surface temperature, precipitation, total cloud amount, and liquid water path are area-weighted with the cosine of the latitude. To reduce high frequency noise in the individual time series, a 12-month running mean is applied. Additionally, the linear cross-correlations (lag zero) are calculated between two investigated time series. This diagnostic is applied in section 5.3 *Regional Impacts of ENSO or PDO on precipitation and cloud properties* (see for example Figure 5.20).

### **Important Notes if a new CVDP Version is released**

Since the new implemented diagnostics are need to be kept in the CVDP, even if a new version of CVDP replaces the older one in the ESMValTool-CVDP combination, the following steps have to be taken in account.

1. The variables stay the same and there are only modifications within the existing CVDP diagnostic files of the older CVDP version. In this case, the user only replaces the modified diagnostic files.
2. The variables stay the same and there are totally new CVDP diagnostics in the new CVDP version. In this case, the new diagnostic files need to be copied in the CVDP diagnostics folder and file names are added in the *cvdp\_driver.ncl* that they are executed in the ESMValTool-CVDP combination.
3. A new variable is added within the new version and there are modifications within the existing CVDP diagnostics files and/or totally new CVDP diagnostics. In this case, the diagnostic files need to be copied and are replaced in the CVDP diagnostics folder. The CVDP executing file *driver.ncl* is copied in the ESMValTool folder *diag\_scripts* and must be renamed in *cvdp\_driver.ncl*, that the file will be detected by the ESMValTool diagnostic *cvdp\_atmos*. Additionally, the user adds the variables (LWP, CLT (TCA)) and files names of the routines for cloud properties and precipitation implemented in this thesis in the new *cvdp\_driver.ncl*. Furthermore, the user complements these variables (LWP, CLT (TCA)) in the new CVDP diagnostics files *namelist.ncl* and *functions.ncl*. The lines of code can be taken from the older *namelist.ncl* and *functions.ncl*. The order of the rows of the variables must be adopted in the *cfg\_cvdp* (ESMValTool).

## **4 Models, Model Simulations and Observations for Evaluation**

### **4.1 Models**

#### **4.1.1 Max Planck Institute Earth System Model (MPI-ESM)**

The MPI-ESM is a further development and improvement of the ECHAM5/MPIOM coupled model (Jungclaus et al., 2006) from the Max Planck Institute for Meteorology (MPI-M) in Hamburg, Germany. The model couples processes in the atmosphere, the ocean and the land surface through exchange of energy, momentum, water and other trace gases like carbon dioxide. It consists of four model components namely the coupled general circulation models for the atmosphere and ocean, i.e., the European Centre-Hamburg atmosphere model (ECHAM6) (Stevens et al., 2013) and the Max Planck Institute ocean model (MPIOM) (Jungclaus et al., 2013), and the submodels for land and vegetation, the Jena Scheme for Biosphere Atmosphere coupling in Hamburg (JSBACH) (Reick et al., 2013; Schneck et al., 2013) and the marine biogeochemistry component Hamburg ocean Carbon Cycle Model (HAMOCC5) (Ilyina et al., 2012). The coupling between atmosphere and land processes, and between ocean and biogeochemistry is handled by the Ocean Atmospheric Sea Ice Soil (OASIS3) coupler.

The low resolution (LR) configuration uses for the atmosphere a T63 ( $\sim 1.9^\circ \times 1.9^\circ$ ) horizontal resolution and 47 hybrid sigma-pressure levels, and for the ocean a bipolar grid with  $1.5^\circ$  resolution (near the equator) and 40 z-levels. The poles of the ocean model are moved over Greenland and the coast of the Weddell Sea by a conformal map of the geographical grid. MPI-ESM-LR has the same spatial resolutions in the atmosphere and ocean as ECHAM5/MPIOM used within CMIP3, except for the vertical grid in the atmosphere. The L47 vertical grid extends from the surface to 0.01 hPa, while the L31 grid of the old version of the model (ECHAM5) extended up to 10 hPa. Between the surface and 100 hPa, however, both vertical grids are identical. This vertical extension of the atmospheric grid includes for the first time the stratosphere in CMIP simulations at MPI-M, in order to capture the high variability of the high latitude circulation in the middle atmosphere, which dynamically influences the tropospheric circulation below (Karpechko and Manzini, 2012). The time steps in the atmosphere and in the ocean are 600 and 4320 s, respectively.

#### **4.1.2 ECHAM/MESSy Atmospheric Chemistry Model (EMAC)**

The ECHAM/MESSy Atmospheric Chemistry (EMAC) model is a lower to middle atmosphere (MA) atmospheric chemistry general circulation model. As a chemistry-climate model it couples chemical and dynamical processes in the atmosphere and is typically used for multi-decadal chemistry and climate simulations. The model uses a modular structure that combines several different submodels

describing the different processes in the atmosphere as well as the interactions between the atmosphere, the ocean and land masses. Additionally, anthropogenic emissions of trace gases and particles are taken into account in the model (Jöckel et al., 2015). Currently, the 5<sup>th</sup> generation of the general circulation model ECHAM (Roeckner et al., 2006) serves as base model and represents the dynamical core of the atmospheric model. The different submodels are linked together via the Modular Earth Submodel System (MESSy, Jöckel et al., 2010) offering the possibility to couple multi-institutional codes with great flexibility.

The T42 horizontal resolution of the simulations analyzed in this work corresponds to a Gaussian grid of approximately  $2.8^\circ \times 2.8^\circ$  in longitude and latitude. The atmosphere is discretized in 90 hybrid-pressure layers resolving the atmosphere up to a pressure of 0.01 hPa (80 km). The model time step in this configuration is 720 s (Jöckel et al., 2006, 2015).

## 4.2 Model Simulations

**Table 4.1:** Model simulation analyzed in this thesis.

	<b>SSTs</b>	<b>Time period</b>	<b>Nudging</b>
<b>MPI-ESM coupled</b>	Coupled	1850 – 2005	---
<b>MPI-ESM AMIP</b>	Prescribed from HadISST	1979 – 2005	---
<b>EMAC RC1-base-07</b>	Prescribed from HadISST	1950 – 2010	---
<b>EMAC RC1SD-base-10</b>	Prescribed from ERA-Interim	1979 - 2013	sea level pressure, divergence, vorticity, temperature

### 4.2.1 Max Planck Institute Earth System Model (MPI-ESM)

In this thesis, two different simulations with the MPI-ESM are analyzed. First, the CMIP5 “historical” experiment (MPI-ESM coupled) simulating the climate from 1850 to 2005 with the coupled atmosphere-ocean model prescribing the best estimates of natural and anthropogenic forcings. The prescribed natural forcing includes variations in the Earth orbit, variability in solar irradiance, seasonally varying natural tropospheric aerosols, and stratospheric aerosols from volcanic eruptions. The anthropogenic forcing from emissions of greenhouse gases, aerosols, land use changes, etc. is also included in the model setup (Giorgetta et al., 2013).

Second, the “AMIP” experiment covering the time period from 1979 to 2005 using the same boundary conditions for atmosphere and land as the historical experiment up to 2005. Here, the model is run in an atmosphere-only configuration with prescribed SSTs. For the years 2006 through 2008 the forcings from the representative concentration pathway 4.5 (RCP4.5) scenario have been used. The prescribed SSTs and sea ice concentrations (PCMDI, <http://www.pcdmi.gov/projects/amip/>) have been linearly interpolated between the midpoints of the months to the actual time in the model.

#### **4.2.2 ECHAM/MESSy Atmospheric Chemistry Model (EMAC)**

As a contribution to the Chemistry-Climate Model Initiative (CCMI) (Eyring et al., 2013), a free-running hindcast simulation from 1950 to 2010 (RC1-base-07) and a hindcast simulation with specified dynamics from 1979 to 2013 (RC1SD-base-10) has been performed.

The EMAC RC1SD-base-10 simulation analyzed in this work was nudged applying a Newtonian relaxation technique towards ECMWF reanalysis data (ERA-Interim, Dee et al., 2011). These reanalysis data are obtained through assimilation of a large variety of available observations.

The EMAC RC1SD-base-10 simulation uses prescribed SSTs taken from the ERA-Interim reanalysis, the variables sea level pressure, temperature, vorticity, and divergence are nudged, resulting in atmospheric conditions similar to the reanalysis data. The nudging is only applied in the free troposphere, the boundary layer, which consists of the three lowest layers in EMAC, and the stratosphere are not modified. To avoid spurious effects resulting from differences in the model used to generate the ERA-Interim reanalysis (IFS) compared to EMAC, the nudging modifies the variables listed above only with a modest strength in order to keep the simulation “on track”, but allows the model to develop a self-consistent state. SSTs in the free-running EMAC RC1-base-07 are prescribed following the global data set HadISST (Rayner et al., 2003). The hydrological cycle is free-running in both EMAC simulations (Jöckel et al., 2015).

#### **4.3 Observational Data for Model Evaluation**

A variety of different observations are used for the model evaluation. For each of the variables assessed in this work (near-surface air temperature, sea surface temperature, sea level pressure, precipitation, total cloud amount, and liquid water path), an observational data set was selected. A brief description of the data is given in this section. Follow-up studies could additionally assess how observational uncertainty influences the results by using alternative datasets.

**Table 4.2:** Used observational data sets.

<b>Data set</b>	<b>Variable</b>	<b>Type</b>	<b>Time period</b>	<b>Reference</b>
<b>HadISST</b>	Sea surface temperature	In-situ, reanalysis	1850 - present	Rayner et al., 2003
<b>NCEP/NCAR</b>	Near-surface air temperature	reanalysis	1948 - present	Kalnay et al., 1996
<b>ERA-Interim</b>	Near-surface air temperature, sea level pressure	reanalysis	1979 - present	Dee et al., 2011
<b>GPCP-SG</b>	Precipitation	Satellite, rain gauge	1979 - present	Huffman et al., 1997
<b>ISCCP-D1</b>	Total cloud amount	Satellite	1984 - present	Rosow and Schiffer, 1999
<b>UWisc</b>	Liquid water path	Satellite	1988 - 2007	O'Dell et al., 2008

### **Near-Surface Air Temperature and Sea Level Pressure**

The two reanalysis data sets ERA-Interim and National Centers for Environmental Prediction (NCEP)/NCAR are used for comparison with simulated monthly near-surface air temperatures, and ERA-Interim data set for comparison with modelled sea level pressure. Meteorological reanalyses are assimilations of historical observational data that span an extended period of time.

ERA-Interim reanalyses are produced by the European Centre for Medium-Range Weather Forecast (ECMWF). ERA-Interim reanalysis data cover the period from 1979 to present, and uses cycle 31r2 of ECMWF's Integrated Forecast System (IFS) (Dee et al., 2011). Observations used in the reanalysis are subject to quality control, selection steps (e.g., to remove duplicate data or data that are known to have large errors) and bias corrections (Dee et al., 2011).

The NCEP/NCAR reanalysis used in this thesis covers the time period from 1948 to the present (Kalnay et al., 1996). Over this period, the availability of observations improved, particularly when satellite observations became available in the 1970s. NCEP/NCAR is used as the main reference data set for the near-surface air temperature in this thesis.

## **Precipitation**

In the precipitation diagnostics, the Global Precipitation Climatology Project (GPCP) observational data set “GPCP-SG” has been used as reference. GPCP-SG is the combined monthly Satellite Gauge (SG) data set for the monthly precipitation estimates on a  $2.5^\circ \times 2.5^\circ$  grid from 1979 to present. The combination of satellite-based rainfall estimates provides the most complete analysis of rainfall available over the global oceans, and additional necessary spatial detail to the rainfall analysis over land. This therefore provides global coverage. In the current version 2.2 the Special Sensor Microwave Imager Sounder (SSMIS) satellite data are included (Huffman and Bolvin, 2013). The GPCP combined precipitation data are provided by the NASA/Goddard Space Flight Center’s Laboratory for Atmospheres, which develops and computes the data set as a contribution to the GEWEX Global Precipitation Project (Huffman et al., 1997). Nijsson et al. (2001) found that the GPCP-SG underestimate precipitation in some regions with complex orography. This underestimation is mainly related to missing rain gauge data. The satellite observations also have difficulty to see orographic rainfall. Over the ocean, there is a general lack of rain gauge data. Errors in precipitation estimates also occur due to the combination of different satellites. The rainfall rates over the ocean therefore still have large uncertainties (Adler et al., 2003).

## **Sea Surface Temperature**

For the evaluation of the simulated SST, the Hadley Centre’s sea ice and sea surface temperature (HadISST) data set is used [<http://www.metoffice.gov.uk/hadobs/hadisst/>]. It is a combination of monthly SST fields with global coverage on a  $1^\circ \times 1^\circ$  longitude-latitude grid from 1871 to present (Rayner et al., 2003). The HadISST data are reconstructed using reduced space optimal interpolation applied to SSTs from the Marine Data Bank (mainly ship measurements) and the International Comprehensive Atmosphere-Ocean Data Set (ICADS) through 1981, and then a combination of in-situ and satellite-derived SSTs. SSTs near sea ice are estimated using statistical relationships between SST and sea ice concentration. A weakness of this data set is the sparse observational data in polar regions (<https://climatedataguide.ucar.edu/climate-data/sst-data-hadisst-v11>).

## **Total Cloud Amount**

For total cloud amount (TCA), the observations from the International Satellite Cloud Climatology Project (ISCCP) are used. ISCCP uses infrared and visible radiances from imaging radiometers. These instruments are aboard of operational weather satellites to provide a long-term (1984-2009) global record of cloud properties.

The stage D1 product of ISCCP is produced by summarizing the pixel-level results every 3 hours on an equal-area map with 280 km resolution and merging the results from separate satellites with the

atmospheric and ice/snow data sets to produce global coverage at each time (<http://isccp.giss.nasa.gov/>). In this analysis, monthly means are used.

The TCA from ISCCP is estimated to be about 10 % too low over land and “about right” over the ocean (Rossow and Schiffer, 1999).

### **Liquid Water Path**

For the evaluation of the liquid water path (LWP), the University of Wisconsin LWP climatology (UWisc) is used. This climatology is derived from satellite-based passive microwave observations over the global oceans and includes data from the Special Sensor Microwave Imager (SSM/I), the Tropical Rainfall Measuring Mission (TRMM) Microwave Imager (TMI), and the Advanced Microwave Scanning Radiometer for Earth Observing System (EOS) (AMSR-E) in the years 1988–2007 (O’Dell et al., 2008). In this LWP climatology, the diurnal cycle of the data has been removed by using a combination of different instruments with different overflight times. Therefore, the data set is well suited for the evaluation of monthly means.

O’Dell et al. (2008) give potential systematic errors in the LWP climatology of the order of 15%–30%.

## 5 Results

### 5.1 Evaluation of the Mean State

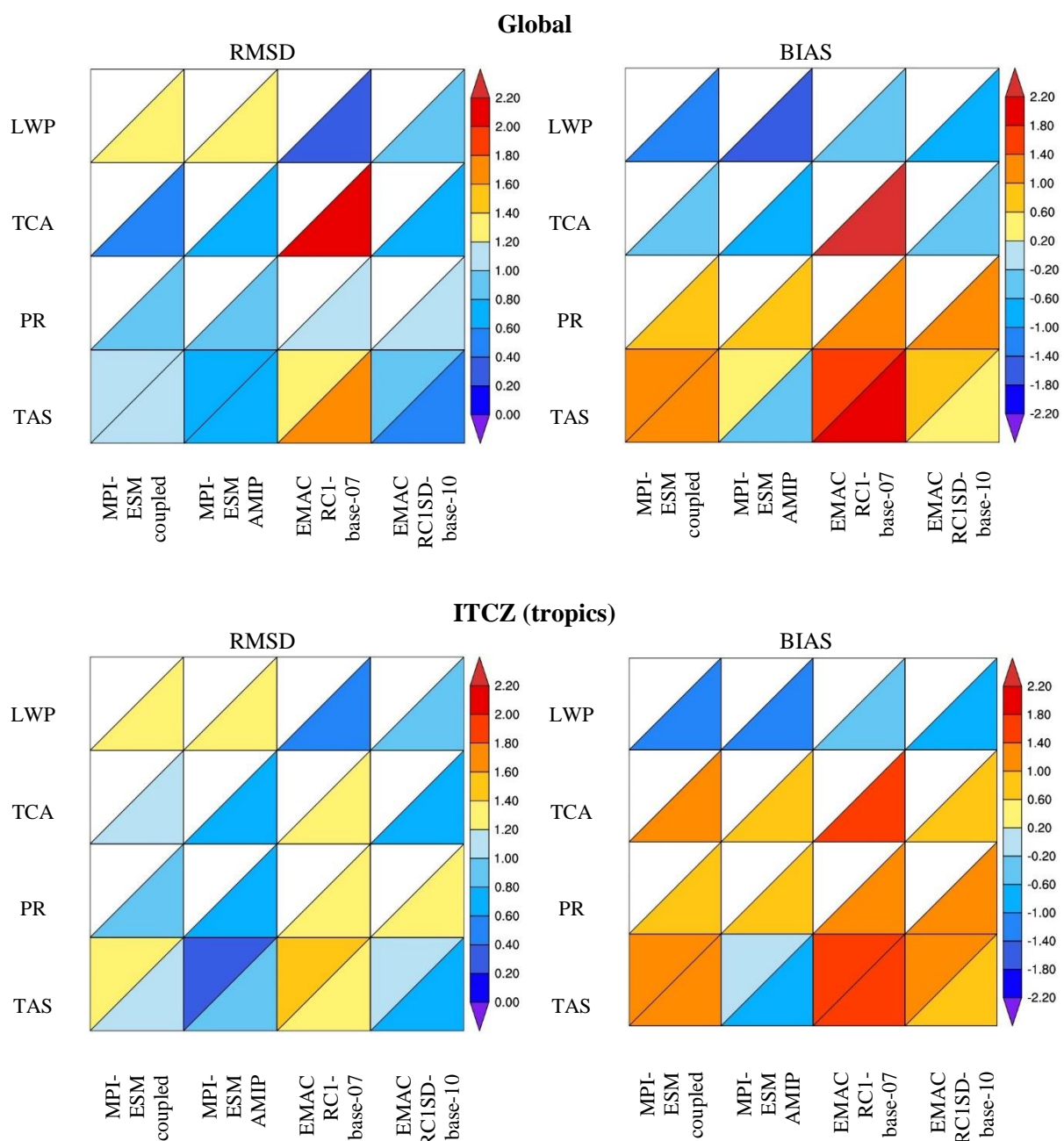
Before evaluating and analysing the impact of the climate modes PDO and ENSO on cloud properties and precipitation, the performance of the models in reproducing the related observed basic climate variables is assessed. Such knowledge on the models' skill in realistically representing relevant basic climate variables is needed to evaluate, assess and interpret the simulation results later. For example, if the simulated cloud distribution in a model is not realistic, no realistic response of these clouds to climate variabilities can be expected and vice versa.

In order to evaluate the basic climate parameters near-surface air temperature, precipitation, total cloud amount, and liquid water path, an existing diagnostic of the ESMValTool (Righi et al., 2014) is used that calculates and plots the annual mean for all years and each model based on monthly mean fields. Differences with respect to the observational data are calculated to assess the performance of the models.

A comparison of a coupled atmosphere-ocean and an atmosphere-only simulation with MPI-ESM is done to identify biases in the atmospheric component of the MPI-ESM model. In order to quantitatively assess and compare the ability of the different model simulations in reproducing key features of the observed climate, statistical measures are calculated in addition to the diagnostic plots. For each diagnostic, the root-mean-square difference (RMSD) and the overall mean bias are calculated. The applied RMSD and bias metrics are calculated from the space-time fields (latitude, longitude plus annual cycle). Following Gleckler et al. (2008), the RMSD (Fig. 5.1 left panel) and overall mean bias (Fig. 5.1 right panel) in the modelled annual cycle of the atmospheric variables near-surface temperature (TAS), precipitation (PR), total cloud amount (TCA) and liquid water path (LWP) are calculated for four domains with a focus on the Pacific (global, ITCZ (tropics) (0.5°S-13.5°N, 136°E-80°W), northeast Pacific (NEP) mid-latitudes (20°-50°N, 110°-140°W), southeast Pacific (SEP) stratocumulus region (12.5°-33:5°S, 70°-90°W)) and are summarized in portrait plot diagrams. These plots provide a summary of the models' relative errors using "portrait" diagrams in which the different colours indicate the size of error. The portraits are arranged such that the rows are labelled by the variable name and the columns by the name of the model simulation. Positive (negative) values for the mean bias indicate that the model overestimates (underestimates) the observations. In order to compare the relative performance of the simulations, the RMSD and overall mean bias are normalized by dividing through the multi-model average bias.

In the global domain and the tropical region, the nudged (RC1SD-base-10) and the free-running (RC1-base-07) EMAC simulations perform similarly in reproducing the observed cloud climatology, with the only exception that the free-running simulation strongly overestimates the global average total cloud amount. While EMAC RC1-base-07 overestimates cloud water compared with the observations

in the NEP midlatitudes, the nudged model simulation shows too little cloud water. The coupled and the AMIP simulations from MPI-ESM produce similar biases in the atmospheric variables TAS, PR, TCA, and LWP in the geographical distribution. In three of the four regions, the MPI-ESM coupled and the MPI-ESM AMIP underestimate total cloud amount (Global, NEP midlatitudes, SEP stratocumulus). In all four regions, both MPI-ESM simulations overestimate precipitation and underestimate liquid water path. The positive biases in precipitation range from 0.6 to 2.0 mm day<sup>-1</sup> and the negative biases in liquid water path from -0.20 to -1.80 g m<sup>2</sup>. Additionally, the analysis has also been applied to 21 coupled ocean-atmosphere CMIP5 models (not shown) to assess the skill of the coupled MPI-ESM. The majority of the CMIP5 models produce similar biases in the atmospheric in the four regions.



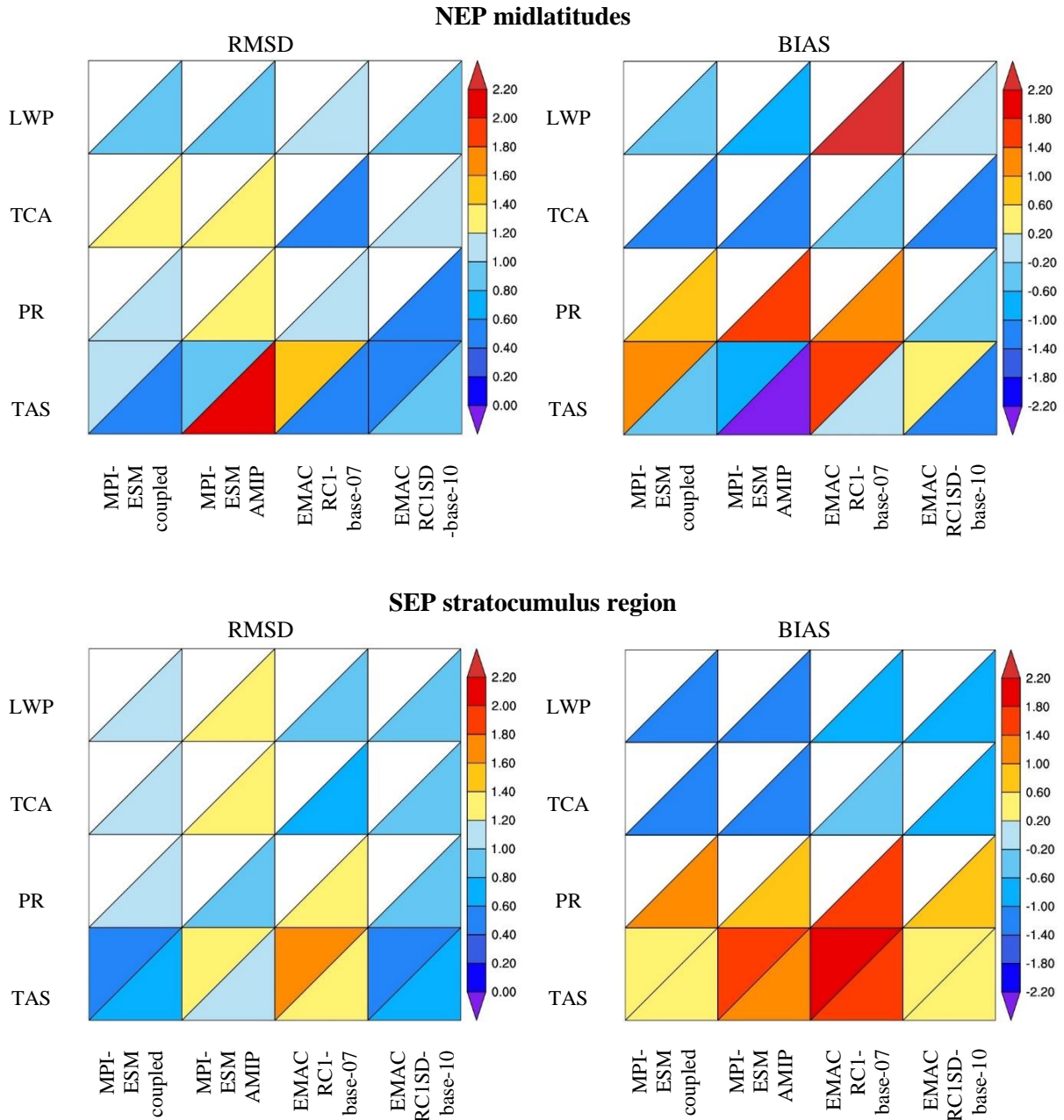


**Figure 5.1:** Root-mean-square difference (left) and overall mean bias (right) of precipitation (PR), near-surface air temperature (TAS), cloud liquid water path (LWP), and total cloud amount (TCA) averaged over the global domain, the tropics, NEP midlatitudes and southeast Pacific stratocumulus regions. Columns and rows represent the EMAC and CMIP5 simulations and the variables/regions analysed, respectively. The diagram boxes are split in two parts, showing the model performance compared to the primary (lower triangle) and alternative (upper triangle) observational data set (Tab. 4.2). Where no alternative observations are available, the upper triangles are marked white.

### 5.1.1 Evaluation of Annual Mean Near-Surface Air Temperature

Figure 5.2 depicts the differences between the 21-yr annual average NCEP reanalysis and the different model simulations for near-surface air temperature (TAS). The reanalysis data and the models are averaged over the period 1984 - 2005. The Student's t-test analysis was employed to calculate the statistical significance of the model biases. For the simulations with prescribed SSTs (MPI-ESM AMIP, EMAC RC1-base-07, and EMAC RC1SD-base-10), only the land temperatures are analysed as the differences between SSTs and TAS are very small over the ocean and not significant.

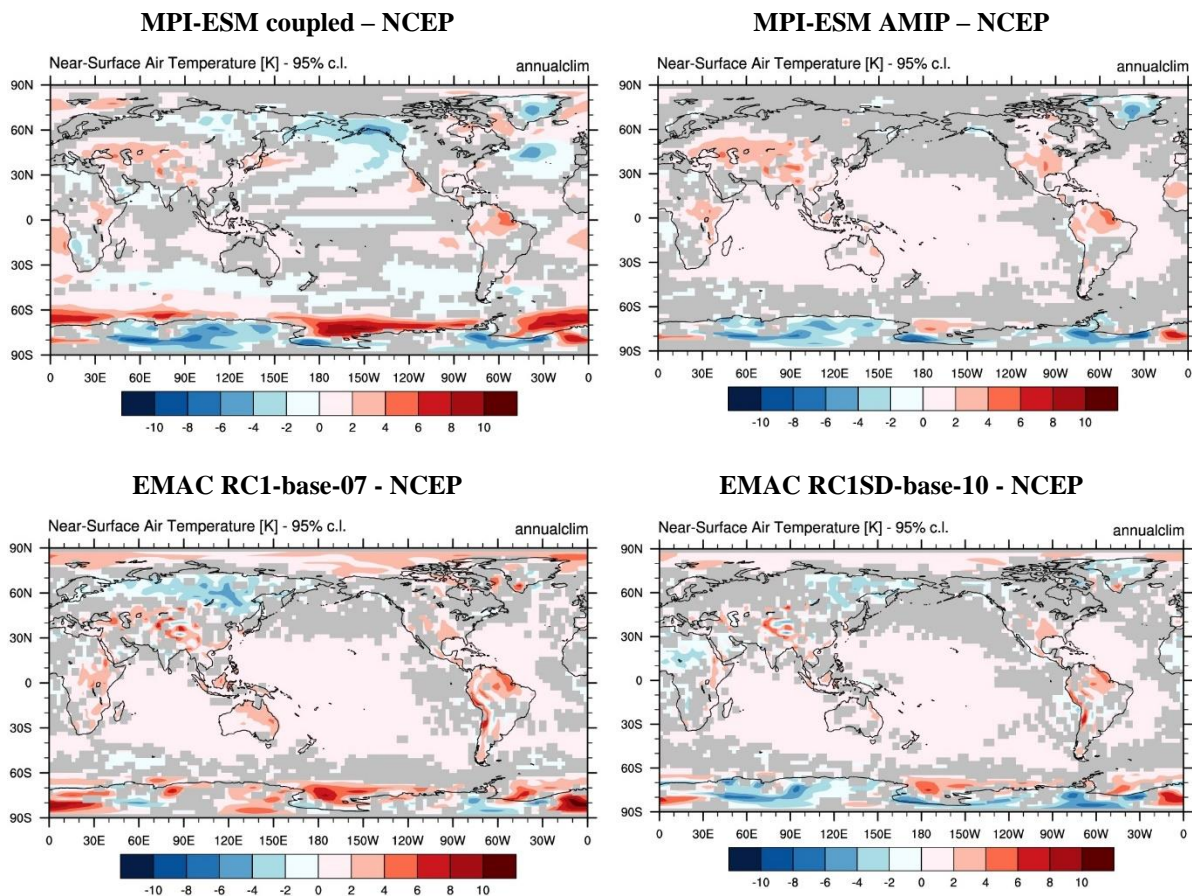


**Figure 5.2:** The difference plots between 21-yr average near-surface air temperature (TAS) (1984-2005) in Kelvin from NCEP reanalysis data (top) and the 4 different model simulations. MPI-ESM AMIP, EMAC RC1-base-07, and EMAC RC1SD-base-10 simulations use prescribed SSTs (only the land areas are analysed). Biases exceeding the 95 % level of statistical significance based on Student's t test are coloured in red and blue.

The statistical significance at the 95 % level, according to a t-test shows that the biases in the simulations are believable over land for example in mountainous regions and the Siberian lowland, even though their global means are in close agreement with the reanalysis (Tab. 5.1). Biases are found in the mountainous areas, such as the Rocky Mountains, the Tibetan Plateau, the Andes, Greenland and Antarctica, which might be related to the rather coarse representation and incorrect height of these

topographic features in the models leading to differences between the real and the model surface elevation in these regions. The maximum warm bias in the models is found over the Tibetan Plateau with differences up to 6 °C. Large biases in higher elevations are typical for coupled climate models (IPCC 2013). A strong cold bias of 6 °C is found in the free-running EMAC RC1-base-07 simulation over the Siberian lowland. Nevertheless, the models show a good agreement in simulating the geographical pattern of the annual mean near-surface temperature with spatial correlation coefficients up to values close to 1. The RMSE of the annual mean values lies between 1.6 °C (coupled MPI-ESM) and 2.2 °C (EMAC RC1-base-07) compared to the NCEP reanalysis.

**Table 5.1:** Statistics of global average multi-year mean near-surface air temperature [°C] over land, averaged over the years 1984-2005.

	<b>NCEP</b>	<b>ERA-Interim</b>	<b>MPI-ESM coupled</b>	<b>MPI-ESM AMIP</b>	<b>EMAC RC1-base-07</b>	<b>EMAC RC1SD-base-10</b>
<b>Annual mean 2m air temperature [K]</b>	9.2	9.4	9.3	10.0	10.0	9.4
<b>Pattern correlation</b>		1.00	1.00	1.00	0.99	1.00
<b>Root-mean-square error (RMSE) [K]</b>		1.6	1.7	1.8	2.2	1.9

The RMSE of annual mean near-surface temperature from the MPI-ESM coupled simulation is 1.5 °C over the ocean. For comparison, the RMSE of ERA-Interim over the ocean is 0.7 °C (reference data set: NCEP reanalysis). Over the ocean, the biases in TAS closely resemble the biases in the SST (Fig. 5.6 b), underlining the strong influence of the SST on near-surface air temperature.

**Table 5.2:** Statistics of global average multi-year mean near-surface air temperature [°C] over the ocean, averaged over the years 1984-2005.

	<b>NCEP</b>	<b>ERA-Interim</b>	<b>MPI-ESM coupled</b>
<b>Annual mean near-surface air temperature [°C]</b>	16.1	16.4	16.4
<b>Pattern correlation</b>		1.0	1.0
<b>Root-mean-squared error (RMSE) [°C]</b>		0.7	1.5

### 5.1.2 Evaluation of Annual Mean Precipitation

Figure 5.3 displays the mean spatial pattern of the annual precipitation ( $\text{mm day}^{-1}$ ) from GPCP-SG satellite data (top), and the differences between the model simulations and GPCP-SG observations (below) showing biases in the modelled annual mean precipitation rates.

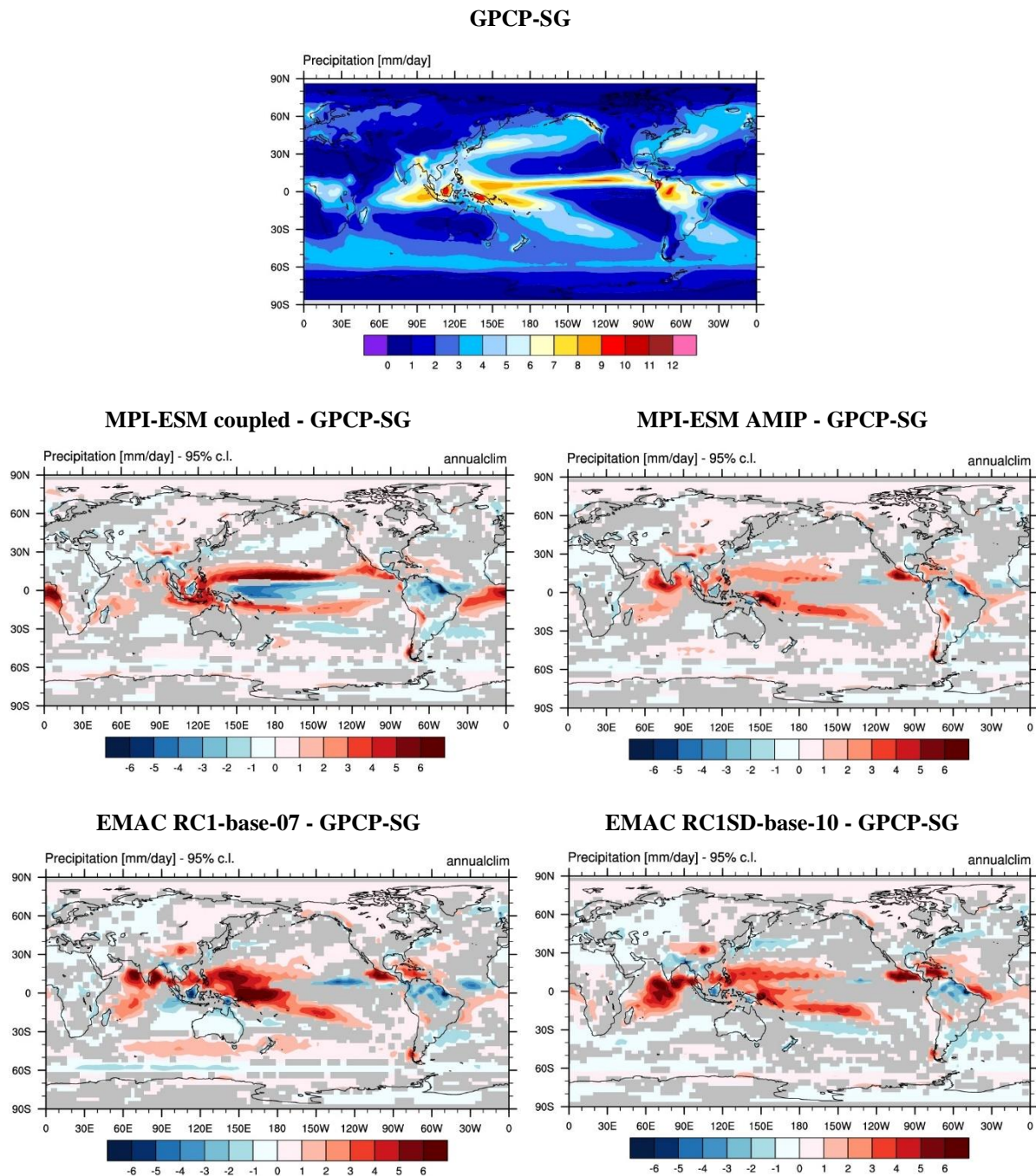


**Figure 5.3:** The 21-yr average precipitation (1984-2005) in mm per day from the GPCP-SG analysis based on satellite observations (top), and the differences between GPCP-SG and each of the four model simulations (middle and bottom). Biases exceeding the 95 % level of statistical significance based on Student's t test are coloured in red and blue.

Regions are coloured in red and blue in which the biases exceeding the 95% level of statistical significance based on Student's t-test. Observations and model simulations are averaged over the period 1984 to 2005. The focus of the evaluation is on the tropics and subtropics over the Pacific Ocean, such as the rain belts in the Pacific ITCZ and South Pacific Convergence Zone (SPCZ). High precipitation rates are also found in the Indian Ocean, Maritime Continent, western equatorial Pacific, and the Atlantic and Indian Ocean ITCZ (Fig. 5.3). The amplitude of the bias in the modelled precipitation is as large as  $6 \text{ mm day}^{-1}$  over a broad region in the tropics, and as much as  $3 \text{ mm day}^{-1}$  in the subtropics. The globally averaged annual mean precipitation is also overestimated with values between  $2.9 \text{ mm day}^{-1}$  and  $3.0 \text{ mm day}^{-1}$  compared with an observed value of  $2.7 \text{ mm day}^{-1}$  (Tab. 5.3). Associated with the SST bias in the so-called cold tongue in the equatorial eastern Pacific (Fig. 5.6 b). The MPI-ESM coupled simulates an unrealistic narrow band of minimum precipitation in this region (Fig. 5.3). This rain belt is a so-called double-ITCZ pattern, which is also characterized by unrealistic, excessive precipitation over the Northern Hemisphere ITCZ and the Southern Hemisphere SPCZ. The double-ITCZ problem is a typically systematic bias in many coupled ocean-atmosphere climate models (Lin 2007; Li and Xie, 2014) Even though the models with prescribed SSTs naturally do not have any biases in SST, these models still show unrealistic excessive precipitation particularly in the western Pacific and the Indian Ocean. In the MPI-ESM AMIP run and the EMAC RC1SD-base-10 simulation, there is a strong overestimation of daily mean precipitation of up to  $6 \text{ mm day}^{-1}$  in these regions. The overestimation in the free-running EMAC RC1-base-07 simulation is significantly stronger with biases exceeding  $6 \text{ mm day}^{-1}$ . This suggests that the overestimation of tropical precipitation might be related to problems in the convection parametrization of the atmospheric parts of models, and that the underestimation of precipitation in the equatorial Pacific in the coupled run of MPI-ESM is related to ocean-atmosphere feedbacks (Lin, 2007). Nevertheless, the spatial correlation coefficients of GPCP-SG (Tab. 5.3) and the MPI-ESM AMIP run (0.87) and the EMAC RC1SD-base-10 simulation (0.83) are considerably higher than those of the free-running EMAC RC1-base-07 (0.79) and the MPI-ESM coupled (0.77) simulations.

**Table 5.3:** Statistics of global average multi-year mean precipitation rates [ $\text{mm day}^{-1}$ ], averaged over the years 1984-2005.

	<b>GPCP-SG</b>	<b>MPI-ESM coupled</b>	<b>MPI-ESM AMIP</b>	<b>EMAC RC1-base-07</b>	<b>EMAC RC1SD-base-10</b>
<b>Annual mean precipitation [<math>\text{mm day}^{-1}</math>]</b>	2.7	2.9	3.0	3.0	3.0
<b>Pattern correlation</b>		0.77	0.87	0.79	0.83
<b>Root-mean-square error (RMSE) [<math>\text{mm day}^{-1}</math>]</b>		1.6	1.1	1.5	1.4

### 5.1.3 Evaluation of Annual Mean Total Cloud Amount

Consistent with the significant biases in precipitation, the models also show large regional biases in the geographical distribution of the mean total cloud amount (TCA) (Fig. 5.4)

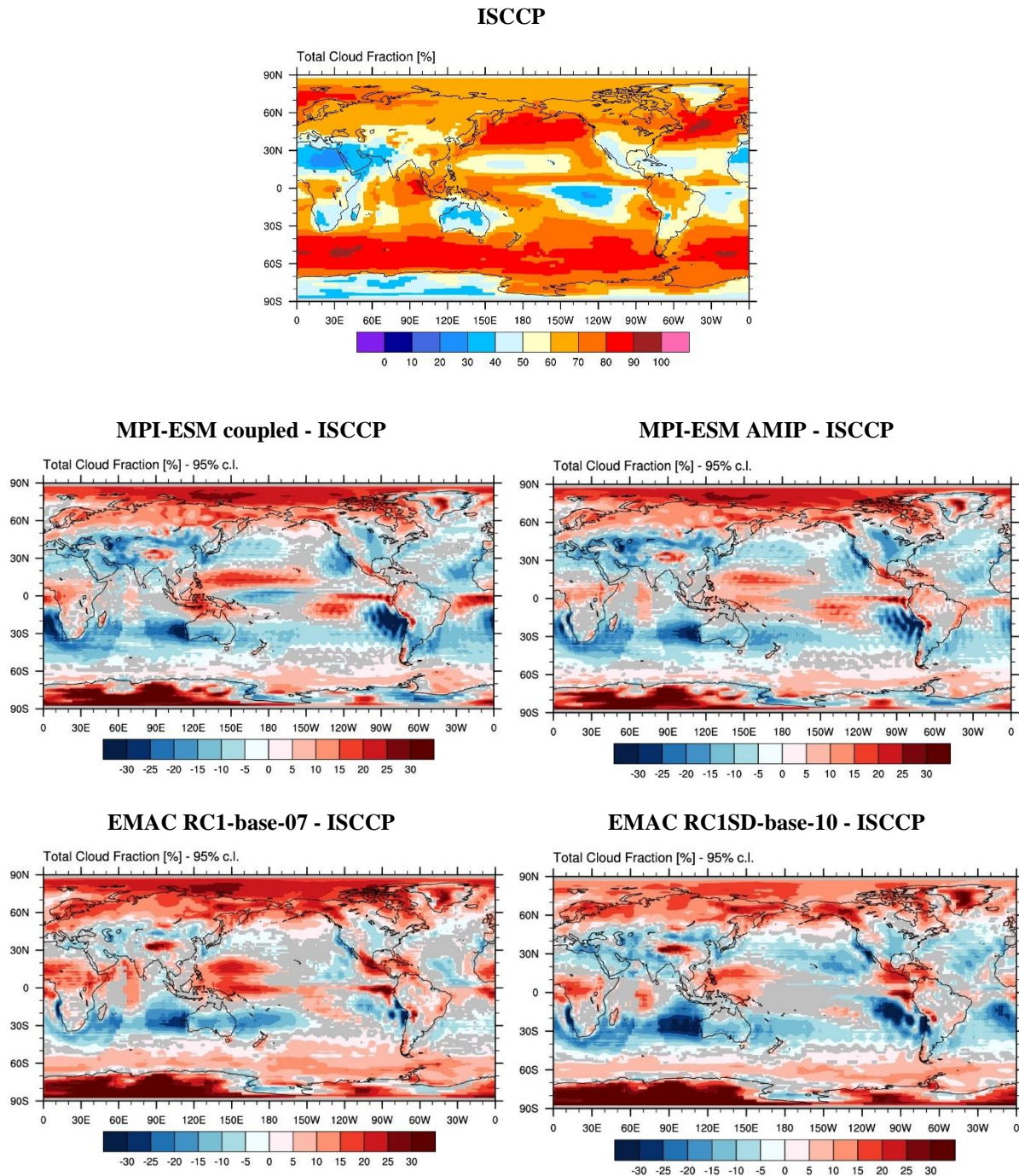


**Figure 5.4:** The 21-yr average total cloud amount (1984-2005) in percent from ISCCP satellite observations (top), and below the differences between ISCCP and each of the model simulations. Biases exceeding the 95 % level of statistical significance based on Student's t test are coloured in red and blue.

As discussed above, biases in the tropical SST cause errors in the precipitation and clouds pattern. The mean total cloud amount from the MPI-ESM coupled simulation also shows an unrealistic double-ITCZ. Compared with ISCCP observations, the models generally underestimate TCA in particular in regions with persistent marine stratocumulus found on the eastern sides of the subtropical ocean basins. Here, the absolute differences in total cloud amount range between -15% and -35%. In contrast, TCA over most of the eastern tropical Pacific as well as large parts of the off the eastern coast of Central America is overestimated (absolute values +15% to +35% larger than in the observations). The global average TCA is overestimated in the models with values ranging between 63% (MPI-ESM coupled) (Fig. 5.4) and 68% (EMAC RC1-base-07) compared to 60% in the observations. The linear pattern correlation of the annual mean TCA between the individual models and the satellite observations is nearly identical with values between 0.76 (coupled simulation of MPI-ESM) to 0.79 (EMAC RCSD1-base-10).

**Table 5.4:** Statistics of the global mean time-averaged total cloud amount [%], averaged over the years 1984-2005.

	<b>ISCCP</b>	<b>MPI-ESM coupled</b>	<b>MPI-ESM AMIP</b>	<b>EMAC RC1- base-07</b>	<b>EMAC RC1SD- base-10</b>
<b>Annual mean total cloud amount [%]</b>	60	63	63	68	64
<b>Pattern correlation</b>		0.76	0.78	0.79	0.79
<b>Root-mean-square error (RMSE) [%]</b>		11.1	10.3	10.7	11.5

### 5.1.4 Evaluation of Annual Mean Liquid Water Path

Figure 5.5 shows the 18-yr annual mean liquid water path averaged over the years 1988 – 2005 from the University of Wisconsin LWP climatology (UWisc) data set, and the differences between models and observations indicating the bias. UWisc is based on satellite observations from the Special Sensor Microwave Imager (SSM/I), the Tropical Rainfall Measuring Mission (TRMM) Microwave Imager (TMI), and the Advanced Microwave Scanning Radiometer for Earth Observing System (EOS) (AMSR-E) (O'Dell et al., 2008). In all regions with available satellite observations, the highest LWP values (110-180 g m<sup>-2</sup>) are found in the Indian Ocean, the ITCZ, and the SPCZ, and the storm track regions in mid-latitudes. The global annual mean LWP from satellite observations is 86 g m<sup>-2</sup> ± 26 g m<sup>-2</sup> (assuming an uncertainty of 30%, O'Dell et al., 2008). The global mean LWP values in the models range from 63 (coupled atmosphere-ocean simulation of MPI-ESM) to 82 g m<sup>-2</sup> (EMAC RC1-base-07). The linear pattern correlation of the annual mean LWP from the individual models with the

satellite observations range from 0.34 (coupled simulation of MPI-ESM) to 0.59 (EMAC RC1-base-07) (Tab. 5.5). Regions are coloured in red and blue in which the biases exceeding the 95% level of statistical significance based on Student's t test.

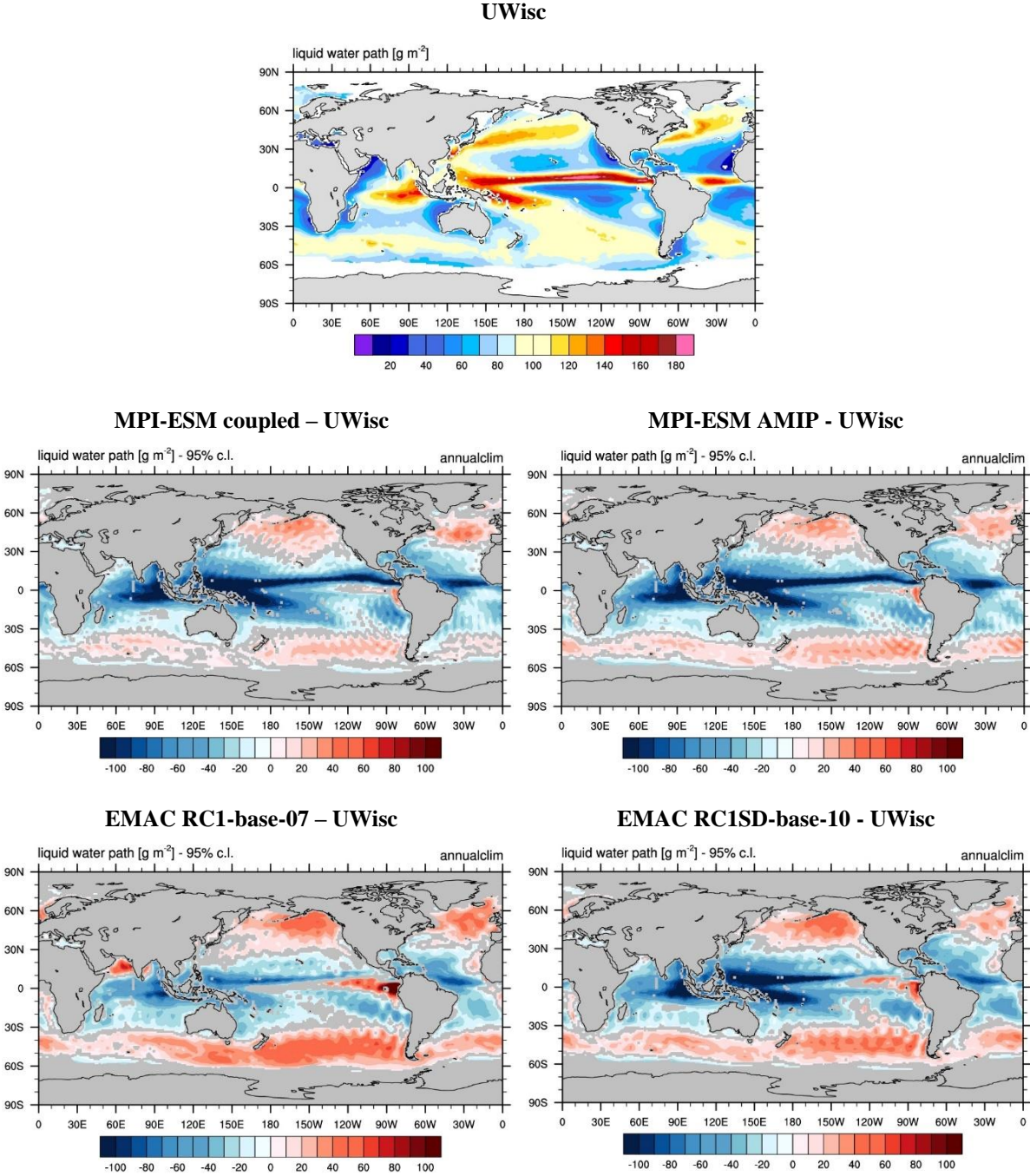


**Figure 5.5:** The 17-yr average cloud liquid water path (1988-2005) in g per m<sup>2</sup> from the UWisc satellite climatology based on SSM/I, TMI, and AMSR-E (O'Dell et al., 2008), and below the differences between UWisc and the MPI-ESM and EMAC simulations. Biases exceeding the 95 % level of statistical significance based on Student's t test are coloured in red and blue.

Overall there is a distinct underestimation in the liquid water path in the tropics with relative biases of about 50% in the MPI-ESM coupled, MPI-ESM AMIP, and EMAC RC1SD-base-10 in the SPCZ. The bias in the model EMAC RC1-base-07 is about 25% in the SPCZ. In contrast, EMAC RC1-base-07 overestimates LWP along the tropical east coast of South America. All four model simulations generally overestimate the liquid water path in mid-latitudes (Fig. 5.5), which is the opposite of what has been found for total cloud amount in these regions (Fig. 5.4). Expressed as a relative fraction of the observed values, the models overestimate LWP in the mid-latitudes storm track regions by about +20% to +30%. In the equatorial eastern Pacific particularly off the coast of South America, the overestimation in LWP is low in the MPI-ESM coupled ( $20 \text{ g m}^{-2}$ ) and high in EMAC RC1-base-07 ( $100 \text{ g m}^{-2}$ ). LWP in the SEP stratocumulus region is underestimated in all four model simulations. Lauer and Hamilton (2013) showed that simulated cloud climatologies (LWP, TCA) show large intermodal discrepancies between many coupled CMIP5 model simulations.

A comparison of the MPI-ESM coupled ocean-atmosphere simulation (MPI-ESM coupled) with the simulation with prescribed SSTs (MPI-ESM AMIP) shows that MPI-ESM AMIP does not outperform MPI-ESM coupled in reproducing observed mean cloud properties. This suggests that the deficiencies in model cloud simulations may be rather attributable to the cloud, convection, and boundary layer parameterization than to biases in simulated SSTs (Lauer and Hamilton, 2013).

**Table 5.5:** Statistics of the global mean time-averaged liquid water path [ $\text{g m}^{-2}$ ] over the ocean, averaged over the years 1988-2005.

	<b>UWisc</b>	<b>MPI-ESM coupled</b>	<b>MPI-ESM AMIP</b>	<b>EMAC RC1-base-07</b>	<b>EMAC RC1SD-base-10</b>
<b>Annual mean liquid water path [<math>\text{g m}^{-2}</math>]</b>	86.7	63.4	64.2	82.2	70.8
<b>Pattern correlation</b>		0.34	0.34	0.59	0.46
<b>Root-mean-square error [<math>\text{g m}^{-2}</math>]</b>		42.8	43.2	32.1	40.0

### 5.1.5 Summary of the Evaluation of the Mean State

For near-surface air temperature, the MPI-ESM coupled, MPI-ESM AMIP, EMAC RC1-base-07, and EMAC RC1SD-base-10 simulations show geographical patterns closely resembling the observed patterns. Significant positive and negative biases are found particularly in mountainous regions. Biases over the ocean are typically smaller than over land areas.

The simulation of clouds and precipitation involves many complex nonlinear processes, and that increases the sensitivity to errors. Deviations from the observations can be quite large in some regions (Dai et al., 2006). The tropical rainfall biases are partly related to errors in simulated SST fields. The cold tongue in the MPI-ESM coupled simulation in the equatorial eastern Pacific extends too far west. Associated with this extended SST cold tongue, an unrealistic narrow band of minimum precipitation and total cloud amount exists over the equatorial central and eastern Pacific, which contribute to the unrealistic double-ITCZ pattern in the model. The analysed models are not capable of reproducing the observed mean total cloud amount well, including marine stratocumulus clouds. The SST and associated precipitation biases over the tropical Pacific likely result from the errors in ocean-atmosphere exchanges of energy and water (e.g., resulting from errors in cloud radiative feedbacks) (Dai et al., 2006). However, the performance of the MPI-ESM coupled simulation and the MPI-ESM AMIP and EMAC simulations (in which the atmospheric components are forced by prescribed SSTs) in reproducing the observed cloud climatologies is quite similar, the atmosphere-only models do not outperform the coupled run in simulating the observed mean cloud properties. For example, the spatial correlation of the simulated annual mean LWP from the coupled and the AMIP MPI-ESM with the UWisc satellite climatology is 0.34 in both cases. A difference in the simulated annual mean LWP can be found between the nudged and the free-running EMAC version. Here, the spatial correlation with the UWisc climatology of the free-running version is 0.59 compared to 0.46 of the nudged simulation. Nevertheless, both the EMAC and MPI-ESM model overestimate LWP in mid-latitudes and underestimate LWP in the tropics.

As a conclusion the biases in the simulated cloud properties and precipitation climatologies may be partially attributable to the cloud, convection, and boundary layer parameterizations. The interactions of the atmosphere with the ocean may not be the particular reason for these biases in precipitation and cloud properties.

## 5.2 Natural Modes of Climate Variability

Internally-generated modes of variability complicate model evaluation and intercomparison as they introduce noise to the system. As the modes investigated here (ENSO, PDO) are spontaneously generated by the models with free-running ocean, they do not necessarily exhibit the same chronological sequence in the models as in nature. However, their statistical properties (i.e., time scale, autocorrelation, spectral characteristics, and spatial patterns) should be captured by climate models. Here, the skill of the MPI-ESM coupled simulation in reproducing the observed tropical Pacific mean state in SST, the PDO and the seasonal evolution of ENSO is analysed and evaluated. In order to investigate the atmospheric cloud properties and precipitation response to the SST evolution in the ENSO composites (temporal evolution of the El Niño minus La Niña composites), all four model simulations including the ones with prescribed observed SSTs (MPI-ESM AMIP, free-running EMAC RC1-base-07, and nudged EMAC RC1SD-base-10) and the MPI-ESM coupled were analysed globally and on regional scales. Finally, the systematic differences are assessed between the coupled ocean-atmosphere version and the atmosphere-only configuration (AMIP) of MPI-ESM using prescribed SSTs and between the nudged simulation of EMAC perform and the free-running version.

### 5.2.1 Geographical Pattern of Non-Seasonal Sea Surface Temperature Variability

Before evaluating and analysing the temporal and spatial variability of the climate modes PDO and ENSO and their impact on cloud properties and precipitation, the performance of the MPI-ESM coupled simulation is assessed. Such knowledge on the models' skill in realistically representing the SST is needed to evaluate, assess and interpret the simulation results later. Errors in the simulation of ENSO or PDO are often closely related to errors in the mean state of SST (AchutaRao and Sperber, 2006; Wittenberg et al., 2006; Guilyardi, 2006) and degrade the quality of the simulation in capturing the hydrological response (Joseph and Nigam, 2006). The long-term mean observational SST distribution is shown in figure 5.6 (a) and additionally the difference between the observations and simulated mean SST distribution from the MPI-ESM coupled simulation (see Figure 5.6 b). The model produces an overly narrow SST cold tongue in the central equatorial Pacific that extends far west into the western Pacific, which is a widespread bias in many coupled ocean-atmosphere models (IPCC WR5 2013). Lin (2007) attributes these errors to overly strong wind speed and sensitivity of SST to rain. Li and Xie (2014) suggest that the errors arise from the atmospheric interaction with the ocean via Bjerknes feedback (see Section 2.1.1.1). A warm SST bias in the coastal upwelling region off the coast of Peru is often associated with too few stratocumulus clouds (Li and Xie, 2014; Ma et al., 1996).

One approach to quantify the magnitude and spatial distribution of non-seasonal SST variability is to map the standard deviation of the monthly SST anomalies (defined as the deviation of the SST for a particular month from the long-term monthly mean).

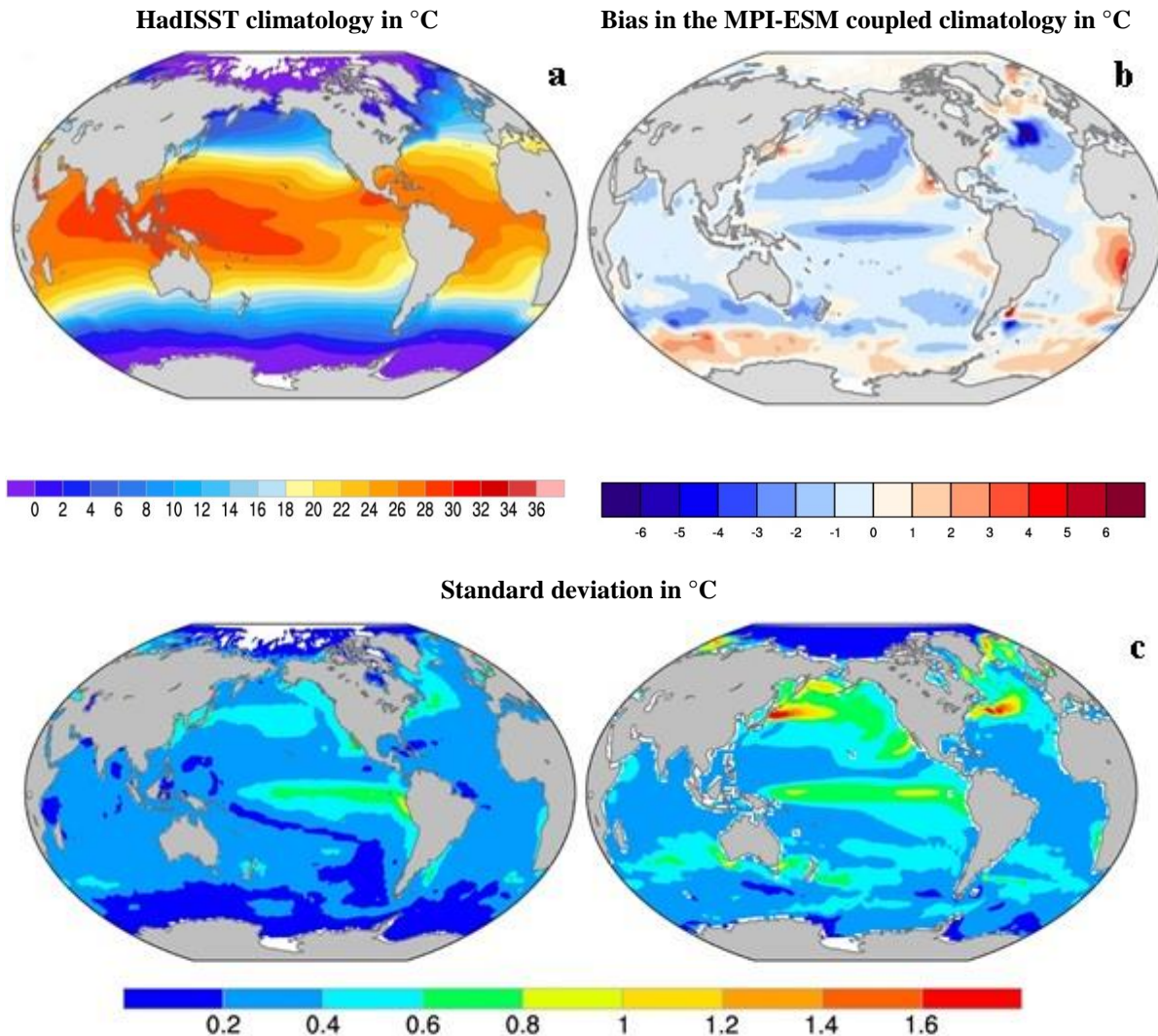


**Figure 5.6:** (a) The 136-yr average sea surface temperature (1870-2005) in °C from the HadISST reference data set (top left), and (b) the difference between the HadISST data and the MPI-ESM coupled for the same time period. (c) The standard deviation (bottom) of monthly SST anomalies (deviations from the long-term monthly means) based on HadISST (left) and the MPI-ESM coupled (right). The units are °C.

Figure 5.6 (c) shows the standard deviation based on the values of HadISST data and the coupled simulation from MPI-ESM for 1870 – 2005. In the observed pattern, two regions stand out as having the largest non-seasonal variability: the upwelling zones in the equatorial Pacific off the coast of Peru, the western-boundary current regions (Kuroshio and Gulf Stream). In these regions maximum values of the SST variability given by the standard deviation exceed 0.6°C. The MPI-ESM coupled overestimates the standard deviation of the SST in the Pacific upwelling regions. In the tropics, the

highest standard deviations are found in the equatorial Pacific and coastal upwelling in the eastern Pacific basin. In this region, large SST changes occur during an ENSO event. Apart from the regions of maximum SST standard deviation, there is a high variability (standard deviations around 0.75 – 1°C) in some regions of the North Pacific, North Atlantic and South Pacific, South Indian, and South Atlantic and relatively low variability across the tropical ocean basins (standard deviations around 0.3 – 0.5°C).

## 5.2.2 Pacific Decadal Oscillation (PDO)

The standard deviation map of non-seasonal SST anomalies presented in Figure 5.6 (c) does not give any information on how SST variations at one location are related to another. To investigate the co-variability (spatial variability) of SST anomalies at different locations, alternative analysis methods are needed (Deser et al., 2010). One commonly used approach is the empirical orthogonal function (EOF) analysis (see Section 2.2.1) and extensions thereof (von Storch and Zwiers, 1999). The leading EOF of monthly area-weighted SST anomalies averaged over the North Pacific (20°-70°N, 110°E-100°W) is calculated. The global monthly average SST anomalies are subtracted from each time step to separate the PDO from any “global warming” signal contained in the data. In general, EOFs consists of a spatial pattern and a corresponding time series (so-called principal component (PC)). The associated first PC time series is termed the Pacific PDO after Mantua et al. (1997) (Fig. 5.7 a). Although the EOF calculation is limited to the North Pacific, the pattern is displayed globally by regressing the PC time series on the monthly SST anomalies at each grid cell.

The PDO pattern in the North Pacific (Fig. 5.7 a) consists of a tongue-shaped region around 35°N extending from Japan eastwards to about 140°W where the SSTs are either anomalously warm or cold, depending on the phase of the PDO, and a horseshoe shaped region along the west coast of North America where SST anomalies are of the opposite sign than in the tongue-shaped region. The MPI-ESM coupled has difficulties in simulating a recognizable PDO pattern. In part, both the shape and the strength of the PDO pattern differ significantly from that obtained from the HadISST data. In the model, only 16.1% of the total variability of the SST in this region are explained by the leading EOF, whereas this mode accounts for 25.2% of the variance in the HadISST observational data set (Rayner et al., 2003). Compared to the pattern correlation of the multi-model mean (MMM) (correlation coefficient of 0.80) obtained from averaging over 33 CMIP5 models, the performance of the MPI-ESM coupled in reproducing the first EOF pattern (see Fig. 5.8 and 5.9) is somewhat below average (0.69). The second EOF calculated from the MPI-ESM results accounts for 9.9% of the total variability, which is slightly lower than that from the observations (11.2%) and the CMIP5 MMM (11.3%).

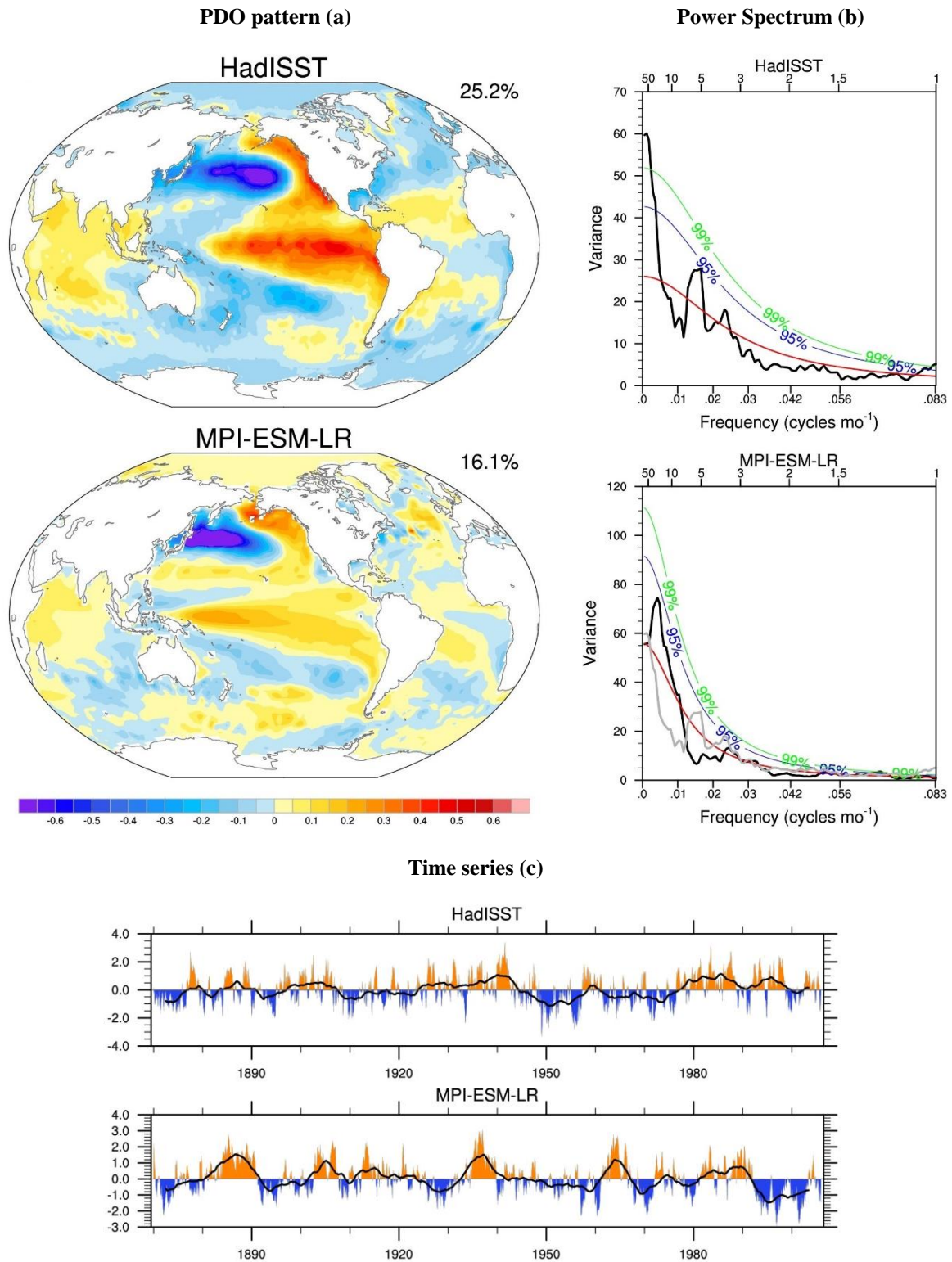


**Figure 5.7:** A sample of the ESMValTool-CVDP diagnostics package showing the PDO for one observational data set (HadISST) and MPI-ESM coupled from 1870 - 2005. (a) The spatial pattern shows the global SST anomalies in °C associated with the first EOF (= PDO). The name of each data set, period of analysis, and percent of the variance explained by the first EOF are given above each plot. (b) The power spectrum as a function of frequency in cycles per month with the solid black line denoting the spectrum. The red line indicates the best-fit first-order Markov red noise spectrum, the red line the 95% and the green line the 99% confidence intervals. The observational spectrum is overlaid in grey. (c) Associated PC time series showing the unsmoothed record (red and blue bars) and the 10-year low-pass-filtered data (black line).

The simulated strongly negative SST anomaly in the MPI-ESM coupled is about 30° further to the west and closer to Japan, compared to the observations. The region with strongly positive SST anomalies off the western coast of North America with values of 0.4 to 0.6 °C in the observations is significantly weaker in the MPI-ESM coupled simulation (0.2 to 0.3 °C).

The difficulties of the MPI-ESM coupled simulation in reproducing the observed PDO pattern could be related to the long periods of warm and cold PDO events and the lack of knowledge about the mechanism. An inability to correctly reproduce the observed PDO pattern is expected to affect the model's ability to simulate the relatively slow variations in climate associated with this pattern (Stoner et al., 2009).

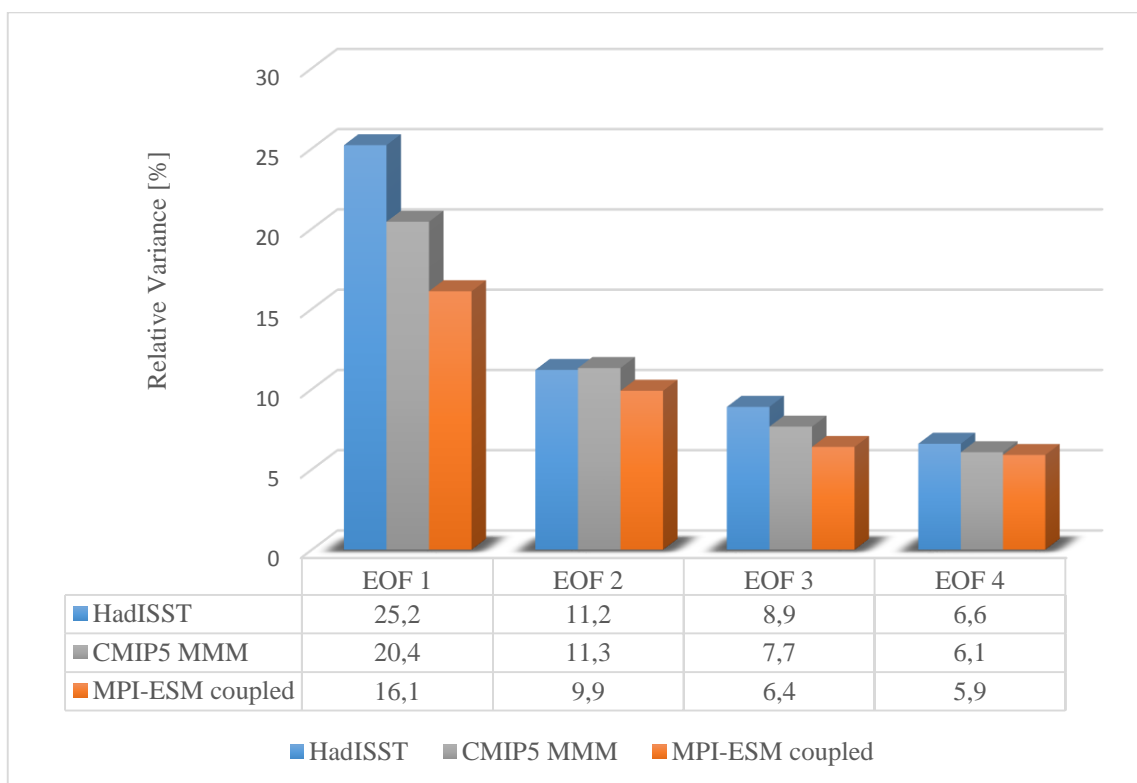


**Figure 5.8:** Relative variance explained by the first four EOFs in the PDO region (20°-70°N, 110°E-100°W) from the multi-model mean (MMM) averaged over 33 CMIP5 models, the MPI-ESM coupled and the HadISST observations in the years 1870 - 2005.

The time series of the PDO (Fig. 5.7 c) exhibits considerable decadal variability and shows periods during which its phase is the same for two decades or longer. This is in agreement with the results from Deser et al. (2010). The PDO is spontaneously generated by the model and thus does not exhibit the same chronological sequence as in nature. The time of specific events as well as the strength and the typically decadal duration of a PDO event differ significantly between a coupled model such as the MPI-ESM and the HadISST data. In order to investigate the temporal variability of the leading SST anomaly EOF, a spectral analysis is calculated (Fig. 5.7 b). The values represented in the power

spectra plots are the percentage of the total variance explained at that frequency. The power spectrum as a function of frequency in cycles of the PDO per month, the solid black line denotes the spectrum. The red line indicates the best-fit first-order Markov red noise spectrum, the red line its 95% and the green line its 99% confidence intervals. The observational spectrum is overlaid in grey. The power spectrum of observational data shows that the PDO has a significant peak at 30-50 years. Throughout the record there is also a significant power in the 3 to 7 year band typical for ENSO. In both the power spectrum and the time series this period can be clearly seen. The spectral analysis of the model also illustrates a weak ENSO peak between 3 to 5 years. The simulated peak associated with the PDO signal has a frequency of around 20 years.

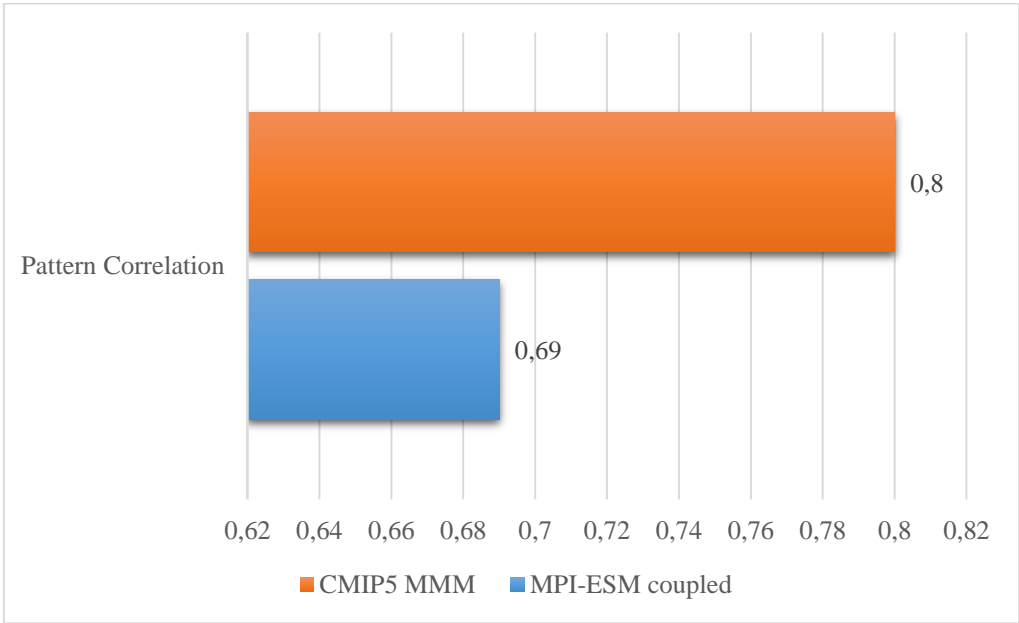


**Figure 5.9:** Pattern correlation in the PDO region (20°-70°N, 110°E-100°W) between the multi-model mean (MMM) averaged over 33 CMIP5 models and the MPI-ESM coupled with the HadISST observations in the years 1870 - 2005.

## 5.2.3 El Niño-Southern Oscillation (ENSO)

### 5.2.3.1 Niño-3.4 SST Variability

A first step for representing and assessing the SST variability in the tropical Pacific is the comparison of the area-weighted average of monthly SST anomalies in the region 5°N-5°S and 120°-170°W between the coupled model and the observation. The so-called “Niño-3.4 index” (see e.g., Trenberth et al., 1997) includes the region in the western half of the equatorial cold tongue region, that provides a good measure of important changes in SST and SST gradients that result in changes in the pattern of deep tropical convection and atmospheric circulation. Figure 5.10 (a) displays the time evolution of the Niño-3.4 SST index calculated from the HadISST observations and the coupled simulation with MPI-ESM for the years 1870-2005. Both Niño-3.4 time series have been detrended by subtracting the least square linear trend from the data. The ENSO evolution is quite “irregular” in the model, as in the observational time series, so that the ENSO can be adequately described as a series of events rather than a regular oscillation. The MPI-ESM coupled shows some degree of asymmetry between the positive and negative events. Observations show that El Niño events tend to be stronger in terms of SST anomalies than La Niña events which is also reproduced by the model. This suggests that the MPI-ESM model may capture some of the observed ENSO nonlinearities – even though it remains a challenge in many models (Dommenget et al., 2013; Zhang and Sun, 2014). Due to the free-running ocean in the coupled MPI-ESM, the model is not meant to reproduce the exact evolution of the observed Niño-3.4 SST time series. Therefore, the focus of this analysis is on the statistical properties rather than on individual events. In addition to the Niño-3.4 SST time series, spectral analysis is used to investigate the temporal variability of the leading SST anomaly (Fig. 5.10 b). The power spectrum is displayed as a function of frequency in cycles per month of the detrended Niño-3.4 SST index, the solid black line denotes the spectrum. The red line indicates the best-fit first-order Markov red noise spectrum, the red line its 95% and the green line its 99% confidence intervals. The observational spectrum is overlaid in grey on the model spectrum. As can be seen from the figure, the HadISST spectra show a maximum power for periods of around 2.5 to 7 years (which indicates the average period of ENSO in the real world). The simulated power spectrum shows prominent peaks between 2.5 – 6 years, furthermore illustrates that the corresponding modelled spectral peak is shifted towards longer periods (~ 12 years).

### Nino-3.4 time series

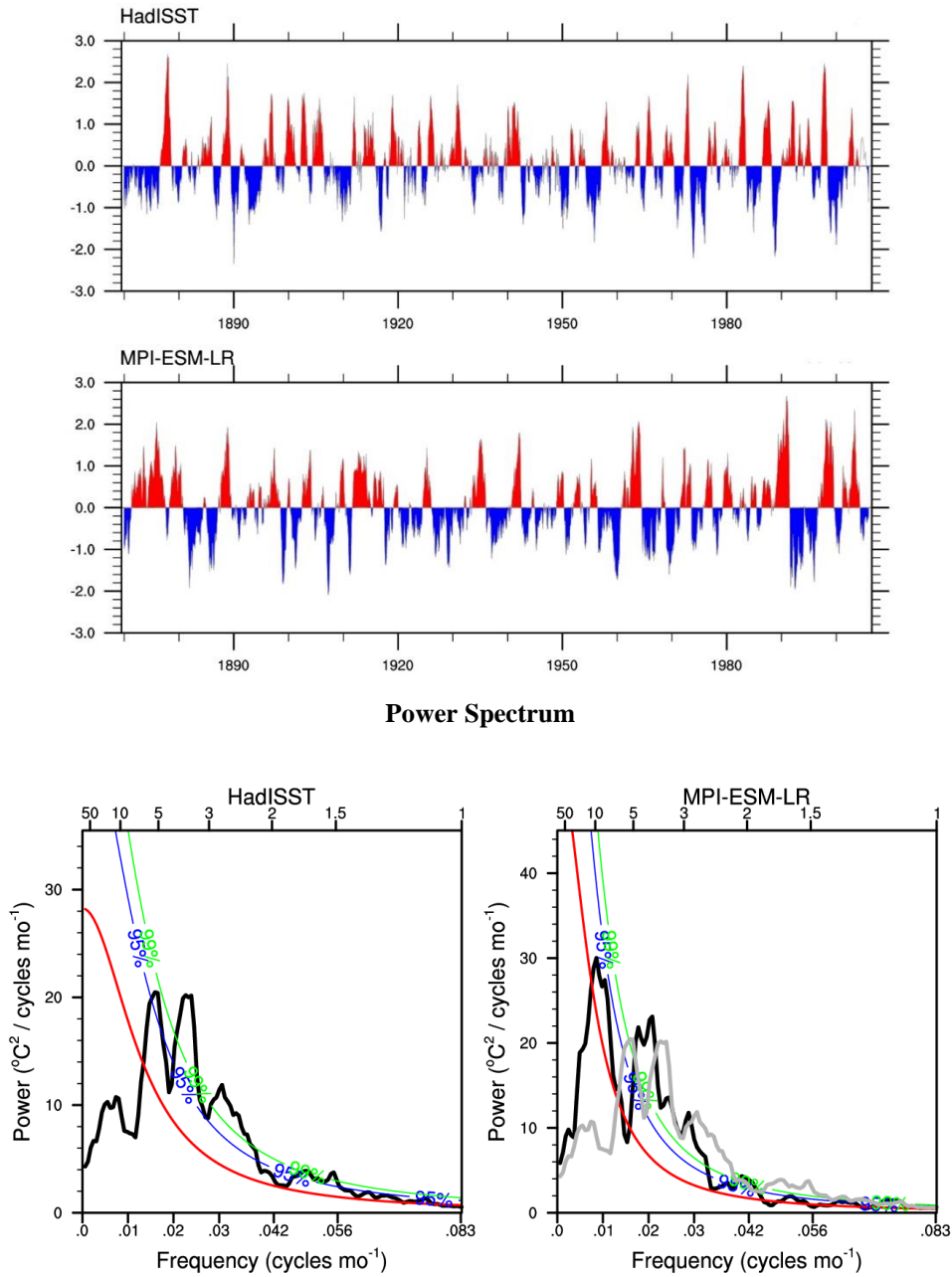


**Figure 5.10:** (a) Temporal evolution of the Nino-3.4 SST index (area-weighted monthly SST anomalies averaged over the region 5°S-5°N, 120°-170°W) over the period 1870 – 2005 from the HadISST data set (top panel) and the coupled (“historical”) experiment with MPI-ESM-LR. The red/blue shading of the detrended time series denotes the positive/negative deviations from the long-term mean. Vertical axis units are °C. (b) The power spectrum as a function of frequency in cycles per month of the Nino-3.4 SST index, the solid black line denotes the spectrum. The red line indicates the best-fit first-order Markov red noise spectrum, the red line its 95% and the green line its 99% confidence intervals. The observational spectrum is overlaid in grey.

The ENSO variability is typically characterized by a strong phase locking to the seasonal SST cycle, as can be seen by the seasonal cycle of the standard deviation of the Niño-3.4 SST anomaly with warm and cold events peaking in the end of the calendar year. The standard deviation of the observed Niño-3.4 SST index shows a maximum (0.95°C) in December and reaches a minimum (0.55°C) in June

(Fig. 5.11). The standard deviation of the simulated Niño-3.4 SST does not reproduce this seasonal cycle even though the maximum values are also found in December (0.85°C) and January (0.90°C). The lowest value is found in August amounting 0.70°C. The RMSE of the modelled seasonal cycle compared to the observations is 0.22 °C.

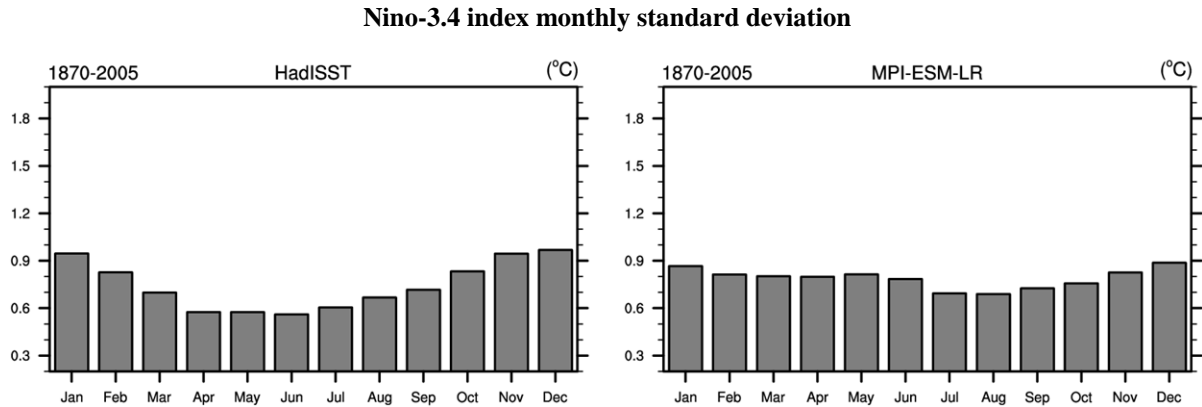


**Figure 5.11:** Monthly standard deviation (°C) of the Niño-3.4 SST index from detrended observations (HadISST) and the MPI-ESM coupled simulation for the 1870 – 2005 mean.

### 5.2.3.2 Composite El Niño and La Niña Events

Based on the Niño-3.4 SST indexes of the model and the observation, a composite of El Niño (La Niña) events along the equator (3°N-3°S) is constructed by selecting years in which the December Niño-3.4 SST index exceeds 1 (is less than -1) standard deviation. To reduce the month-to-month noise, the Niño-3.4 record is smoothed with a 3-point binomial filter before selecting the events. With this criterion, the observed composites for the period 1870 - 2005 are an average of 23 El Niño (EN) events and 20 La Niña (LN) events. The simulated composites are based on 18 (17) EN (LN) events from the coupled simulation with MPI-ESM (see Fig. 5.12). The year that includes the highest Niño-3.4 SST index in December is called year 0 (“Dec<sup>0</sup>”), and the subsequent years are labelled +1 and +2, respectively. The longitude-time sections (Hovmöller diagrams) of composite SST anomalies in Fig. 5.12 are shown for (top) El Niño and (bottom) La Niña based on (left) observations (detrended HadISST) and (right) the model (detrended MPI-ESM coupled simulation). The model composites have been scaled to match the observed composite amplitude of the Niño-3.4 SST index in Dec<sup>0</sup>. The number in the top right of each composite panel indicates the number of events averaged. The warm and cold events from the MPI-ESM simulation (Fig. 5.12) nearly mirror images of another, but only weakly resemble the observed different duration between El Niño and La Niña (“asymmetry”) (Okumura and Deser 2010). The missing asymmetry also occurs in others CMIP5 models (Zhang and Sun, 2014). In particular, the simulated El Niño shows an extended duration through May<sup>+2</sup>, more than 17 months following the peak of the event in Dec<sup>0</sup> and almost one year longer than in the observations.

Another notable difference is that the eastern equatorial Pacific SST anomalies extend approximately 20°-30° of longitude farther west during El Niño compared to the observations.

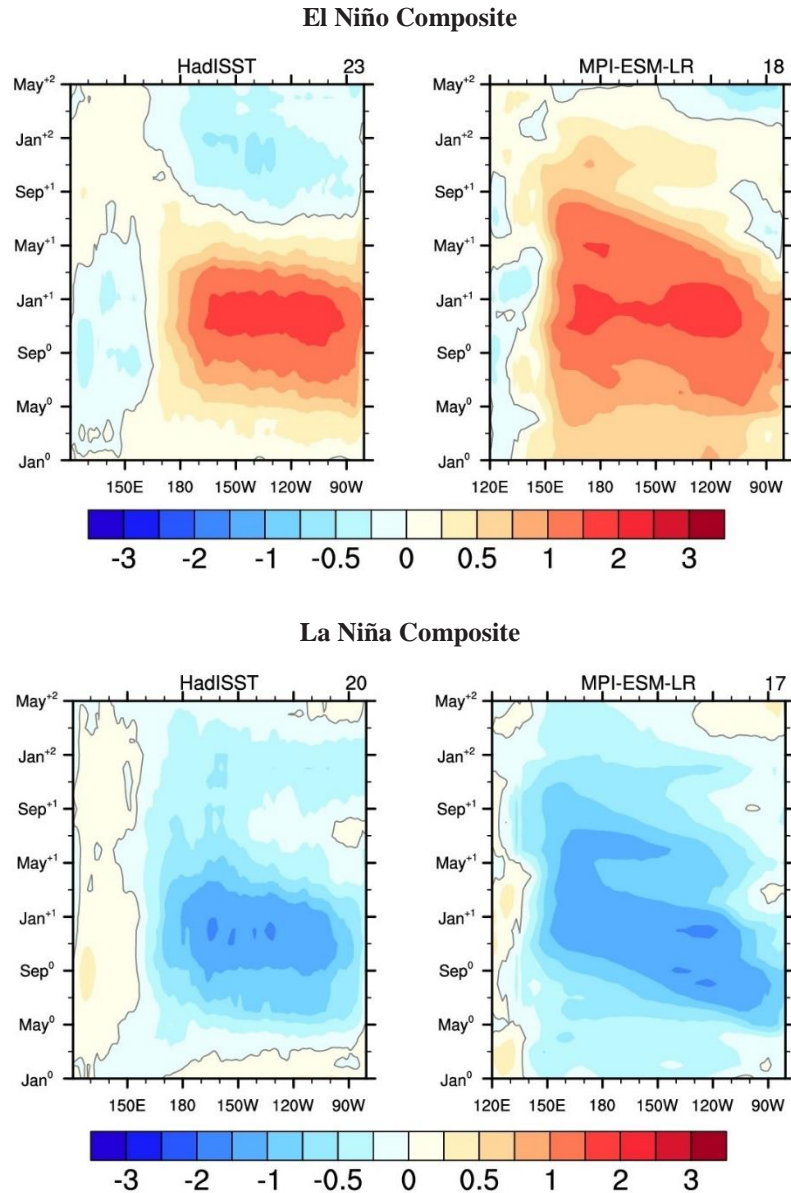


**Figure 5.12:** Longitude-time sections of composite ENSO events along the equator ( $3^{\circ}\text{N}$ - $3^{\circ}\text{S}$ ) for (top) El Niño and (bottom) La Niña conditions based on (left) observations (detrended HadISST data set) and (right) calculated by the coupled CMIP5 model MPI-ESM. The model composites have been scaled to match the observed amplitudes of the Niño-3.4 SST index in Dec<sup>0</sup>. The number in the top right of each panel indicates the number of events averaged.

The temporal evolution of the difference between the composite El Niño and the composite La Niña is shown for each season in figure 5.13, starting with the conditions during June – August<sup>0</sup> (JJA<sup>0</sup>) before the peak and termination with conditions in March – May<sup>+1</sup> (MAM<sup>+1</sup>) of the following year. The warm event (El Niño) composite is based on a selection of the years for which the Niño-3.4 SST index in

November – January exceeds +1 standard deviation based on the period 1984 – 2005. Similarly, the cold event (La Niña) composite is based on a selection of the years for which the November – January Niño-3.4 SST index is less than -1 standard deviation. The observed composite ENSO evolution is depicted for linearly detrended sea surface temperatures (SSTs) and resulting response of near-surface air temperatures over land (TAS), sea level pressure (SLP) (left panel), and precipitation (PR) (Figure 5.13), and total cloud amount (TCA) (left panel) and liquid water path (LWP) (right panel) (Figure 5.14). In the ENSO composites, the La Niña composites are subtracted from the El Niño composites to illustrate the differences between warm (El Niño) and cold (La Niña) ENSO events in the above mentioned variables.

The seasonal SST evolution of the ENSO composite from the coupled model is similar to that obtained from the observations (Fig. 5.13): it exhibits a strengthened warming of the SST along the equator and the coast of South America during JJA<sup>0</sup> that subsequently grows in amplitude over the next several months, reaching its peak around December - Februar<sup>+1</sup> (DJF<sup>+1</sup>). The warm anomaly diminishes during March - May<sup>+1</sup> and begins to turn into a weak cold anomaly in JJA<sup>+1</sup> (not shown). Accompanying the warming in the equatorial central Pacific is the simultaneous development of negative SST anomalies in the northwest and southwest tropical Pacific. Many coupled atmosphere-ocean global climate models like MPI-ESM (Fig. 5.15) simulate the centre of the ENSO-related SST variability over the shifted to the west compared to the observed location (Stoner et al. 2009; Capotondi and Wittenberg, 2013). Furthermore, the simulated region with positive anomalies (coupled MPI-ESM) extends too far into the western Pacific, where a negative SST anomaly is found in the observations during El Niño (Giorgetta et al. 2013).

In order to investigate and assess the atmospheric response to the SST evolution in the ENSO composites (Fig. 5.15), all four model simulations including the ones with prescribed SSTs (MPI-ESM AMIP (Fig. 5.16), EMAC RC1-base-07 (Fig. 5.17), and EMAC RC1SD-base-10 (Fig. 5.18)) were analysed during the peak months of El Niño or La Niña (DJF<sup>+1</sup>). The model simulations with prescribed SSTs naturally include the observed seasonal ENSO SST evolution, whereas the global teleconnections of ENSO with remote regions depend on the atmospheric component of the models.

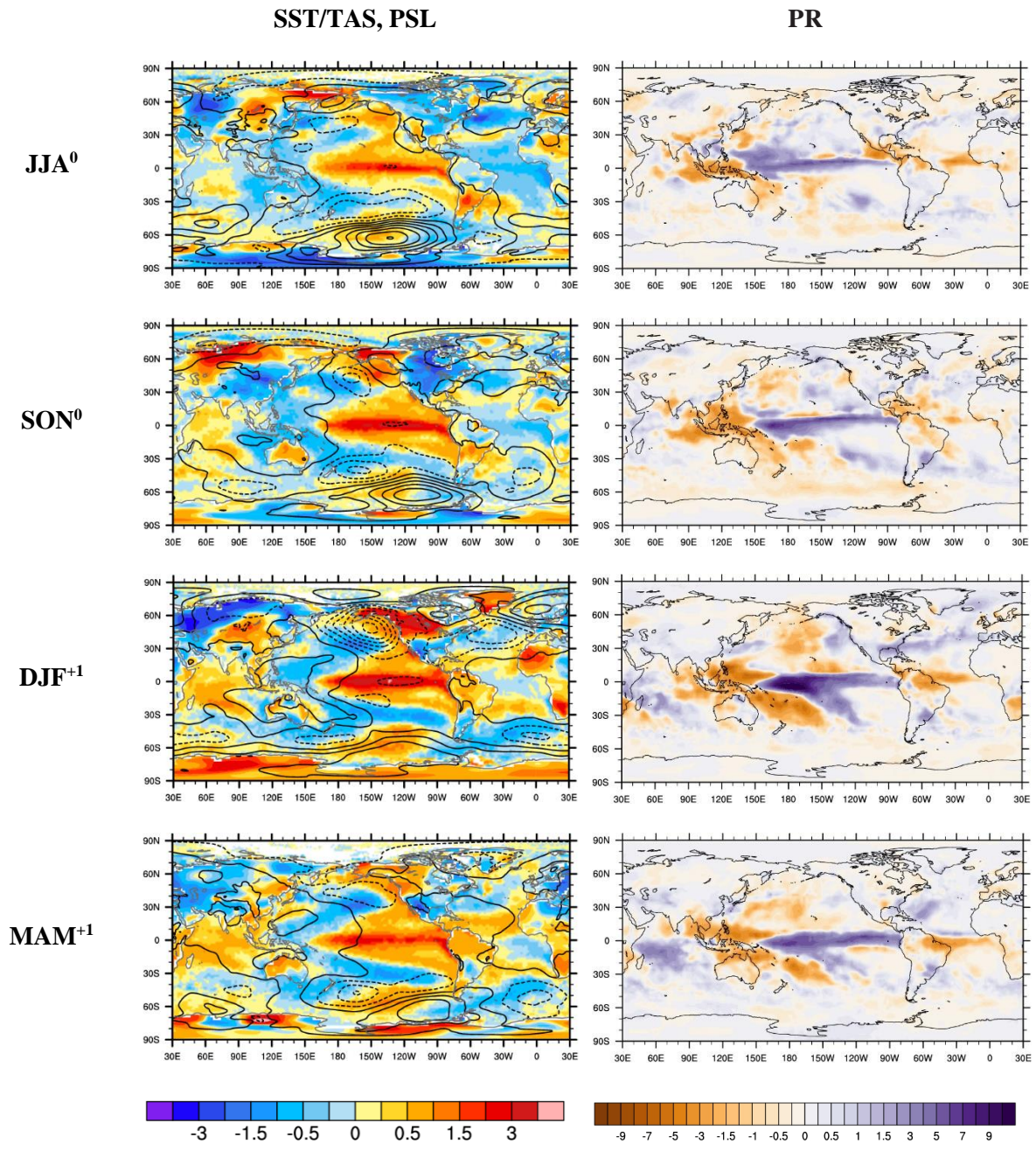


**Figure 5.13:** (left) Temporal evolution of the El Niño minus La Niña composites from observations/reanalysis data for SST and near-surface air temperature over land ( $^{\circ}\text{C}$ ; shaded) and sea level pressure (contour intervals 2 hPa, solid lines show positive values, dashed lines negative values). (right) Difference in precipitation ( $\text{mm day}^{-1}$ ; shaded). (top to bottom) JJA<sup>0</sup>, SON<sup>0</sup>, DJF<sup>+1</sup> and MAM<sup>+1</sup> based on observations for the period 1984 – 2005.

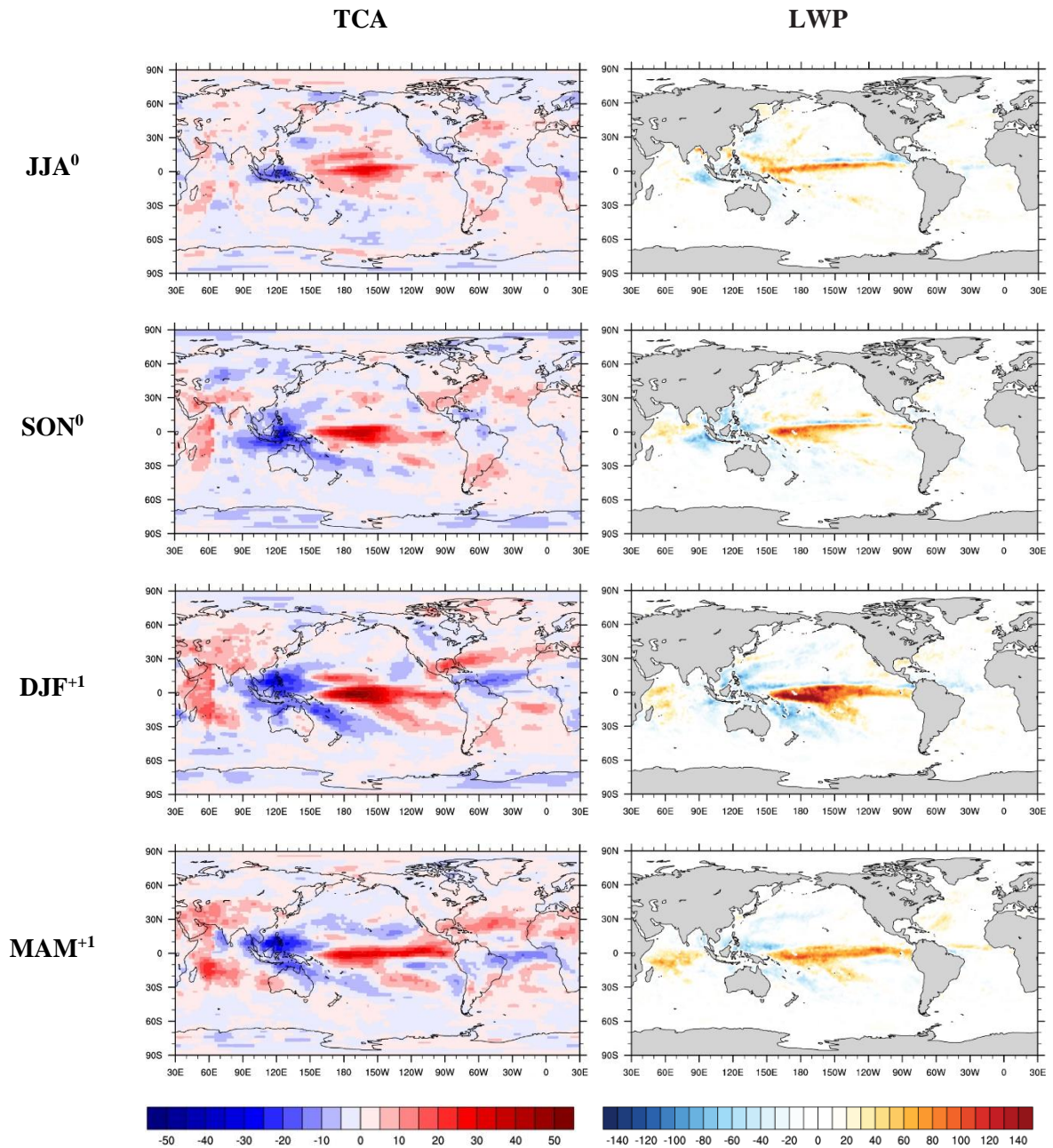


**Figure 5.14:** Temporal evolution of the El Niño minus La Niña composites from observations of (left) TCA (%) shaded and (right) LWP ( $\text{g m}^{-2}$ ; shaded) for (top to bottom) JJA<sup>0</sup>, SON<sup>0</sup>, DJF<sup>+1</sup> and MAM<sup>+1</sup> based on TCA observations for the period 1984 – 2005, and LWP observations for the years 1988 – 2005.

### 5.2.3.3 Global Teleconnections

Here, the ENSO-related atmospheric response to the SST evolution is explained with the help of the observations. Additionally, the model's fidelity is assessed in simulating the response of sea level pressure, precipitation, and cloud parameters to ENSO.

#### ENSO-related Sea Level Pressure Anomalies

In JJA<sup>0</sup> in the ENSO composites (El Niño minus La Niña composites), the SLP response is found over the South Pacific (30° - 80°S, 150°E – 90°W) with a meridional dipole shape, with positive (negative) anomalies near Antarctica and negative (positive) anomalies during El Niño (La Niña) to the north, stretching from New Zealand to South America (Fig. 5.13) (Deser et al., 2012). The geographical pattern and the amplitude of the SLP anomalies from MPI-ESM AMIP and the nudged EMAC RC1SD-base-10 simulation are in good agreement with the observations (not shown). This SLP anomaly pattern persists during SON<sup>0</sup> as El Niño (La Niña) continues to build up. However, the pattern of the simulated SLP response in the models is more meridionally orientated compared to the observations. In DJF<sup>+1</sup>, the strongest SLP response occurs in the Northern Hemisphere, with negative anomalies over the mid-latitude North Pacific (strengthening (weakening) of the Aleutian Low during El Niño (La Niña)). The simulated SLP teleconnection to ENSO is more zonally orientated and spatially more extensive in the Northern Pacific in than observed DJF<sup>+1</sup>. With the exception of EMAC RC1SD-base-10, the model simulations show an unrealistic deepening of the Aleutian low pressure system persisting through MAM<sup>+1</sup> (not shown).

This behaviour is similar to the one reported for the Hadley Centre Atmospheric Model version 3 (HadAM3) by Spencer and Slingo (2003) and the NCAR Community Climate System Model version 4 (CCSM4) (Deser et al., 2012). Overall, the SLP distribution in the Southern Hemisphere shows less seasonal dependence on the ENSO state than that in the Northern Hemisphere. This finding is consistent with Jin and Kirtman (2009) among others. The tropical SLP anomalies correlate with the SST anomalies in the Niño 3.4 region, reaching the maximum amplitude in DJF<sup>+1</sup>. This large-scale SLP anomaly pattern, with the positive values to the west and negative values to the east, is associated with the negative phase of the Southern Oscillation (see also Deser and Wallace, 1999; Harrison and Larkin, 1996).

But not every ENSO event follows the canonical evolution illustrated in Figure 5.13. For example, some events develop mainly in the central equatorial Pacific while others are confined to the coast of South America (Deser and Wallace, 1987; Kao and Yu, 2009). In addition, some events show an eastward movement of the equatorial Pacific SST anomalies (Guan and Nigam, 2008, Deser et al. 2010) in contrast to the westward development of the composite ENSO. As a result, SLP anomalies associated with a particular ENSO event can be quite different. This leads for example to a

displacement of the anomalous convective area during El Niño (La Niña) and is related to a weakening (strengthening) of the Aleutian Low (Zubiaurre and Calvo Fernández 2012).

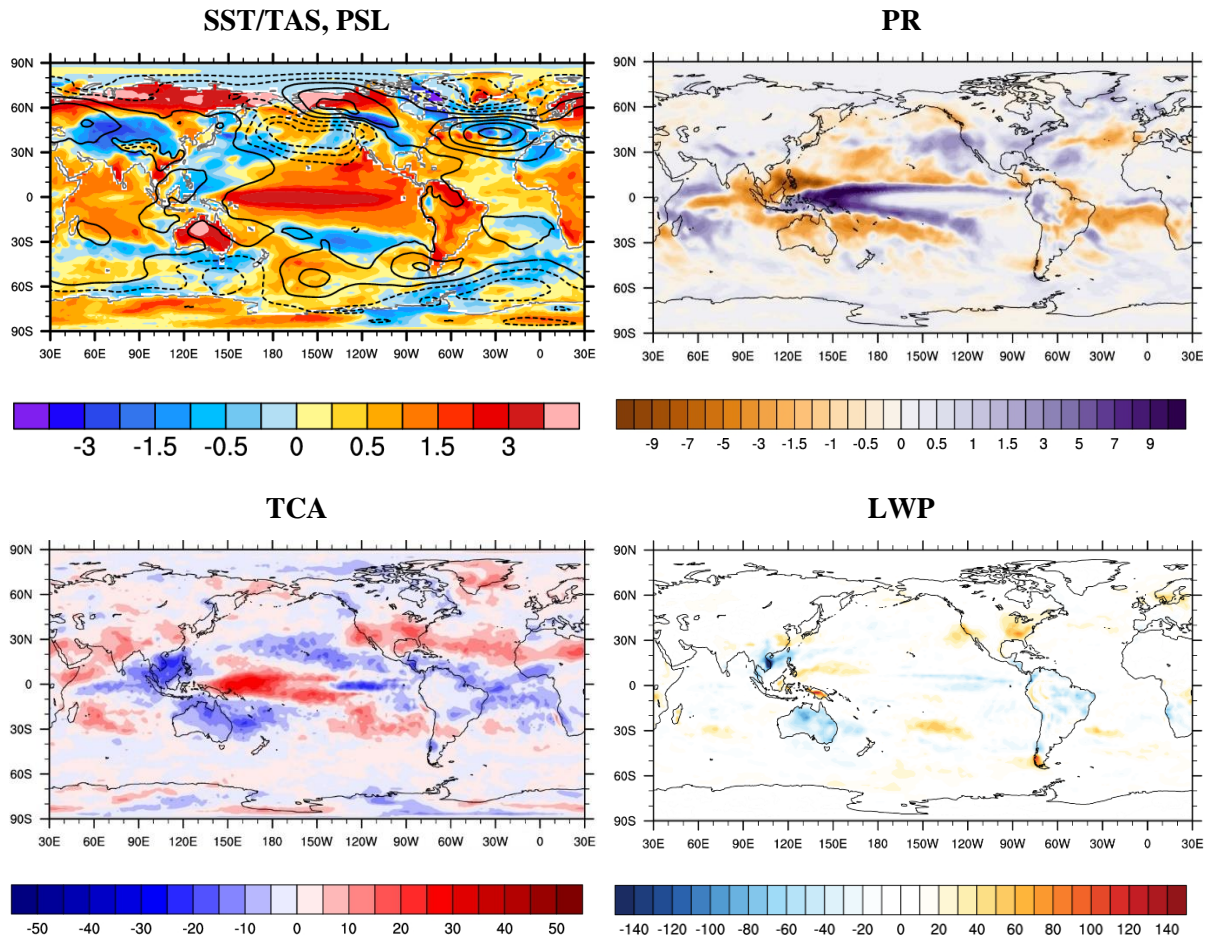


**Figure 5.15:** Evolution of the simulated El Niño minus La Niña composite from the MPI-ESM coupled simulation of (top left) SST/near-surface air temperature over land ( $^{\circ}\text{C}$ ; shaded) and PSL (contour interval 2 hPa, solid lines show positive values, dashed lines negative values), (bottom left) TCA (%; shaded), (top right) precipitation ( $\text{mm day}^{-1}$ ; shaded), and LWP ( $\text{g m}^{-2}$ ) during the ENSO peak in DJF<sup>+1</sup> for the period 1984 – 2005, the simulated LWP for the years 1988-2005.

### ENSO-related Precipitation Anomalies

The spatial precipitation anomalies as a response to ENSO in DJF<sup>+1</sup> given by the differences between the composite El Niño and the composite La Niña are generally quite well simulated by the models (coupled MPI-ESM (Fig. 5.15), MPI-ESM AMIP (Fig. 5.16), EMAC RC1-base-07 (Fig. 5.17), EMAC RC1SD-base-10 (Fig. 5.18)) compared with the observations (Fig. 5.13): in the tropical Pacific, the ITCZ and SPCZ shift equatorward, inducing strengthened (weakening) deep convection with positive (negative) precipitation anomalies across the equatorial Pacific and negative (positive) anomalies along the poleward flanks of the convergence zones during El Niño (La Niña). El Niño leads to reduced precipitation over the Maritime Continent, the eastern tropical Indian Ocean, the tropical

Atlantic Ocean, and Brazil, while enhanced rainfall is found over the western part of the Indian Ocean (except in JJA<sup>0</sup>). Opposites can be seen during La Niña episodes. Nevertheless, the models (Fig. 5.15-5.18) fail to capture the positive (negative) precipitation response from about the central Pacific (5°S, 160°W) to the southern Pacific (50°S, 120°W) in DJF<sup>+1</sup>. MPI-ESM AMIP and EMAC RC1-base-07 overestimate the positive (negative) precipitation anomalies over the equatorial Pacific in MAM<sup>+1</sup> when El Niño (La Niña) diminishes. The tropical rainfall biases in the MPI-ESM coupled simulation (Fig. 5.15) might be related to the errors in the simulated SST fields. As discussed in section 5.1.3.1, the simulated cold tongue extends too far into the western Pacific, producing an unrealistic narrow band of minimum precipitation over the equatorial central and eastern Pacific and contributing to the unrealistic double-ITCZ pattern with associated biases in precipitation in the MPI-ESM coupled.

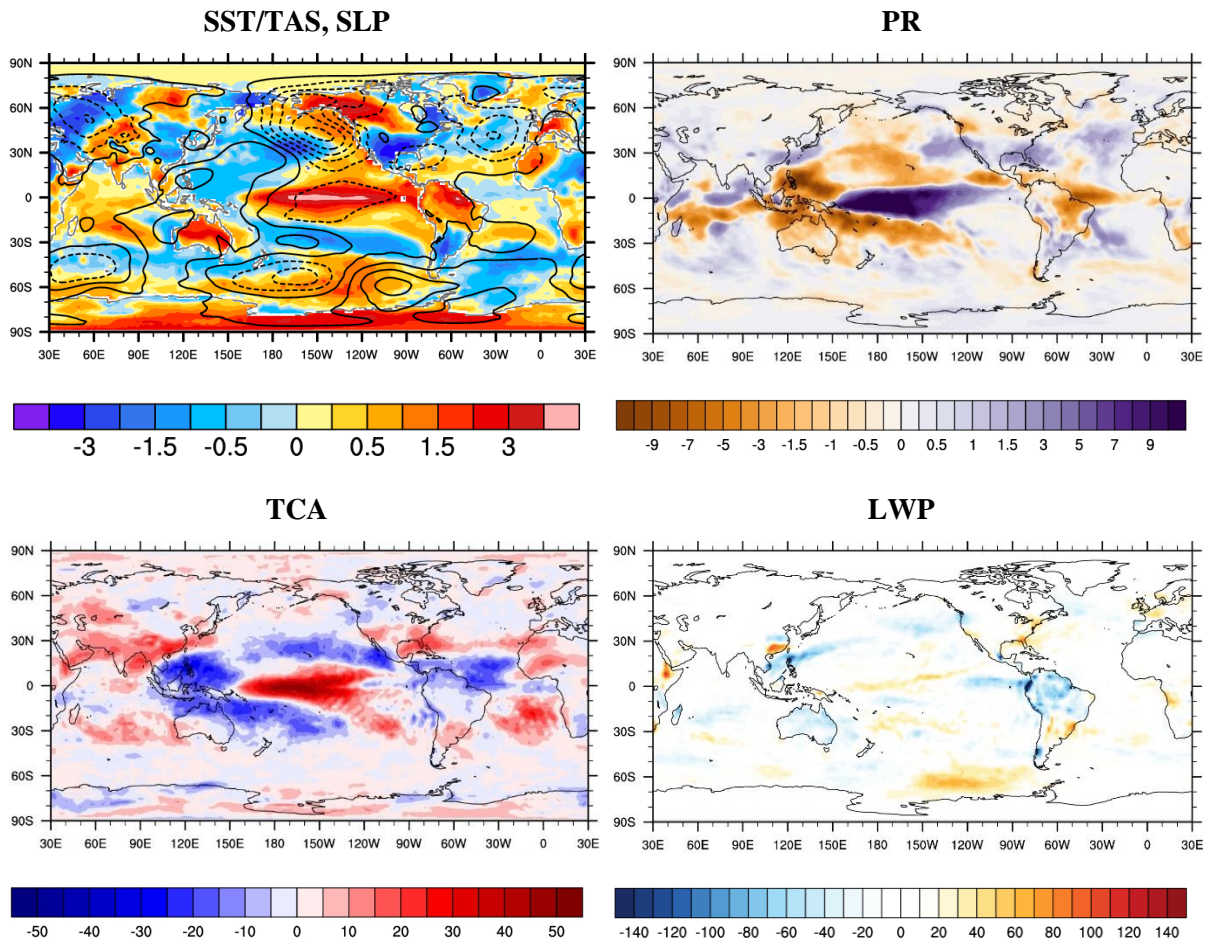


**Figure 5.16:** As in Figure 5.15, but for MPI-ESM AMIP.

## ENSO-related Total Cloud Amount Anomalies

TCA anomalies (Fig. 5.14) are strongly correlated to changes in the SST in the tropical Pacific. The warmer the water, the greater the evaporation, and the higher TCA due to more convective systems (Eastman et al. 2011). Colder SSTs mean less evaporation and lower TCA. A positive (negative) SST anomaly exhibits an increase (decrease) in TCA along the equator and the coast of South America during JJA<sup>0</sup> that subsequently grows in amplitude over the next several months, reaching its peak around DJF<sup>+1</sup>. With a warm event typically diminishing in MAM<sup>+1</sup>, the strong positive (negative) TCA anomalies also reduce at the same time. The strong correlation of the TCA anomalies with SST changes can also be seen in the MPI-ESM coupled (see Fig. 5.15) simulation during DJF<sup>+1</sup>. The centre of the ENSO-related TCA response over the tropical Pacific shifts too far to the west, in comparison to the observed location. The simulations with prescribed SSTs (MPI-ESM AMIP (Fig. 5.16), EMAC RC1-base-07 (Fig. 5.17), EMAC RC1SD-base-10 (Fig. 5.18) show a good spatial agreement of TCA anomalies during the peak months of El Niño or La Niña (DJF<sup>+1</sup>).

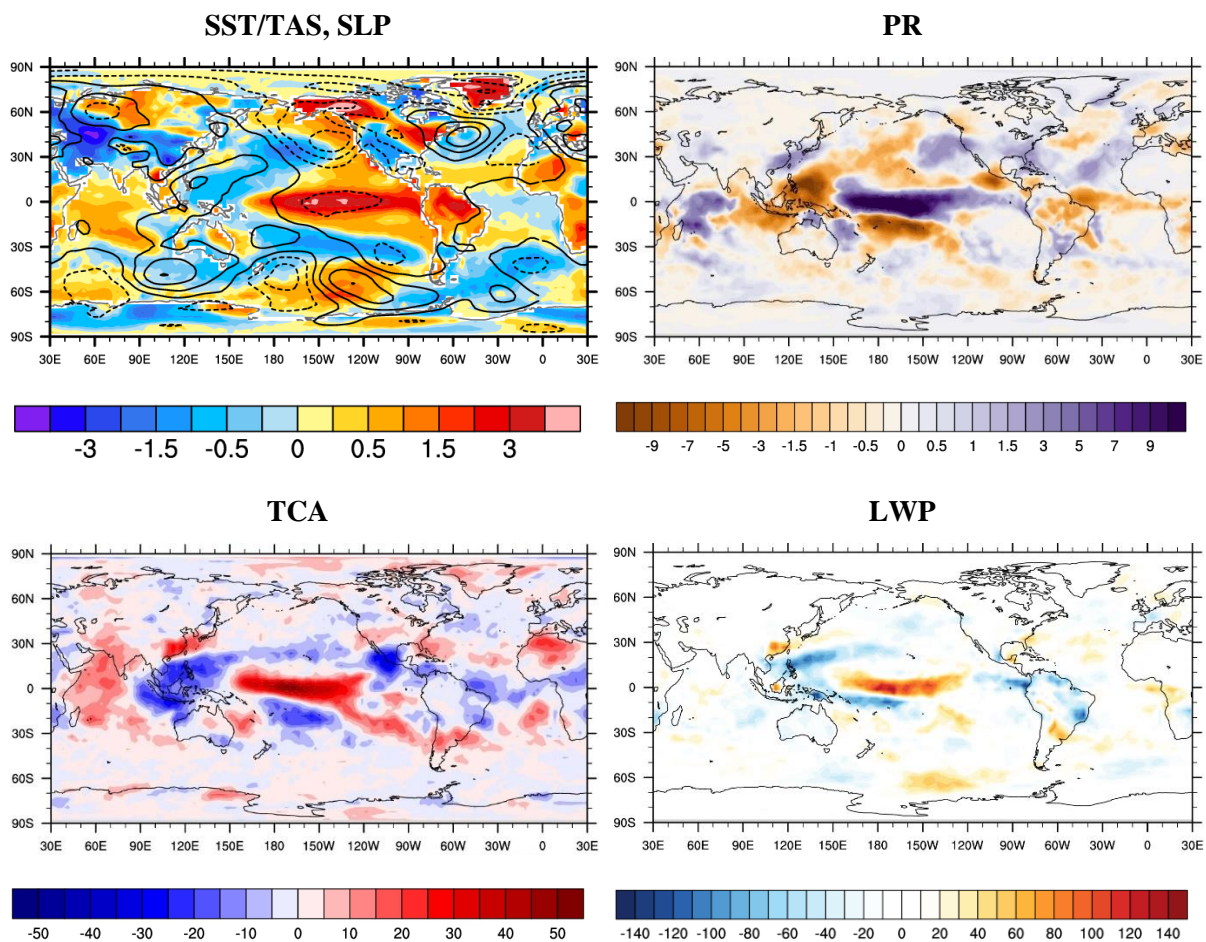


Figure 5.17: As in Figure 5.15, but for EMAC RC1-base-07.

## ENSO-related Liquid Water Path Anomalies

Over the tropical Pacific, LWP anomalies (Fig. 5.14) is positively correlated to changes in SSTs and precipitation, both in terms of the spatial structure and the temporal variability, and is strongest in DJF<sup>+1</sup>. While positive (negative) SST anomalies tend to be associated with higher (less) rainfall amounts, the geographical pattern of rainfall changes is greatly influenced by the ITCZ and SPCZ and their movements.

The link between LWP and rainfall is not surprising, as both are closely associated with the mean flow and convergence of moisture by the trade winds, while the latter is in turn linked to SST gradient patterns. The MPI-ESM coupled (Fig. 5.15), MPI-ESM AMIP (Fig. 5.16), and EMAC RC1SD-base-10 (Fig. 5.18) fail to reproduce observed positive (negative) LWP anomalies in the central Pacific, and negative (positive) LWP anomalies over the Maritime Continent during El Niño (La Niña) in DJF<sup>+1</sup>. That suggests, there is no linkage in these models in the simulated LWP response to the rainfall response during El Niño (La Niña).

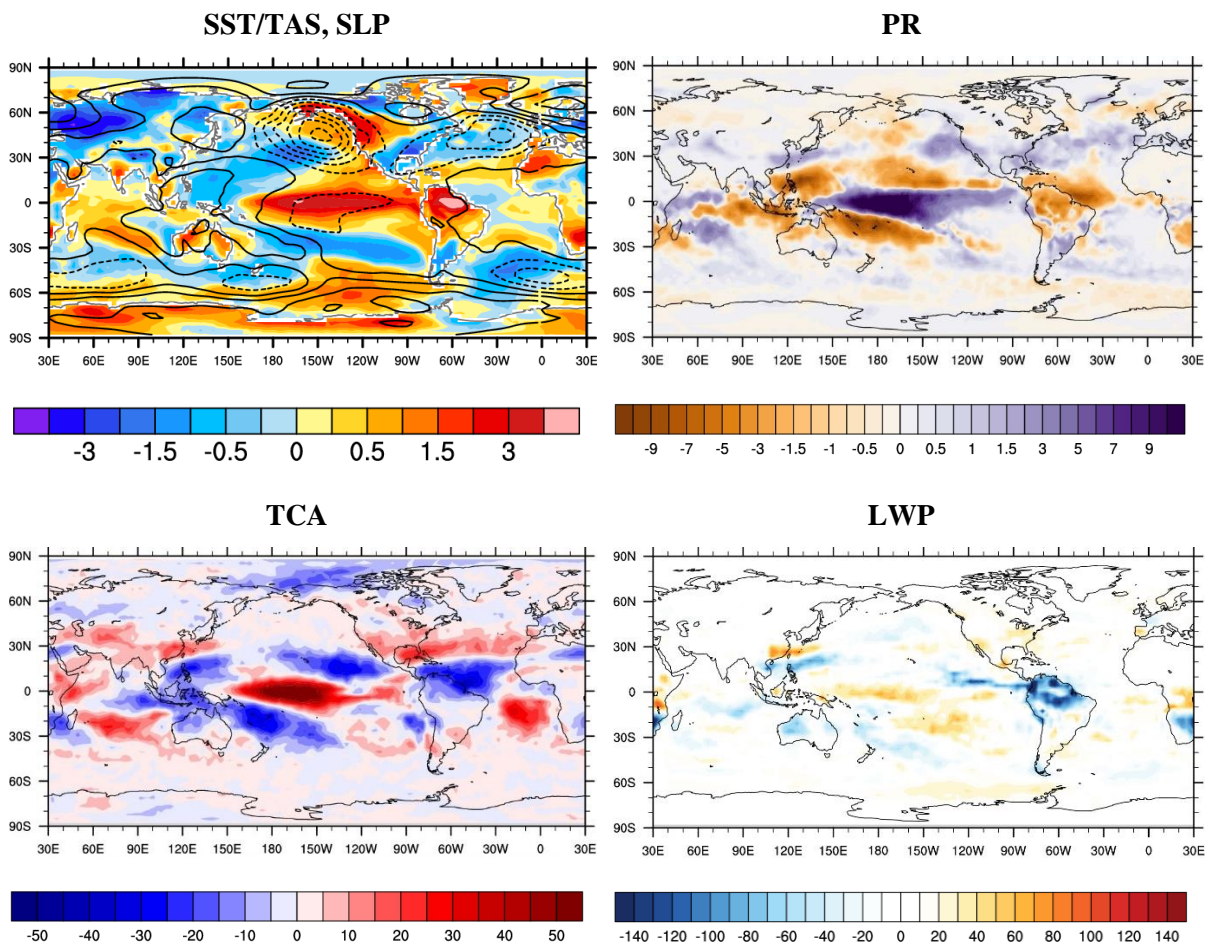


Figure 5.18: As in Figure 5.15, but for EMAC RC1SD-base-10.

A greater consistency with observations is found in the EMAC RC1-base-07 (Fig. 5.17) with positive (negative) LWP anomalies in the central Pacific, and negative (positive) LWP anomalies over the Maritime Continent during El Niño (La Niña) in DJF<sup>+1</sup>. The biases in the mean state of LWP impact directly the response of the cloud properties to ENSO.

Hence, a connection can be established between the no realistic response of the liquid water path to ENSO in the MPI-ESM coupled, MPI-ESM AMIP, and EMAC RC1SD-base-10 model simulation and the not realistic liquid water path distribution in these runs. In contrast, the EMAC RC1-base-07 simulates a more realistic liquid water path distribution and show a more realistic response to ENSO (see Figure 5.5).

### 5.3 Regional Impacts of ENSO and PDO on Clouds and Precipitation

In order to investigate the models' ability and systematic differences in the model setups reproducing observed amplitude of rainfall, total cloud amount, and liquid water path anomalies more qualitatively, three regions are investigated. Similar to Eastman et al. (2011), these regions are expected to be impacted to some degree by ENSO and PDO and that are characterized by very different cloud regimes. These regions include the ITCZ (deep convection, 0.5°S-13.5°N, 136°E-80°W), the NEP mid-latitudes (convective and stratiform clouds, 20°-50°N, 110°-140°W), and the SEP stratocumulus region (low-level marine clouds, 12.5-33.5°S, 70°-90°W).

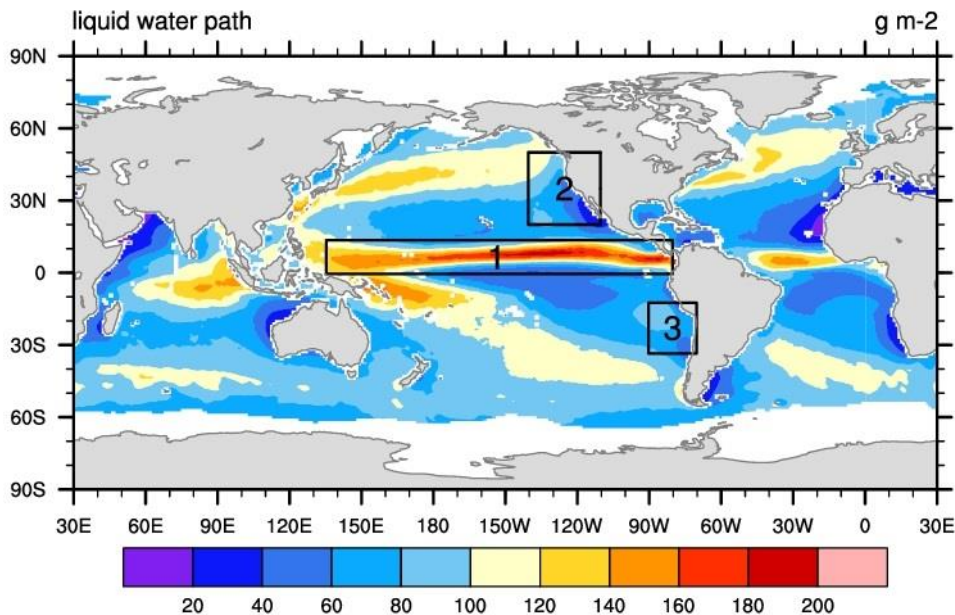


**Figure 5.19:** The three selected cloud regime regions, namely the tropics (0.5°S-13.5°N, 136°E-80°W) (1), the NEP mid-latitudes (20°-50°N, 110°-140°W) (2), and the SEP stratocumulus region (12.5-33.5°S, 70°-90°W) (3) used for a correlation analysis between the atmospheric variables and SST. Underlay the 17-yr average cloud liquid water path (1988-2005) in g per m<sup>2</sup> from the UWisc satellite climatology based on SSM/I, TMI, and AMSR-E (O'Dell et al., 2008).

The three cloud regime regions are shown in Fig. 5.19. As for ENSO (see Section 5.2.3.3), the relationship of changes in the patterns of pressure, wind, and temperature as a response to the PDO have been investigated by Mantua et al. (1997). This includes a possible connection between the PDO (given by the PDO index) and regional changes in precipitation, cloud amount and liquid water path. The question is which role teleconnections (climate anomalies being related to each other at large distances) are playing in the atmospheric response to SST changes in comparison with local SST anomalies. For this purpose, the temporal correlation is calculated between SST anomalies averaged over the (1) Nino-3.4 region, (2) the PDO region, and (3) local domain and atmospheric variables for all three cloud regime regions. Another question addressed is whether the model simulations correctly reproduce the observed relationship between atmospheric variables and SSTs. The 12-month running mean time series of the atmospheric variables and anomalies in the SST indices are used to examine their possible relationship. A difficulty when assessing teleconnections in coupled model simulations such as that from MPI-ESM is that biases in the ENSO dynamics (e.g., in amplitude or spatial distribution of the main SST anomaly in the equatorial Pacific) degrade the quality of the simulation already at the source region before the onset of any teleconnection mechanisms (Joseph and Nigam, 2006). The model simulations with prescribed SSTs naturally include the observed seasonal ENSO SST evolution, whereas the global teleconnections of ENSO with remote regions depend on the atmospheric component of the models.

### 5.3.1 Tropics

A positive correlation between variables (PR, TCA, and LWP), and local SST and the Nino-3.4 index is found in the observational data (Fig. 5.20) for the tropics. In the tropical region, warmer waters lead directly to enhanced surface evaporation and low-level moisture convergence and then to more rainfall, total cloud amount, and liquid water path. Convective processes are predominant in the tropical central and eastern Pacific (Trenberth and Shea, 2005; Wang et al., 2005).

These results in terms of the positive correlation between precipitation and the SST indices (PDO index, Nino-3.4 index and local SST changes) are very well reproduced by the models (see Tab. 5.6 for correlation coefficients). The models, however, fail to capture the observed LWP-SST relationship. A reason could be the incorrect representation of the mean state of LWP. In contrast to the high local SST and Nino-3.4 SST index correlation, the influence of the PDO is less relevant in the tropics (0.46 (PR), 0.37 (TCA), 0.47 (LWP) in the observations). The model simulations show a qualitatively similar correlation between PR, TCA and the PDO index. A correct positive correlation between the PDO index and LWP is only simulated by the free-running EMAC.

The observed rainfall-SST correlation is better reproduced in the MPI-ESM coupled simulation compared to the MPI-ESM AMIP simulation. MPI-ESM AMIP and MPI-ESM coupled both fail to even capture the correct sign of the observed correlation between LWP and all three of the investigated SST indices.

The EMAC RC1-base-07 simulation reproduces the observed positive correlation between the local SST and the Nino-3.4 SST index with PR (0.83/0.77), TCA (0.84/0.79), and LWP (0.24/0.18) quite well. There is also a stronger relationship between PDO and the atmospheric variables in the free-running EMAC RC1-base-07 than in the observational data. In contrast, EMAC RC1SD-base-10 shows lower correlation coefficients between PR and TCA and the PDO index. Additionally, the LWP values are anti-correlated with changes in SST.

**Table 5.6:** Linear cross-correlation coefficients at lag zero, tropics (0.5°S-13.5°N, 136E°-80°W).

Tropics	PDO region			Local (tropics)			Niño-3.4 region		
	PR	TCA	LWP	PR	TCA	LWP	PR	TCA	LWP
<b>Observations</b>	<b>0.46</b>	<b>0.37</b>	<b>0.47</b>	<b>0.81</b>	<b>0.50</b>	<b>0.80</b>	<b>0.78</b>	<b>0.54</b>	<b>0.74</b>
<b>MPI-ESM coupled</b>	0.37	0.34	-0.29	0.83	0.75	-0.71	0.86	0.77	-0.77
<b>MPI-ESM AMIP</b>	0.45	0.48	-0.50	0.73	0.76	-0.67	0.63	0.67	-0.70
<b>EMAC RC1-Base-07</b>	0.51	0.49	0.26	0.83	0.84	0.24	0.77	0.79	0.18
<b>EMAC RC1SD-Base-10</b>	0.36	0.16	-0.73	0.68	0.65	-0.44	0.65	0.61	-0.45

TROPICS (0.5°S-13.5°N, 136°E-80°W)

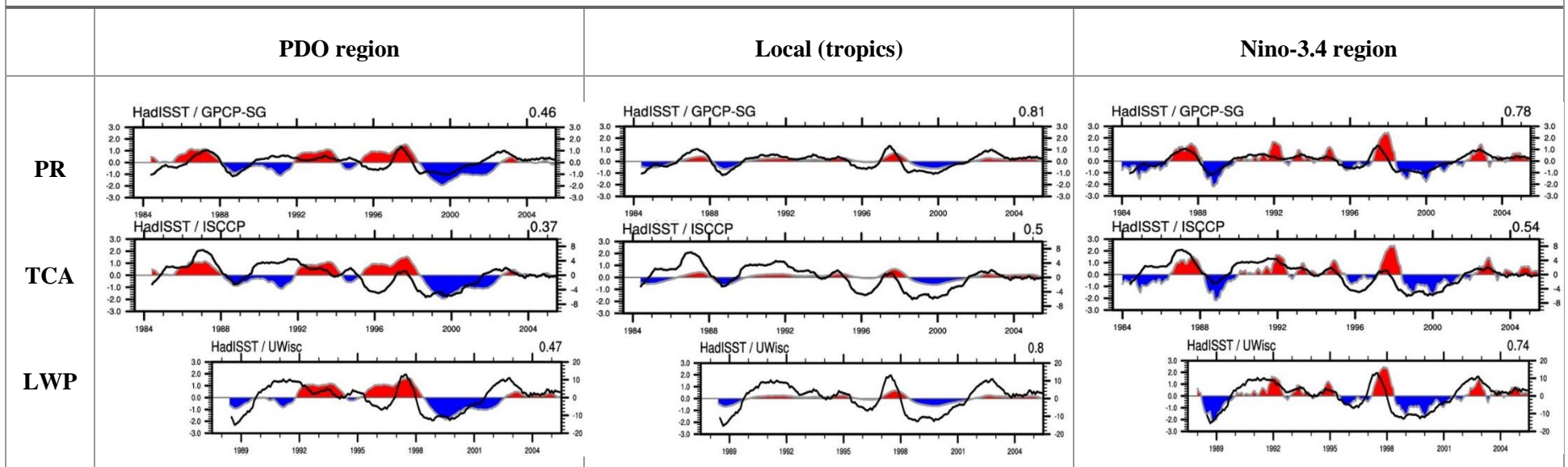


**Figure 5.20:** 12-month running mean time series of (left column) the observed SST anomalies averaged of the PDO region (20°-70°N, 110°E-100°W), (middle column) the “local” (0.5°S-13.5°N, 136°E-80°W) SST, (right column) the Nino-3.4 SST region (5°N-5°S, 120°-170°W), and anomalies of (top row) PR, (middle row) TCA, and (bottom row) LWP averaged over the tropics (0.5°S-13.5°N, 136°E-80°W). The time series (PR, TCA) span from 1984 through 2005 and 1988-2005 (LWP). The linear cross-correlation coefficients at lag zero between two investigated time series and the observations used are given above each plot.

### 5.3.2 NEP mid-latitudes

One of the responses of the atmospheric circulation to ENSO as a consequence of changes in the patterns of deep tropical convection is a shift of the North Pacific jetstream (storm track). Observations show that ENSO is strongly correlated with a strengthening of the Aleutian Low, and is accompanied by changes in the Walker circulation, the distribution of clouds, and precipitation (Deser et al. 2012).

Tab. 5.7 summarizes the correlation coefficients between the SST anomalies averaged over the PDO region, the Niño-3.4 region, and local domain and the atmospheric variables PR, TCA, and LWP calculated from the observational data (Fig. 5.21) and the model simulations.

In the observational data, a warming of the local SST is related to a decrease in TCA (-0.42), but an increase in rainfall (0.60) due to strengthened convective activity and a reduction in LWP (-0.16). The models qualitatively reproduce these relationships, but the simulated negative correlations are generally weaker.

An agreement can be seen in the positive correlation between the SST anomaly averaged over the Niño-3.4 region and precipitation (0.46), the effects on the cloud properties TCA (-0.16), and LWP (0.08) are weak. The models are able to reproduce the observed positive correlation of the SST anomaly in the Niño-3.4 region with precipitation.

**Table 5.7:** Linear cross-correlation coefficients at lag zero, mid-latitudes (20°-50°N, 110°-140°W).

NEP midlatitudes	PDO region			Local (NEP mid-latitudes)			Niño-3.4 region		
	PR	TCA	LWP	PR	TCA	LWP	PR	TCA	LWP
<b>Observations</b>	<b>-0.45</b>	<b>-0.25</b>	<b>-0.21</b>	<b>0.60</b>	<b>-0.42</b>	<b>-0.16</b>	<b>0.46</b>	<b>-0.16</b>	<b>0.08</b>
<b>MPI-ESM coupled</b>	0.03	0.18	0.09	0.47	-0.10	-0.05	0.45	0.25	0.39
<b>MPI-ESM AMIP</b>	-0.27	-0.22	-0.63	0.26	-0.24	-0.50	0.44	0.18	-0.33
<b>EMAC RC1-Base-07</b>	-0.23	-0.18	-0.42	0.42	-0.07	-0.29	0.28	-0.02	-0.37
<b>EMAC RC1SD-Base-10</b>	-0.12	-0.54	-0.23	0.42	-0.50	-0.14	0.38	-0.34	-0.13

NEP MID-LATITUDES (20°-50°N, 110°-140°W)

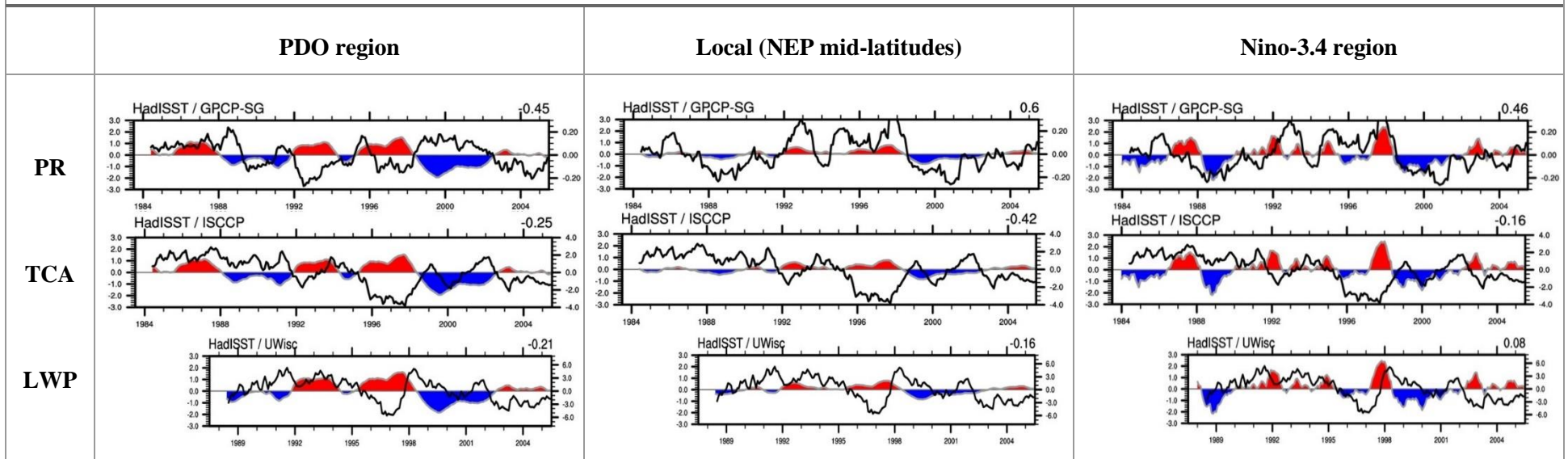


Figure 5.21: As Fig. 5.20 but for the NEP mid-latitudes (20°-50°N, 110°-140°W).

### 5.3.3 SEP Stratocumulus Region

The stratocumulus deck over the south eastern Pacific is the largest and most persistent subtropical stratocumulus deck in the world (e.g., Wood et al., 2011; Mechoso et al., 2014). It is formed and maintained by complex interactions between the underlying cold SST, the marine boundary layer capped by warm and dry air, high tropospheric stability and complex physical processes (e.g., Lin et al., 2014). These stratocumulus clouds typically do not generate significant amounts of precipitation and stretch far westward off the coast of Peru.

During El Niño, anomalously warm waters cover the eastern tropical Pacific. As a result, the stratocumulus clouds are partly replaced by cumulus clouds that can bring some rain near the coast. As a consequence of this transition in cloud type, TCA is decreased. The observed TCA and LWP are therefore anti-correlated with anomalies in the local SST (-0.52) (cf. Tab. 5.8 and Fig. 5.22). In contrast, the correlation of local SST changes with precipitation is weak (0.18). The simulations with prescribed SST (MPI-ESM AMIP, EMAC RC1-base-07, and EMAC RC1SD-base-10) capture the observed anti-correlation between the local SST and TCA reasonably well (see cross-correlation coefficients in Tab. 5.8), while the coupled simulation shows an unrealistic positive correlation between TCA and local SST.

The correlation coefficients (between PR, TCA, LWP and the SST indices) of MPI-ESM AMIP show a good agreement with the ones calculated from the observations, especially an influence of the SST anomalies averaged over the PDO region and of local SST anomalies on TCA and LWP can be seen. The MPI-ESM coupled simulation reproduces this relationship for LWP, but shows a positive correlation between the SST anomalies and TCA, which is of the opposite sign than the one calculated from the observations.

SST anomalies averaged over the Niño-3.4 region affect the clouds in the stratocumulus region similarly to the above discussed changes in local SST. This is not surprising as changes in local SST in the stratocumulus region are strongly correlated with those averaged over the Niño3.4 region (ENSO). A significant correlation of the cloud properties and precipitation in the stratocumulus region with SST anomalies averaged over the PDO was not found.

Due to complex physical processes and feedbacks, a realistic simulation of the stratocumulus cloud deck has proven particularly difficult for coupled climate models (Hannay et al., 2009, Wyant et al., 2009). The MPI-ESM coupled simulates a correlation coefficient between the local SST anomalies with TCA of the opposite sign than the one derived from the observational data.

SEP STRATOCUMULUS REGION (12.5-33.5°S, 70°-90°W)

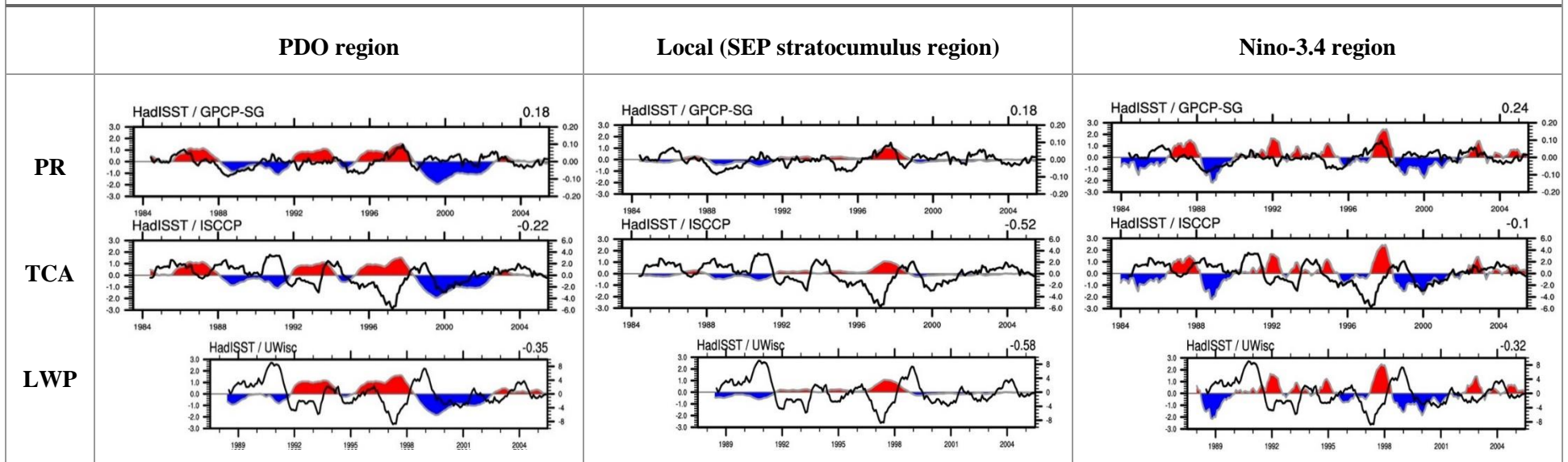


Figure 5.22: As Fig. 5.20 but for the SEP stratocumulus region (12.5-33.5°S, 70°-90°W)

**Table 5.8:** Linear cross-correlation coefficients at lag zero, SEP stratocumulus region (12.5-33.5°S, 70°-90°N).

SEP Stratocumulus	PDO region			Local (SEP stratocumulus region)			Niño-3.4 region		
	PR	TCA	LWP	PR	TCA	LWP	PR	TCA	LWP
<b>Observations</b>	<b>0,18</b>	<b>-0,22</b>	<b>-0,35</b>	<b>0,18</b>	<b>-0,52</b>	<b>-0,58</b>	<b>0,24</b>	<b>-0,1</b>	<b>-0,32</b>
<b>MPI-ESM coupled</b>	0,40	0,42	-0,29	0,33	0,37	-0,38	0,26	0,49	-0,62
<b>MPI-ESM AMIP</b>	0,49	-0,09	-0,50	0,28	-0,15	-0,38	0,3	0,06	-0,61
<b>EMAC RC1-Base-07</b>	0,18	-0,39	-0,46	-0,11	-0,51	-0,65	-0,12	-0,3	-0,42
<b>EMAC RC1SD-Base-10</b>	-0,35	-0,47	-0,77	-0,31	-0,34	-0,47	-0,22	-0,08	-0,56

## 5.4 The Role of the Model Setup

In this section, the impact of the model setup, i.e. coupled vs. atmosphere-only and free-running vs. nudged, on the simulated effect of climate modes on clouds and precipitation is analysed. This is done by comparing two simulations with MPI-ESM, one performed with a coupled ocean and one with prescribed SSTs (Section 5.4.1). The aim is to find similarities and important differences in the results between the different model setups. The same is also done for the free-running EMAC RC1-base-07 and the nudged EMAC RC1SD-base-10 simulation, which is discussed in section. 5.4.2.

### 5.4.1 MPI-ESM coupled vs. MPI-ESM AMIP

Common biases in the simulated annual mean SST in the Pacific in many coupled atmosphere-ocean models such as MPI-ESM (coupled) include a warm SST bias in the southeast Pacific stratocumulus region, a cold SST bias in the equatorial cold tongue and in parts of the North Pacific (Lin and Xie 2014). Errors in the equatorial SST are affecting the simulated mean precipitation and total cloud amount and are the reason for an unrealistic so-called double ITCZ. Even though the MPI-ESM AMIP does not suffer from SST biases (due to prescribed SSTs), precipitation biases are found over the western equatorial Pacific and the Indian Ocean (see Section 5.1.2). The correlation coefficient of the simulated geographical distribution of annual mean rainfall with GPCP-SG observations is smaller for

MPI-ESM coupled (0.77) than for MPI-ESM AMIP (0.87) data. Similarities can be found in the poor representation of simulated mean LWP pattern in both MPI-ESM simulations.

In section 5.2.3.3, the teleconnections related to the ENSO evolution were analysed. Both MPI-ESM simulations fail to capture the increase of LWP during El Niño over the equatorial Pacific and the decrease of LWP over the Maritime Continent shown in figure 5.15 (MPI-ESM coupled) and figure 5.16 (MPI-ESM AMIP). The MPI-ESM coupled simulates an unrealistic narrow band of minimum precipitation over the equatorial and eastern Pacific. The maximum amplitude of rainfall is shifted too far to the west.

In order to analyse the teleconnections of natural climate variabilities more qualitatively and to assess the performance of the model simulations, three regions have been investigated (see Section 5.3). These regions (tropics, NEP mid-latitudes and SEP stratocumulus region) are affected to some degree by ENSO and the PDO. Additionally, the role of anomalies in local SSTs have been examined.

In the tropics, both simulations capture well the observed correlation between local SST variations, SST anomalies averaged over the PDO region and the Niño-3.4 region and the atmospheric variables PR and TCA. But both MPI-ESM model simulations fail to reproduce the observed positive correlation of the SST anomalies with LWP.

In the NEP midlatitudes, the observed anti-correlation of the SST anomalies averaged over the PDO region with PR (-0.45), TCA (-0.25), and LWP (-0.21) is well reproduced in the AMIP simulation (PR (-0.27), TCA (-0.22), LWP (-0.63)). A good agreement with the observed correlations is found between the Niño-3.4 index and PR in both simulations. Local SST changes are positively correlated with PR anomalies, and negatively correlated with TCA and LWP anomalies. This is the case for both, the AMIP and the coupled simulation.

In the SEP stratocumulus region, the MPI-ESM AMIP also reproduces the signs of the observed relationships between SST anomalies averaged over the PDO region, the Niño-3.4 region, and local SST changes and the atmospheric variables, i.e., positive correlations with PR and negative correlations with TCA and LWP. The coupled model is capable to reproduce the positive correlation of the SST anomalies (PDO region, Niño-3.4 region and local SST) with PR and the anti-correlation with LWP. The observed anti-correlation of the SST anomalies with TCA, however, is not reproduced in the coupled simulation.

In summary, the differences in the performance of the coupled and the atmosphere-only model runs with MPI-ESM in reproducing the observed relationships between PDO, ENSO, and local SST changes and cloud parameters and precipitation are rather small. In particular, the model run with prescribed SSTs does not systematically outperform the coupled model setup. However, the coupled model does not reproduce the observed anti-correlation between TCA anomalies and local SST changes in the SEP stratocumulus region in contrast to MPI-ESM AMIP. Another difference can be found in an unrealistic narrow band of minimum precipitation over the equatorial and eastern Pacific

simulated by the MPI-ESM coupled. This is not the case for MPI-ESM AMIP with prescribed SSTs. In addition, the region with maximum rainfall rates is shifted too far to the west in the MPI-ESM coupled run. This suggests that the biases in the mean state of precipitation impact directly the rainfall response to ENSO, which are partly affected by biases in the simulated mean SST in the MPI-ESM coupled in the tropical Pacific. In conclusion, the errors in the mean SST pattern impact the quality of the simulation of modes of climate variabilities (PDO, ENSO) at the source region in the MPI-ESM coupled. Thus the error susceptibility is increased in simulating teleconnections related to climate variabilities.

#### **5.4.2 EMAC RC1-base-07 vs. EMAC RC1SD-base-10**

In order to analyse the impact of atmospheric nudging on the simulated sensitivity of cloud parameters and precipitation to the climate modes ENSO and PDO, the free-running (RC1-base-07) and a nudged (RC1SD-base-10) EMAC simulation are compared.

The nudged EMAC RC1SD-base-10 run shows an improved representation of the annual mean precipitation in the western equatorial Pacific, but increased overestimation in precipitation in the western Indian Ocean compared to the free-running EMAC RC1-base-07 experiment. The pattern correlation of the annual mean precipitation with observations is slightly higher in the nudged EMAC run (0.83) than in the free-running EMAC RC1-base-07 simulation (0.79). A strong underestimation of the annual mean TCA is found in the Southeast Pacific in the nudged simulation (up to -35%), but the simulation of clouds in the western Pacific is improved compared to the free-running simulation (10-25%). Nevertheless, both model simulations, EMAC RC1SD-base-10 (68 %) and EMAC RC1-base-07 (64 %), overestimate the annual mean TCA compared with the ISCCP observations (60%). Both model simulations do not reproduce the geographical distribution of the mean LWP well. The RMSE in EMAC RC1-base-07 ( $32 \text{ g m}^{-2}$ ) is significant smaller than that from the nudged version ( $40 \text{ g m}^{-2}$ ). The spatial correlation of the annual mean LWP of the EMAC RC1-base-07 with observations is 0.59, and for EMAC RC1SD-base-10 is 0.46.

The free-running EMAC RC1-base-07 and the nudged EMAC RC1SD-base-10 generally reproduce the observed response to ENSO in terms of the corresponding changes in temperature, precipitation, and cloud properties reasonably well. Examples for the correct representation are the maximal amplitude of rainfall and cloudiness over the central equatorial Pacific and drier conditions as well as less cloudiness over the Maritime Continent. The wintertime deepening of the Aleutian Low is too weak simulated in EMAC RC1-base-07 compared with the observations and with EMAC RC1SD-base-10. The nudged model simulation fails to capture the positive LWP response to ENSO in the equatorial Pacific during the ENSO peak phase.

In order to further investigate the influence of nudging on teleconnections of natural climate variabilities with the hydrological parameters PR, TCA, and LWP, a qualitative analysis is done for the three regions tropics, NEP mid-latitudes and the SEP stratocumulus region. All of these regions are impacted to some degree by ENSO and PDO. Additionally, the role of local SST changes is being examined.

In the tropics, the free-running simulation captures the relationship between the local SST variations, SST anomalies averaged over the PDO and the Nino-3.4 region and the atmospheric variables PR, TCA and LWP well. The nudged simulation shows good agreement with the observed relationships between the SST anomalies and PR and TCA. It fails, however, to capture the observed positive correlation between the SST anomalies and LWP. Both model simulations fail to capture the observed positive correlation between the SST anomalies and LWP.

In the NEP mid-latitude region, both simulations reproduce the observed anti-correlation of the SST anomalies in the PDO region with PR, TCA, and LWP. A better agreement with the observed relationship between local SST changes as well as between the Nino-3.4 SST anomalies and PR, TCA and LWP is found in the nudged simulation compared to the free-running simulation. This suggests that the influence of atmospheric nudging is more important for the hydrological cycle in higher latitudes.

In the SEP stratocumulus region, the EMAC RC1-base-07 simulation reproduces the observed correlations between the PDO SST anomalies and the hydrological parameters PR, TCA, and LWP reasonably well. The nudged version simulates a correlation of the PDO SST anomalies with PR of opposite sign than the one derived from the observational data. The observed relation of local SST changes and the three atmospheric parameters is better captured by the free-running version, such as increasing SST leading to a reduction in TCA. The Nino-3.4 SST anomalies affect clouds in the stratocumulus region similarly to the changes in local SSTs.

In summary, the differences in the performance of the free-running and the nudged atmosphere-only model runs with EMAC in reproducing the observed relationships between PDO, ENSO, or local SST changes with cloud parameters and precipitation are rather small. The free-running EMAC shows a slightly better agreement with the observed correlations between the hydrological parameters and the SST indices in the tropics and the SEP stratocumulus region, where convective processes are predominant. In the NEP mid-latitudes, the nudged EMAC slightly outperforms the free-running in terms of the above mentioned correlation coefficients. This suggests that the atmospheric nudging is more important for the hydrological cycle in higher latitudes. Nevertheless, the atmospheric nudged run does not systematically outperform the free-running model setup.

## 6 Summary and Outlook

The main focus of this study was a quantitative assessment of performance of selected climate models in reproducing the observed modes of natural climate variabilities El Niño-Southern Oscillation (ENSO) and Pacific Decadal Oscillation (PDO) as well as the impact of these climate modes on cloud parameters and precipitation. For this, a coupled and an atmosphere-only simulation with the Max Planck Institute Earth System Model (MPI-ESM) as well as a nudged and a free-running simulation with the Atmospheric Chemistry model EMAC are analysed and compared to a variety of different observational data sets.

In order to evaluate in particular the performance of the MPI-ESM coupled model, the NCAR Climate Variability Diagnostics Package has been implemented into the Earth System Model Evaluation Tool. The ESMValTool is a software tool developed by multiple institutions which aims at improving routine Earth System Model evaluation. The CVDP computes key metrics of internal climate variability for a set of user-specified model simulations and observational data sets.

In order to assess the performance of the MPI-ESM coupled simulation (1870-2005) with free-running ocean in simulating the spatial structure and the temporal variability of the PDO, an EOF analysis of the SST has been applied over the North Pacific. The spatial pattern of the PDO simulated by the MPI-ESM coupled is quite realistic, except a smaller percentage of variance explained by the first EOF (PDO) compared to the CMIP5 multi model mean and to observations. In terms of temporal variability, the MPI-ESM coupled produces a periodic response of approximately the same frequency as observed – that is, periods of 3 – 7 years for ENSO, and 20 – 30 years for the PDO. However, with regard to the asymmetric temporal evolution between the observed warm (El Niño) and cold (La Niña) ENSO events, the MPI-ESM coupled only weakly resembles the observed asymmetry. Furthermore, the model fails to capture the observed strong phase locking to the seasonal SST cycle. Nevertheless, the MPI-ESM coupled generally simulates a quite realistic SST evolution of ENSO. In conclusion, the results suggest that errors in the mean SST pattern impact the quality of the simulation of modes of climate variabilities (PDO, ENSO) at the source region in the MPI-ESM coupled. Thus the error susceptibility is increased in simulating teleconnections related to climate variabilities.

Then, shorter simulations with the MPI-ESM using prescribed SSTs (so-called Atmospheric Model Intercomparison Project experiment) from 1984 – 2005 as well as a free-running and a nudged simulation with the atmosphere-only model EMAC (also with prescribed SSTs) have been additionally analysed. In the nudged configuration of EMAC, atmospheric variables like temperature, vorticity, and divergence are continuously forced towards reanalysis data while the hydrological cycle can evolve freely. The model simulations with prescribed SSTs naturally include the observed seasonal ENSO SST evolution, whereas the teleconnections of ENSO and PDO with remote regions depend on the atmospheric component of the models.

To evaluate the hydrological teleconnections resulting from the ENSO SST evolution and to assess systematic differences between the different model setups (i.e., coupled vs. atmosphere-only, nudged vs. free-running), new diagnostics were implemented into the ESMValTool-CVDP combination.

Before evaluating and analysing the impact of the climate modes PDO and ENSO on cloud properties and precipitation, the performance of the models in reproducing observed basic climate variables has been assessed. The evaluation of the annual mean state of the cloud properties (precipitation, total cloud amount, and liquid water path) showed that the models generally have difficulties in reproducing the observed mean cloud properties very well. The evaluation also showed that the performance of the MPI-ESM coupled simulation and the MPI-ESM AMIP and the two EMAC simulations in reproducing the observed cloud climatologies is quite similar, i.e., the atmosphere-only models do not systematically outperform the coupled run in simulating the observed mean cloud properties. This suggests that the deficiencies in model cloud simulations may be rather attributable to the cloud, convection, and boundary layer parameterization than to biases in simulated SSTs.

Despite some difficulties in reproducing the observed basic climate variables, the MPI-ESM AMIP, free-running and nudged EMAC model simulations generally simulate teleconnections of the atmospheric circulation with ENSO including corresponding changes in temperature, precipitation, and cloud properties reasonably well. The free-running EMAC version underestimates the wintertime deepening of the Aleutian Low. The MPI-ESM coupled produces an unrealistic narrow band of minimum precipitation over the equatorial and eastern Pacific. The maximum amplitude of rainfall is shifted too far to the west in the MPI-ESM coupled run. The errors in the simulated SST also affect the simulated precipitation pattern. The MPI-ESM coupled, MPI-ESM AMIP, and the nudged EMAC simulations fail to capture the positive liquid water path response to ENSO in the equatorial Pacific during the ENSO peak phase.

To analyse the teleconnections of natural climate variabilities more qualitatively and to assess the systematic differences between the model simulations, three region with different cloud regimes have been investigated. These regions (tropics, NEP mid-latitudes and SEP stratocumulus region) are impacted to some degree by ENSO and PDO. Additionally, the role of local SST changes has been examined. The correlation of SST anomalies and the parameters PR, TCA, and LWP between the model simulations and observational data is considered as a measure of models' performance.

Systematic differences in the performance of the coupled and the atmosphere-only model runs with MPI-ESM in reproducing the observed relationships between PDO, ENSO, and local SST changes and cloud parameters and precipitation are rather small. In particular, the model run with prescribed SSTs do not systematically outperform the coupled model setup. Nevertheless, a disagreement to the observations can be found in the correlation of TCA anomalies and local SST changes in the coupled model in the SEP stratocumulus region. In addition, the coupled model simulates a narrow band of

minimum precipitation over the equatorial and eastern Pacific and westward shift of the maximum amplitude of rainfall which is a common problem of many coupled models.

In order to analyse the impact of atmospheric nudging on the hydrological cycle, a free-running and a nudged EMAC simulation are compared. The performance of both EMAC in reproducing the observed correlations between PDO, ENSO and changes in the local SST and cloud parameters and rainfall are rather small. The free-running EMAC shows a slightly better agreement with the observed correlations between the hydrological parameters and the SST anomalies in the tropics and the SEP stratocumulus region. In the NEP mid-latitudes, the nudged EMAC slightly outperforms the free-running in terms of the above mentioned correlation coefficients. This suggests that the atmospheric nudging is improving the simulation of the hydrological cycle in higher latitudes. Nevertheless, the atmospheric nudged run does not systematically outperform the free-running model setup.

Further investigations of natural climate variabilities and resulting hydrological teleconnections could also look at additional variables such as meridional and zonal wind components and take a closer look at the sea level pressure. In addition, part of deficiencies in simulating annual mean cloud properties and precipitation is probably related to the parametrizations of the relevant atmospheric processes within in the models. A logical next step would include a process analysis of the relevant processes such as convection and boundary layer physics with the aim to improve the parametrizations. Further research on the coupling processes between ocean and atmosphere is needed to identify and improve the understanding of the relevant feedback processes, which lead to SST anomalies in the equatorial (ENSO) and northern (PDO) Pacific.

Uncertainties exist also in the reference data that needs to be better understood and taken into account when evaluating the performance of climate models.

## 7 Acknowledgements

This work was performed as part of the DLR KliSAW (“Klimarelevanz von atmosphärischen Spurengasen, Aerosolen und Wolken: Auf dem Weg zu EarthCARE und MERLIN“) project within the Earth System Model Evaluation (ESMVal) Group.

First of all, I would like to express my gratitude to Veronika Eyring for giving me this unique opportunity to write my final thesis at DLR on this interesting topic and for the great insight on earth sciences this possibility gave me and for supervising me. Many thanks go to Axel Lauer for all the hours he spent with me interpreting the results, for the valuable comments and informations about all the science stuff he always provided, his proofreading of the thesis and for his strong support, not only in the final days of this thesis.

Furthermore, I owe thanks to Daniel Senfleben for introducing me to the command language NCL and for his help with sorting out technical problems.

I want to also thank Sabrina Wenzel, Mattia Righi and Franziska Frank for always having an open ear for me when I had questions of all kinds.

I also thank my colleagues at the department for offering a one-of-a-kind familiar working environment. There, special thanks go to my room colleagues Michael Löffler and Moritz Dreusicke.

Thanks to Adam Phillips and Clara Deser for providing us with the NCAR Climate Variability Diagnostics Package (CVDP) that substantially supported the analysis of this thesis.

Last but not least, I want to thank my family for their help, particular my parents and my girlfriend who supported me over all the years and made it possible to successfully complete this final step.

## 8 References

- AchutaRao, K., and K. Sperber, 2006: ENSO simulations in coupled ocean-atmosphere models: Are the current models better? *Clim. Dyn.*, 27, 1–16.
- Adler, R. F., et al., 2003: The version 2 global precipitation climatology project (GPCP) monthly precipitation analysis (1979-present). *J. Hydrometeorol.*, 4(6), 1147-1167.
- Alexander M. A., 2010: Extratropical air-sea interaction, sea surface temperature variability, and the Pacific Decadal Oscillation. *Climate Dynamics: Why does Climate Vary?*, Geophys. Monogr., Vol. 189, *Amer. Geophys. Union*, 123-148.
- Alexander M. A., Blade I., Newman M., Lanzante J.R., Lau N.-C., Scott J.D., 2002: The atmospheric bridge: the influence of ENSO teleconnections on air-sea interaction over the global oceans. *J. Climate*, 15:2205–31
- An, S.-I. 2008: Interannual variations of the tropical ocean instability wave and ENSO. *J. Climate*, 21, 3680-3686
- Battisti, D. S., and Hirst, A. C., 1989: Interannual variability in the tropical atmosphere-ocean model: influence of the basic state, ocean geometry and nonlinearity. *J. Atmos. Sci.*, 45, 1687- 1712.
- Bjerknes, J., 1969: Atmospheric teleconnections from the equatorial Pacific. *Mon. Weather Rev.*, 97, 163-172.
- Bloomfield, P., 2000, *Fourier analysis of time series: an introduction*, second edition: New York, John Wiley & Sons, Inc., 261 p.
- Capotondi, A., and A. Wittenberg, 2013: ENSO diversity in climate models. *U.S. CLIVAR Variations*, 11, 10-14.
- Cayan, D. R. 1996: Interannual climate variability and snowpack in the western United States. *Journal of Climate*, 9(5), 928-948.
- Dai, A., 2006: Precipitation characteristics in eighteen coupled climate models. *J. Climate*, 19, 4605-4630.
- De Szoeko, S. P., and S. P. Xie, 2008: The tropical eastern Pacific seasonal cycle: Assessment of errors and mechanisms in IPCC AR4 coupled ocean – atmosphere general circulation models. *J. Clim.*, 21, 2573–2590.
- Dee, D. P.; Uppala, S. M.; Simmons, A. J.; Berrisford, P.; Poli, P.; Kobayashi, S.; Andrae, U.; Balmaseda, M. A.; Balsamo, G.; Bauer, P.; Bechtold, P.; Beljaars, A. C. M.; van de Berg, L.; Bidlot, J.; Bormann, N.; Delsol, C.; Dragani, R.; Fuentes, M.; Geer, A. J.; Haimberger, L.; Healy, S. B.; Hersbach, H.; Hólm, E. V.; Isaksen, L.; Kållberg, P.; Köhler, M.; Matricardi, M.; McNally, A. P.; Monge-Sanz, B. M.; Morcrette, J.-J.; Park, B.-K.; Peubey, C.; de Rosnay, P.;

- Tavolato, C.; Thépaut, J.-N.; Vitart, F., 2011: The ERA-Interim reanalysis: configuration and performance of the data assimilation system. *Journal of the Royal Meteorological Society*, 137 (2011), S. 553–597.
- Deser, C., A. S. Philips, J. W. Hurrell, 2004: Pacific interdecadal climate variability: linkages between the tropics and the North Pacific during boreal winter since 1900. *J. Climate*, 17:3109-24.
- Deser, C., A. S. Philips, R. A. Tomas, Y. Okumura, M. A. Alexander, A. Capotondi, J. D. Scott, Y.-O. Kwon, and M. Ohba, 2012: ENSO and Pacific Decadal Variability in Community Climate System Model Version 4. *J. Climate*, 25, 2622-2651, doi: 10.1175/JCLI-D-11-00301.1.
- Deser, C., M. A. Alexander, S.-P. Xie, A. S. Philips, 2010: Sea Surface Temperature Variability: Patterns and Mechanism. *Annu. Rev. Mar. Sci.* 2010. 2:115-43, doi:10.1146/annurev-marine-124008-151453.
- Dommenget, D., & Latif, M., 2002: A cautionary note on the interpretation of EOFs. *Journal of Climate*, 15(2), 216-225.
- Dommenget, D., T. Bayr, and C. Frauen, 2013: Analysis of the non-linearity in the pattern and time evolution of El Niño Southern Oscillation. *Climate Dyn.*, 40, 2825-2847, doi:10.1007/s00382-012-1475-0
- Eastman, R., Warren, S. G., & Hahn, C. J. (2011). Variations in cloud cover and cloud types over the ocean from surface observations, 1954-2008. *Journal of Climate*, 24(22), 5914-5934.
- Eyring, V., J.-F. Lamarque, P. Hess, F. Arfeuille, K. Bowman, M. P. Chipperfield, B. Duncan, A. Fiore, A. Gettelman, M. A. Giorgetta, C. Granier, M. Hegglin, D. Kinnison, M. Kunze, U. Langematz, B. Luo, R. Martin, K. Matthes, P. A. Newman, T. Peter, A. Robock, T. Ryerson, A. Saiz-Lopez, R. Salawitch, M. Schultz, T. G. Shepherd, D. Shindell, J. Stähelin, S. Tegtmeier, L. Thomason, S. Tilmes, J.-P. Vernier, D. W. Waugh, and P. J. Young, Overview of IGAC/SPARC Chemistry-Climate Model Initiative (CCMI) Community Simulations in Support of Upcoming Ozone and Climate Assessments, SPARC Newsletter No. 40, p. 48-66, 2013.
- Eyring, V., Righi, M., Evaldsson, M., Lauer, A., Wenzel, S., Jones, C., Anav, A., Andrews, O., Cionni, I., Davin, E. L., Deser, C., Ehbrecht, C., Friedlingstein, P., Gleckler, P., Gottschaldt, K.-D., Hagemann, S., Juckes, M., Kindermann, S., Krasting, J., Kunert, D., Levine, R., Loew, A., Mäkelä, J., Martin, G., Mason, E., Phillips, A., Read, S., Rio, C., Roehrig, R., Senfleben, D., Sterl, A., van Ulft, L. H., Walton, J., Wang, S., and Williams, K. D.: ESMValTool (v1.0) – a community diagnostic and performance metrics tool for routine evaluation of Earth System Models in CMIP, *Geosci. Model Dev. Discuss.*, 8, 7541-7661, doi:10.5194/gmdd-8-7541-2015, 2015.

- Gates, W. L., et al., 1999: An overview of the results of the Atmospheric Model Intercomparison Project (AMIP I). *Bulletin of the American Meteorological Society*, 74(3), 387-399.
- Gebbie, G., Eisenman, I., Wittenberg, A. T., and Tziperman, E., 2007: Modulation of westerly wind bursts by sea surface temperature: A semi-stochastic feedback for ENSO. *J. Atmos. Sci.*, 64, 3281-3295.
- Gilman, D. L., Fuglister, F. J., & Mitchell Jr, J. M., 1963: On the power spectrum of “red noise”. *Journal of the Atmospheric Sciences*, 20(2), 182-184.
- Giorgetta, M. A., et al., 2013: Climate and carbon cycle changes from 1850 to 2100 in MPI-ESM simulations for the Coupled Model Intercomparison Project phase 5, *J. Adv. Model. Earth Syst.*, 5, 572-597, doi:10.1002/jame.20038.
- Gleckler, P. J., Taylor, K. E., & Doutriaux, C., 2008: Performance metrics for climate models. *Journal of Geophysical Research: Atmospheres* (1984–2012), 113(D6).
- Guan, B. S. Nigam, 2008: Pacific sea surface temperatures in the twentieth century: An evolution-centric analysis of variability and trend. *J. Climate*, 21, 2790-2809.
- Guilyardi, E., 2006: El Niño - mean state - seasonal cycle interactions in a multimodel ensemble. *Clim. Dyn.*, 26, 229–348.
- Guilyardi, E., A. Wittenberg, A. Fedorov, M. Collins, C. Wang, A. Capotondi, G. J. van Oldenborgh, and T. Stockdale, 2009: Understanding El Nino in ocean-atmosphere general circulation models: Progress and challenges. *Bull. Amer. Meteor. Soc.*, 90, 325-340.
- Hagemann, S., A. Loew, and A. Andersson, 2013: Combined evaluation of MPI-ESM land surface water and energy fluxes, *J. Adv. Model. Earth Syst.*, 5, doi:10.1029/2012MS000173.
- Hagemann, S., K. Arpe, and E. Roeckner, 2006: Evaluation of the hydrological cycle in the ECHAM5 model. *Journal of Climate*, 19(16), 3810-3827.
- Hannay, C., Williamson, D., Hack, J., Kiehl, J., Olson, J., Klein, S., Bretherton, C., and Kohler, M.: Evaluation of forecasted south-east pacific stratocumulus in the NCAR, GFDL, and ECMWF Models, *J. Climate*, 22, 2871–2889, 2009.
- Hou., M., and X. Yan, 2010: A seasonal scale analysis correlating total cloud amount anomalies with ENSO over the tropical Pacific. *Theor. Appl. Climatol.*, 103:471-478, doi:10.1007/s00704-010-0318-3.
- Huffman G. J., R.F. Adler, P. Arkin, A. Chang, R. Ferraro, A. Gruber, J. Janowiak, A. McNab, B. Rudolf, and U. Schneider, 1997: The Global Precipitation Climatology Project (GPCP) Combined Precipitation Dataset. *Bull. Amer. Meteor. Soc.*, 78, 5–20. doi: [http://dx.doi.org/10.1175/1520-0477\(1997\)078<0005:TGPCPG>2.0.CO;2](http://dx.doi.org/10.1175/1520-0477(1997)078<0005:TGPCPG>2.0.CO;2)

- Huffman, G. J., and D.T. Bolvin, 2013: GPCP Version 2.2 SG Combined Precipitation Data Set Documentation.
- Ilyina, T., K. Six, J. Segschneider, E. Maier-Reimer, H. Li, and I. Núñez-Riboni, 2013: Global ocean biogeochemistry model HAMOCC: Model architecture and performance as component of the MPI-Earth System Model in different CMIP5 experimental realizations, *J. Adv. Model. Earth Syst.*, doi:10.1029/2012MS000178.
- Ilyina, T., K. Six, J. Segschneider, E. Maier-Reimer, H. Li, and I. Nunez-Riboni (2013), Global ocean biogeochemistry model ~HAMOCC: Model architecture and performance as component of the MPI-Earth System Model in different CMIP5 experimental realizations, *J. Adv. Model. Earth Syst.*, doi:10.1029/2012MS000178.
- IPCC, 2013: Climate Change 2013 - the Physical Science Basis. Contribution of Working Group I to the Fifth Assessment Report of the Intergovernmental Panel on Climate Change [Stocker, T.F.; D. Qin, G.-K. ; Plattner, M.; Tignor, S.K.; Allen, J.; Boschung, A.; Nauels, Y.; Xia, V.; Bex P.M.] Cambridge, United Kingdom and New York, NY, USA.
- Jin, D., and B. P. Kirtman, 2009: Why the Southern Hemisphere ENSO responses lead ENSO. *J. Geophys. Res.*, 114, D23101, doi:10.1029/2009JD012657.
- Jin, F. F., 1997: An equatorial ocean recharge paradigm for ENSO. Part I: Conceptual model. *J. Atmos. Sci.*, 54, 811-829
- Jöckel, P., A. Kerweg, A. Pozzer, R. Sander, H. Tost, H. Riede, A. Baumgaertner, S. Gromov, B. Kern, 2010: Development cycle 2 of the Modular Earth Submodel System (MESSy2), *Geoscientific Model Development*, 3(2):717-752.
- Jöckel, P., H. Tost, A. Pozzer, C. Brühl, J. Buchholz, L. Ganzeveld, P. Hoor, A. Kerweg, M. Lawrence, R. Sander, B. Steil, G. Stiller, M. Tanarhte, D. Taraborrelli, J. van Aardenne, and J. Lelieveld, 2006: The atmospheric chemistry general circulation model ECHAM5/MESSy1: consistent simulation of ozone from the surface to the mesosphere. *Atmospheric Chemistry and Physics Discussions*, 6:5067-5104.
- Jöckel, P., H. Tost, A. Pozzer, M. Kunze, O. Kirner, C.A.M. Brenninkmeijer, S. Brinkop, D.S. Cai, C. Dyroff, J. Eckstein, F. Frank, H. Garny, K.G. Gottschaldt, P. Graf, V. Grewe, A. Kerweg, B. Kern, S. Matthes, M. Mertens, S. Meul, M. Neumaier, M. Nützel, S. Oberländer-Hayn, R. Ruhnke, T. Runde, R. Sander, D. Scharffe, A. Zahn, 2015: Earth System Chemistry Integrated Modelling (ESCiMo) with the Modular Earth Submodel System (MESSy, version 2.51). *Geoscientific Model Development* (not published yet).
- Joseph, R. and Nigam, S. 2006: ENSO evolution and teleconnections in IPCC's twentieth-century climate simulations: Realistic representation? *Journal of Climate*, 19, 4360-4377

- Jungclauss, J. H., N. Fischer, H. Haak, K. Lohmann, J. Marotzke, D. Matei, U. Mikolajewicz, D. Notz, and J. S. von Storch, 2013: Characteristics of the ocean simulations in MPIOM, the ocean component of the MPI-Earth system model, *J. Adv. Model. Earth Syst.*, 5, 422-446, doi:10.1002/jame.20023.
- Jungclauss, J. H., N. Keenlyside, M. Botzet, H. Haak, J.-J. Luo, M. Latif, J. Marotzke, U. Mikolajewicz, and E. Roeckner, 2006: Ocean circulation and tropical variability in the coupled model ECHAM5/MPI-OM, *J. Clim.*, 19, 3952-3972.
- Kalnay, E., and Coauthors, 1996: The NCEP/NCAR 40-Year Reanalysis Project. *Bull. Amer. Meteor. Soc.*, 77, 437-471.
- Karpechko, A. Y. and E. Manzini, 2012: Stratospheric influence on tropospheric climate change in the Northern Hemisphere, *J. Geophys. Res.*, 117, D05133, doi:10.1029/2011JD017036.
- Karpechko, A. Y., and E. Manzini, 2012: Stratospheric influence on tropospheric climate change in the Northern Hemisphere, *J. Geophys. Res.*, 117, D05133, doi:10.1029/2011JD017036.
- Kunkel, K.E. and Angel, J.R., 1999: Relationship of ENSO to snowfall and related cyclone activity in the contiguous United States. *Journal of Geophysical Research*, 104: doi: 10.1029/1999JD900010. issn: 0148-0227.
- Laing, A.G. and C.H. Paxton, 2002: Assessment of wildfire environments in Florida during 1998. Papers and Proceedings, *Applied Geography Conferences*, 25, 285-293. Binghamton, NY.
- LaJoie, M., and Laing, A., 2008: The influence of the El Niño-Southern Oscillation on cloud-to-ground lightning activity along the Gulf Coast. Part I: Lightning climatology. *Monthly Weather Review*, 136(7), 2523-2542.
- Langenbrunner, B., and J. D. Neelin, 2013: Analyzing ENSO Teleconnections in CMIP Models as a Measure of Model Fidelity in Simulating Precipitation. *J. Climate*, 26, 4431-4446, doi: 10.1175/JCLI-D-12-00542.1.
- Lauer, A., and K. Hamilton, 2013: Simulating Clouds with Global Climate Models: A Comparison of CMIP5 Results with CMIP3 and Satellite Data, *J. Climate*, 26, 3823-3845, doi:10.1175/JCLI-D-00451.1.
- Li, G., S.-P. Xie, 2014: Tropical Biases in CMIP5 Multimodel Ensemble: The Excessive Equatorial Pacific Cold Tongue and Double ITCZ Problems\*. *J. Climate*, 27, 1765-1780, doi: 10.1175/JCLI-D-13-00337.1.
- Lin, J.-L., 2007: The Double-ITCZ Problem in IPCC AR4 Coupled GCMs: Ocean-Atmosphere Feedback Analysis. *J. Climate*, 20, 4497-4525, doi: 10.1175/JCLI4272.1.

- Lin, J.-L., T. Qian, and T. Shinoda, 2014: Stratocumulus Clouds in the Southeastern Pacific Simulated by Eight CMIP5-CFMIP Global Climate Models. *J. Climate*, 27, 3000-3022, doi: 10.1175/JCLI-D-13-00376.1.
- Liu, Z. 2012: Dynamics of interdecadal climate variability: A historical perspective\*. *Journal of Climate*, 25(6), 1963-1995.
- Liu, Z., M. Alexander, 2007: Atmospheric Bridge, oceanic tunnel, and global climate teleconnections, *Rev. Geophys.*, 45, RG2005, doi:10.1029/2005RG000172.
- MacDonald, G. M., & Case, R. A., 2005: Variations in the Pacific Decadal Oscillation over the past millennium. *Geophysical Research Letters*, 32(8).
- Mantua, N. J., and S. R. Hare, 2002: The Pacific Decadal Oscillation. *Journal of Oceanography*, 58, 35-44.
- Mantua, N. J., S. R. Hare, Y. Zhang, J. M. Wallace, and R. C. Francis, 1997: A Pacific interdecadal oscillation with impacts on salmon production. *Bull. Amer. Meteor. Soc.*, 78, 1069-1079.
- Mechoso, C. R., Wood, R., WelleR, R., Bretherton, C. S., Clarke, A. D., Coe, H. ... & Zuidema, P., 2014: Ocean-cloud-atmosphere-land interactions in the Southeastern Pacific: The VOCALS Program. *Bulletin of the American Meteorological Society*, 95(3), 357-375.
- Minobe, S. 1999: Resonance in bidecadal and pentadecadal climate oscillations over the North Pacific: Role in climatic regime shifts. *Geophysical Research Letters*, Vol. 26, pp 855-858.
- Newman, M., 2007: Interannual to decadal predictability of tropical and North Pacific sea surface temperatures. *J. Climate*, 20, 2333–56.
- Newman, M., G. Compo, and M. A. Alexander, 2003: ENSO-forced variability of the Pacific Decadal Oscillation. *J. Climate*, 16, 3853-3857.
- Nijssen, B., G. M. O'Donnell, D. P. Lettenmaier, D. Lohmann, and E. F. Wood, 2001: Predicting the discharge of global rivers. *J. Climate*, 14, 3307–3323.
- O'Dell, C. W., Wentz F. J., Bennartz R., 2008: Cloud liquid water path from satellite-based passive microwave observations: A new climatology over the global oceans. *J. Climate*, 21, 1721-1739.
- Okumura, Y. M., and C. Deser, 2010: Asymmetry in the duration of El Niño and La Niña. *J. Climate*, 23, 5826-5843.
- Park, S. and Leovy C. B., 2004: Marine low-cloud anomalies associated with ENSO. *J. Climate*, 17, 3448-3469.
- Philander, S. G., and Fedorov, A., 2003: Is El Niño sporadic or cyclic? *Annual Review of Earth and Planetary Sciences*, 31, 579-594.

- Philips, A. S., C. Deser, and J. Fasullo, 2014: A New Tool for Evaluating Modes of Variability in Climate Models. *EOS*, 95, 453-455, doi:10.1002/2014EO490002.
- Picaut, J., Masia, F., and du Penhoat, Y., 1997: An advective-reflective conceptual model for the oscillatory nature of the ENSO. *Science*, 277, 663-666
- Pielke Jr, R. A., and Landsea, C. N., 1999: La nina, el nino and atlantic hurricane damages in the united states. *Bulletin of the American Meteorological Society*, 80(10), 2027-2033.
- Rayner, N. A., D.E. Parker, E. B. Horton, C. K. Folland, L. V. Alexander, D. P. Rowell, E. C. Kent, and A. Kaplan, 2003: Global analysis of sea surface temperature, sea ice, and night marine temperature since the late nineteenth century, *J. Geophys. Res.*, 108(D14), doi:10.1029.2002JD002670.
- Reick, C. H., T. Raddatz, V. Borvkin, and V. Gayler, 2013: The presentation of natural and anthropogenic land cover change in MPI-ESM, *J. Adv. Model. Earth Syst.*, 5, 1-24, doi: 10.1002/jame.20022.
- Richman, M. B., 1986: Rotation of principal components. *J. Climatol.*, 6, 293-335.
- Righi M., V. Eyring, K.-D. Gottschaldt, C. Klinger, F. Frank, P. Jöckel, and I. Cionni, 2015: Quantitative evaluation of ozone and selected climate parameters in a set of EMAC simulations. *Geosci. Model Dev.*, 8, 733-768, doi:10.5194/gmd-8-733-2015.
- Roeckner, E.; Brokopf, R.; Esch, M.; Giorgetta, M.; Hagemann, S.; Kornblueh, L.; Manzini, E.; Schlese, U.; Schulzweida, U, 2006: Sensitivity of Simulated Climate to Horizontal and Vertical Resolution in the ECHAM5 Atmosphere Model. *Journal of Climate*, 19 (2006), S.3771–3791
- Ropelewski, C. F., & Halpert, M. S., 1987: Global and regional scale precipitation patterns associated with the El Niño/Southern Oscillation. *Monthly weather review*, 115(8), 1606-1626.
- Rossow, W. B., Schiffer R. A., 1999: Advances in understanding clouds from ISCCP. *Bull. Amer. Meteor. Soc.*, 80, 2261-2287.
- Rossow, W. B., Walker A. W., Beuschel D. E., Roiter M. D., 1996: International Cloud Climatology Project (ISCCP) documentation of new cloud datasets. WMO/TD-737, 115 pp.
- Schaefer, J. T., and F. B. Tatom, 1998: The relationship between El Niño, La Niña, and United States tornadoes, Preprints, 19th Conf. on Severe Local Storms, Minneapolis, MN, *Amer. Meteor. Soc.*, 416-419.
- Schneck, R., C. H. Reick, and T. Raddatz, 2013: The contribution to natural CO<sub>2</sub> variability on time scales of centuries, *J. Adv. Model. Earth Syst.*, 5, 354-365, doi:10.1002/jame.20029.

- Schopf, P. S., and Suarez, M. J., 1988: Vacillations in a coupled ocean-atmosphere model. *J. Atmos. Sci.*, 45, 549-566.
- Simmons, A. J., G. W. Branstator, and J. M. Wallace, 1983: Barotropic 32 wave propagation, instability and atmospheric teleconnection patterns. *J. Atmos. Sci.*, 40, 1363-1392.
- Spencer, H., and J. M. Slingo, 2003: The simulation of peak and delayed ENSO teleconnections. *J. Climate*, 16, 1757-1774.
- Stevens, B., et al., 2013: Atmospheric component of the MPI-M Earth System Model: ECHAM6, *J. Adv. Model. Earth Syst.*, 5, 146-172, doi:10.1002/jame.20015.
- Stoner, A. M. K., K. Hayhoe, D. J. Wuebbels, 2009: Assessing General Circulation Model Simulations of Atmospheric Teleconnection Patterns. *J. Climate*, 22, 4348-4372.
- Taylor, K. E., R. J. Stouffer, and G. A. Meehl, 2012: An Overview of CMIP5 and the Experiment Design. *Bulletin of the American Meteorological Society*, 93(4), 485-498, doi:10.1175/BAMS-D-11-00094.1.
- Trenberth K.E., Branstator G.W., Karoly D., Kumar A., Lau N.-C., Ropelewski C., 1998: Progress during TOGA in understanding and modeling global teleconnections associated with tropical sea surface temperatures. *J. Geophys. Res.* 103:14291–324
- Trenberth, K. E. and D. J. Shea, 2005: Relationships between precipitation and surface temperature. *Geophys. Res. Lett.*, 32, L14703, doi:10.1029/2005GL022760.
- Trenberth, K. E., 1997: The Definition of El Niño. *Bulletin of the American Meteorological Society*, 78, 2771-2777.
- Trenberth, K. E., J. M. Caron, D. P. Stepaniak, S. Worley, 2002: The evolution of ENSO and global atmospheric surface temperatures. *J. Geophys. Res.*, 107, D8, doi:10.1029/2000JD000298.
- Vimont, D. J., 2005: The contribution of the interannual ENSO cycle to the spatial pattern of ENSO-like decadal variability. *J. Climate*, 18, 2080–2092.
- Von Storch, H., and F. W. Zwiers, 1999: *Statistical Analysis in Climate Research*. Cambridge, UK: Cambridge Univ. Press.
- Wang, C., 2001: A unified oscillator model for the El Niño-Southern Oscillation. *J. Climate*, 14, 98-115.
- Wang, C., and J. Picaut, 2004: Understanding the ENSO physics – A review. *Earth's Climate: The Ocean-Atmosphere Interaction*, Geophys. Monogr., Vol. 147, *Amer. Geophys. Union*, 21-48.
- Wang, C., Deser, C., Yu, J. Y., DiNezio, P., & Clement, A. (2012). El Nino and southern oscillation (ENSO): a review. *Coral Reefs of the Eastern Pacific*, 3-19.

- Wang, C., Weisberg, R. H., and Virmani, J. I., 1999: Western Pacific interannual variability associated with the El Niño-Southern Oscillation. *J. Geophys. Res.*, 104, 5131-5149.
- Weisberg, R. H., and Wang, C., 1997: A western Pacific oscillator paradigm for the El Niño-Southern Oscillation. *Geophys. Res. Lett.*, 24, 779-782.
- Wittenberg, A. T., 2009: Are historical records sufficient to constrain ENSO simulations? *Geophys. Res. Lett.*, 36, L12702, doi:10.1029/2009GL038710.
- Wittenberg, A. T., A. Rosati, N.-C. Lau, and J. J. Ploshay, 2006: GFDL's CM2 global coupled climate models. Part III: tropical Pacific climate and ENSO. *J. Climate*, 19, 698-722.
- Wood, R., 2012: Stratocumulus Clouds. *Mon. Wea. Rev.*, 140, 2373–2423. doi:<http://dx.doi.org/10.1175/MWR-D-11-00121.1>
- Wyant, M. C., Wood, R., Bretherton, C. S., Mechoso, C. R., Bacmeister, J., Balmaseda, M. A., ... & Wang, Y., 2010: The PreVOCA experiment: modeling the lower troposphere in the Southeast Pacific. *Atmospheric Chemistry and Physics*, 10(10), 4757-4774.
- Zhang, T., and D.-Z. Sun, 2014: ENSO Asymmetry in CMIP5 Models. *J. Climate*, 27, 4070–4093, doi:10.1175/JCLI-D-13-00454.1.
- Zubiaurre, I. and Calvo Fernández, N., 2012: The El Niño-Southern Oscillation (ENSO) Modoki signal in the stratosphere. *Journal of geophysical research-atmospheres*, 117, ISSN 0148-0227



## **Eigenständigkeitserklärung**

Hiermit erkläre ich, die vorliegende Arbeit selbständig verfasst zu haben und keine anderen als die in der Arbeit angegebenen Quellen und Hilfsmittel benutzt zu haben.

München,

---